

Modeling the Biological Diversity of Pig Carcasses

Erbou, Søren Gylling Hemmingsen; Ersbøll, Bjarne Kjær; Larsen, Rasmus; Christensen, Lars Bager

Publication date:
2009

Document Version
Publisher's PDF, also known as Version of record

[Link back to DTU Orbit](#)

Citation (APA):
Erbou, S. G. H., Ersbøll, B. K., Larsen, R., & Christensen, L. B. (2009). Modeling the Biological Diversity of Pig Carcasses. Kgs. Lyngby, Denmark: Technical University of Denmark (DTU). (IMM-PHD-2008-207).

DTU Library

Technical Information Center of Denmark

General rights

Copyright and moral rights for the publications made accessible in the public portal are retained by the authors and/or other copyright owners and it is a condition of accessing publications that users recognise and abide by the legal requirements associated with these rights.

- Users may download and print one copy of any publication from the public portal for the purpose of private study or research.
- You may not further distribute the material or use it for any profit-making activity or commercial gain
- You may freely distribute the URL identifying the publication in the public portal

If you believe that this document breaches copyright please contact us providing details, and we will remove access to the work immediately and investigate your claim.

Modeling the Biological Diversity of Pig Carcasses

Søren Gylling Hemmingsen Erbou

Kongens Lyngby 2008
IMM-PHD-2008-207

Technical University of Denmark
Department of Informatics and Mathematical Modelling
Building 321, DK-2800 Kongens Lyngby, Denmark
Phone +45 45253351, Fax +45 45882673
reception@imm.dtu.dk
www.imm.dtu.dk

IMM-PHD: ISSN 0909-3192

Preface

This thesis was prepared at the Image Analysis and Computer Graphics group at DTU Informatics and submitted to the Technical University of Denmark (DTU), in partial fulfilment of the requirements for the degree of Doctor of Philosophy, Ph.D., in Applied Mathematics. The project was funded partly by a Ph.D. grant from DTU and partly by the Danish Meat Research Institute (DMRI).

The work herein represents selected parts of the research carried out in the period 2005-2008. The thesis consists of five research papers and an introductory part containing some background information and an overview of the contributions. The work has been carried out in collaboration with the DMRI. Part of the research was conducted at the Australian e-Health Research Centre, CSIRO ICT-centre, Brisbane, Australia. The project was supervised by Professor Bjarne K. Ersbøll and Professor Rasmus Larsen at DTU Informatics, and by Senior Researcher Lars B. Christensen at DMRI.

Kgs. Lyngby, October 2008.

Søren G. H. Erbou

Acknowledgements

This thesis had not seen the light of day without the inspiration, engagement and encouragement from a range of people. First of all I would like to thank my supervisors Bjarne K. Ersbøll, Rasmus Larsen and Lars B. Christensen for their support and for always believing in the project. Thanks to past and present members of the Image Analysis and Computer Graphics group at DTU Informatics for providing an always pleasant and informal atmosphere. A special thanks to my office-mates through most of the time; Martin Vester-Christensen, Mads Fogtmann Hansen and Michael Sass Hansen, who were never too busy to discuss important issues such as the power of procrastination.

Several people at the Danish Meat Research Institute have invested their time in the work that this thesis is based upon. My deepest gratitude goes to Lars B. Christensen and Eli V. Olsen who never ceased to encourage and inspire and always had time for explaining yet another subtlety related to the art of processing pork. They truly have a grand vision for coupling medical imaging to the meat industry. Marchen Hviid, Claus Søndergaard Jensen, Claus Borggaard, Jesper Blom-Hansen and Finn Hansen always showed great interest in collaboration.

My scientific stay with the Australian e-Health Research Centre in Brisbane was in every sense a rewarding and extraordinary experience both scientifically and personally. This was indeed due to the academic interest and great hospitality shown by the mates in Brisbane; Sébastien Ourselin, Jurgen Fripp and the rest of the BioMedIA group. Cheers!

I thank my family and friends for their practical as well as mental support throughout the project. The thesis is dedicated to my dad who only saw the early stages and still kept a strong interest in spite of his sudden illness. Finally my most heartfelt thanks goes to my wife Jane who stood by me from day one and whose love fills me with energy, and to our daughter Karla who makes all the trouble in the world go away with just a smile.

Abstract

This thesis applies methods from medical image analysis for modeling the biological diversity of pig carcasses. The Danish meat industry is very focused on improving product quality and productivity by optimizing the use of the carcasses and increasing productivity in the abattoirs. In order to achieve these goals there is a need for more detailed information about pig carcasses in relation to measures of quality. Non-invasive imaging such as X-ray Computed Tomography (CT) can provide this very detailed information discerning the major tissue types. Medical image analysis provides the tools for extracting and modeling meaningful information from the vast amount of information available from non-invasive imaging data.

The lean meat percentage (LMP) is a common standard for measuring the quality of pig carcasses. Measuring the LMP using CT and using this as a reference for calibration of online equipment is investigated, without the need for a calibration against a less accurate manual dissection. The rest of the contributions regard the construction and use of point distribution models (PDM). PDM's are able to capture the shape variation of a population of shapes, in this case a 3D surface of a specific bone structure in the ham. These models can assist developers of robotic tools by enabling population based testing before actual construction of the tools. Sparse models are compared to the standard PCA based model and a method for fitting PDM's to sparse data is proposed. The former provides more spatially localized modes of variation that are easier interpretable and the latter enables the use of PDM's without the need for full point correspondence of new data.

There is great potential in applying CT as non-invasive modality in the meat industry, e.g. in population based studies, for shape modeling and for analyzing carcass composition. In the future online CT applications can be used to make decisions on the use of each specific carcass by obtaining improved quality measures.

Resumé

Denne afhandling anvender metodikker fra medicinsk billedanalyse til at modellere den biologiske forskellighed af slagtekroppe af svin. Den danske kødindustri er meget fokuseret på at forbedre produktkvalitet og produktivitet ved at optimere brugen af slagtekroppe og øge produktiviteten på slagterierne. For at nå disse mål er der brug for detaljeret information om svineslagtekroppe relateret til kvalitetsmål. Ikke-invasiv billeddannelse, eksempelvis røntgen-baseret Computer Tomografi (CT), kan skelne de væsentlige vævstyper og dermed give denne meget detaljerede information. Medicinsk billedanalyse har de teoretiske værktøjer der kan udtrække og modellere den væsentlige information fra den enorme mængde data som ikke-invasiv billeddannelse frembringer.

Kødprocenten bruges som et fælles mål til at klassificere svineslagtekroppe. Måling af kødprocenten med CT og brugen af denne som reference til kalibrering af online måleudstyr undersøges, og dette uden at skulle kalibrere op mod en ikke så nøjagtig manuel dissektion. De resterende bidrag i afhandlingen drejer sig om opbygning og brug af statistiske formmodeller. Disse kan beskrive formvariation i en population. I denne forbindelse anvendes de på en bestemt knoglestruktur i skinken af slagtekroppen. Formmodeller kan assistere udviklere af robotværktøjer ved at muliggøre populations-baserede undersøgelser uden først at skulle konstruere værktøjerne. Ikke-kompakte formmodeller sammenlignes med standard formmodeller og en metode til at tilpasse formmodeller til data der ikke er komplet bliver beskrevet. Førstnævnte giver modelparametre der er mere lokale spatialt set og derfor lettere at tolke og sidstnævnte gør det muligt at anvende formmodeller til at beskrive nye data uden brug af den fulde punkt-korrespondance.

Der er et stort potentiale ved brug af CT som ikke-invasiv modalitet i kødindustrien, f.eks. i populationsbaserede studier, til formanalyse og til at analysere sammensætningen af slagtekroppe. I fremtiden kan CT applikationer anvendes som beslutningsgrundlag for brugen af den enkelte slagtekrop ved hjælp af forbedrede kvalitetsmål.

Contents

Preface	i
Acknowledgements	iii
Abstract	v
Resumé	vii
Contents	ix
I Summary	1
1 Introduction	3
1.1 Objectives	5
1.2 Thesis Outline	5
1.3 Publications	7
1.4 Nomenclature	9

2	Background	11
2.1	Danish Meat Research Institute	11
2.2	Non-invasive Imaging	17
2.3	Related Work	18
2.4	Data Sets	20
3	Shape Analysis	23
3.1	Shape Descriptors	23
3.2	Surface Reconstruction	25
3.3	Registration	26
3.4	Shape Modeling	28
3.5	Sparse Data	31
4	Contributions	33
4.1	Classification of Pig Carcasses	33
4.2	Building a Point Distribution Model	35
4.3	Sparse Point Distribution Models	37
4.4	Fitting a PDM to Sparse Data	39
4.5	Accelerated Non-Rigid Image Registration	41
5	Discussion and Conclusion	43
5.1	Discussion	43
5.2	Conclusion	45
II	Contributions	47
6	Virtual Dissection of Pig Carcasses	49

6.1	Introduction	49
6.2	Materials and Methods	52
6.3	Results and Discussion	55
6.4	Conclusions	61
7	From CT to Shape Model	63
7.1	Introduction	63
7.2	Methods	65
7.3	Results	70
7.4	Conclusion	77
8	Comparison of Sparse Point Distribution Models	83
8.1	Introduction	83
8.2	Methods	85
8.3	Results and discussion	90
8.4	Conclusion	103
9	Estimation of Shape Model Parameters for 3D Surfaces	105
9.1	Introduction	105
9.2	Methods	106
9.3	Data	110
9.4	Results	110
9.5	Conclusion	113
10	Accelerated 3D Image Registration	117
10.1	Introduction	118
10.2	Methods	119

10.3 Results	128
10.4 Conclusion	132
11 Software	135
11.1 SSM Explorer	135
List of Figures	137
List of Tables	143
Bibliography	145

Part I

Summary

CHAPTER 1

Introduction

For more than half a century production of pork has been an essential part of the Danish economy and today Denmark is the worlds largest exporter of pork. Still the cost of producing meat in Denmark is almost double the cost compared to major competitors such as the U.S. and Brazil [145]. Each year approximately 26 million pigs are produced in Denmark and the vast majority are processed in Danish abattoirs and used for export to more than 130 countries worldwide. In 2007 pork alone accounted for 5%, or 27 billion DKK, of the total Danish export abroad [144]. The meat industry's constant focus on product quality, food safety and efficiency in the production are the main reasons for this success. The vision of the industry is to produce meat products of the highest quality at a competitive price. To achieve this the production must be extremely efficient and well ahead of competitors. Research, development and innovation are the fundamental means to obtain the knowledge required for staying in the lead of the strong competition.

Through the last decade the main focus has been on increasing the productivity in the abattoirs by developing automated robotic tools that can substitute some of the physically very demanding cutting procedures of pig carcasses. It has been a successful strategy resulting in an improved working environment and some quite innovative examples of machinery, but the design of robotic tools is a very complex task. Traditionally a trial-and-error approach is used, testing each small change in tool design on a number of carcasses. The iterative approach in tool design is slow, costly and it is difficult to determine how well suited a tool is

for cutting a whole population of carcasses. This calls for methods for modeling the biological diversity of specific parts of the pig carcass in a population of carcasses, using this information to optimize the process of designing robotic tools and also using it for testing and validation of the tools.

In the years to come the big challenges are to be able to adjust the production quickly and efficiently to the increasingly specific demands of the market and to increase the product range. Necessary conditions for achieving this is optimization of the use of the raw material, i.e. the pig carcasses, and ensuring very uniform quality characteristics in every batch of a specific product. The key to this is to obtain more knowledge of the specific carcass and the population of carcasses and relate this information to the use of the carcass such that the profit is maximized. Recent work [96] suggests that improving measurements of carcasses will result in a substantial improvement in profit due to an optimized use of carcasses and furthermore that the strategic value of improving measurements might be even larger.

Within the medical world there is a long tradition for using non-invasive imaging techniques such as X-ray Computed Tomography (CT), Magnetic Resonance Imaging (MRI), Ultrasound (US) etc. in aiding medical doctors in the diagnosis of patients. Due to the vast amount of data obtainable from these techniques there is a need for tools that can assist in the analysis of the data. This discipline is coined medical image analysis and is a broad field of research based in computer science, mathematics, statistics, medicine and related areas. Statistical shape models (SSM) also known as point distribution models (PDM) is a methodology widely used in medical applications to encapsulate the biological variation in a population of shapes such as *corpus callosum*, heart, liver, bones and cartilage, cf. e.g. [37, 61, 79, 149]. Shape models are often used for classification or regression purposes, e.g. the study of normal vs. abnormal/pathological cases, or relating the model parameters to clinical variables. Their usage could be to gain geometrical knowledge about the variation in the population or to use them for prediction purposes.

It is the intention of this thesis to initiate a bridging of the gap between the two very different worlds of medical image analysis and the meat industry, applying techniques and methodologies of the former in applications from the latter in such a way that new knowledge is obtained in both areas of research. As such the thesis is a product of highly interdisciplinary work.

1.1 Objectives

The main objective of this thesis is to model the biological diversity of pig carcasses by applying non-invasive imaging and image analysis to applications in the meat industry. More specifically the goals are,

- To investigate the use of CT as a common EU reference for pig carcass grading in abattoirs.
- To build a statistical shape model of a specific bone structure of pig carcasses for use when developing robotic tools for abattoirs.
- To determine if sparse models are preferable for the above mentioned application.
- To investigate how statistical shape models can be applied to sparse data

In general the thesis should open the door to image analysis and its versatile use for the meat industry while contributing with scientific publications.

1.2 Thesis Outline

The thesis consists of two parts. Part I is a general introduction and summarizes the work and part II contains scientific publications produced. The publications are self-contained for which reason some overlap occur.

Chapter 2 Introduces and motivates the thesis. A general introduction to the Danish meat industry and where it is heading is provided as well as some examples of recent technological advances.

Chapter 3 Presents a brief overview of methodologies within statistical shape analysis. Based on this choices regarding specific applications are made.

Chapter 4 Summarizes the results of part II supplying an overview of the main contributions of the thesis.

Chapter 5 Consists of a discussion, relating the contributions to applications in the meat industry, as well as an overall conclusion.

Chapter 6 Describes the use of CT as a reference when determining the lean meat percentage (LMP) of pig carcasses using other instruments. A contextual Bayesian classification scheme is applied to classify voxels into three tissue types, fat, meat and bone. A linear model describes the relation between voxels and the full weight of a carcass, which can be determined more accurately than that of the lean meat. This enables the estimation of the LMP more accurately than present methods where operators are involved.

Chapter 7 Proposes a procedure for constructing a 3D point distribution model when faced with highly anisotropic 2D CT scans. It includes segmentation, surface reconstruction using implicit surfaces, registration applying a modified Iterative Closest Point algorithm, a point distribution model based on Principal Components Analysis and model selection using Parallel Analysis.

Chapter 8 Compares 5 different point distribution models suited for data sets containing many variables. The models are based on PCA, Sparse PCA, Varimax, Threshold PCA and Threshold Varimax respectively and are compared w.r.t. sparsity, reconstruction error and interpretability.

Chapter 9 Propose the use of a Gauss-Newton optimization scheme to estimate shape model parameters of 3D surfaces using distance maps, which enables the estimation of model parameters without the requirement of point correspondence. For applications with acquisition limitations such as speed and cost, this formulation enables the fitting of a statistical shape model to arbitrarily sampled data.

Chapter 10 Describes an approach for accelerated image registration. A grid-based warp function is used, parameterized by the displacement of the grid-nodes. The optimization is formulated in the inverse compositional framework resulting in a very efficient optimization algorithm. Storage requirements of the Jacobian and the Hessian are minimized and it is shown that additional constraints on the registration, such as the location of markers, are easily embedded in the optimization.

Chapter 11 Consists of software developed.

1.3 Publications

Scientific publications are listed below. Publications included in this thesis are referred to by chapter number.

Journal papers

- Ch. 6 [167]** M. Vester-Christensen, S. G. H. Erbou, M. F. Hansen, E. V. Olsen, L. B. Christensen, M. Hviid, B. K. Ersbøll and R. Larsen. Virtual Dissection of Pig Carcasses. *Meat Science*, volume 81, pages 699-704, 2009.
- Ch. 8 [54]** S. G. H. Erbou, M. Vester-Christensen, R. Larsen, L. B. Christensen and B. K. Ersbøll. Sparse Point Distribution Models. *Machine Vision and Applications*. doi: 0.1007/s00138-009-0203-1. 2009.
- [168]** C. Vestergaard, S. G. Erbou, T. Thauland, J. Adler-Nissen and P. Berg. Salt Distribution in Dry-cured Ham Measured by Computed Tomography and Image Analysis. *Meat Science*, volume 69, pages 9-15, 2005.

Conference papers

- Ch. 9 [53]** S. G. H. Erbou, S. Darkner, J. Fripp, S. Ourselin and B. K. Ersbøll. Estimation of Shape Model Parameters for 3D Surfaces. *5th IEEE International Symposium on Biomedical Imaging (ISBI)*, pages 624-627, 2008.
- Ch. 10 [166]** M. Vester-Christensen, S. G. Erbou, S. Darkner and R. Larsen. Accelerated 3D Image Registration. *International Symposium on Medical Imaging (SPIE)*, 6512 (651201), 2007.
- [76]** M. F. Hansen, S. Erbou, M. Vester-Christensen, R. Larsen, B. Ersbøll and L. B. Christensen. Surface-to-Surface Registration Using Level Sets. *Scandinavian Conference on Image Analysis (SCIA)*, pages 780-788, 2007.
- [49]** S. G. Erbou, H. B. D. Sørensen and B. Stage. Detection of Cast Shadows in Surveillance Applications. *Den 14. Danske Konference i Mønstergenkendelse og Billedanalyse (DSAGM)*, pages 10-19, 2005.

Conference abstracts

- [51]** S. G. Erbou, M. Vester-Christensen, R. Larsen, E. V. Olsen and B. K. Ersbøll. Quantifying Biological Variation. *European Congress of Chemical Engineering - 6 (ECCE6), Special Symposium - Innovations in Food Technology*, 2007.

- [48] S. G. Erbou. 3D Statistical Shape Model of Bones. *Image Analysis and In-Vivo Pharmacology (IAVP)*, 2007.
- [50] S. G. Erbou, R. Larsen and B. K. Ersbøll. Registration and Shape Modelling of Porcine Bone Structures via CT. *21st Nordic Conference on Mathematical Statistics (NordStat)*, 2006.

Technical Reports

- Ch. 7 [52]** S. G. H. Erbou and B. K. Ersbøll. From CT to Shape Model. *DTU Informatics, Technical University of Denmark*, 20 pages, 2008.

The co-authors of part II and their affiliations are listed below in alphabetical order.

- LARS BAGER CHRISTENSEN
Danish Meat Research Institute, Roskilde, Denmark.
- SUNE DARKNER
DTU Informatics, Technical University of Denmark, Lyngby, Denmark.
- BJARNE KJÆR ERSBØLL
DTU Informatics, Technical University of Denmark, Lyngby, Denmark.
- JURGEN FRIPP
The Australian e-Health Research Centre, CSIRO ICT Centre, Brisbane, Australia.
- MADS FOGTMANN HANSEN
DTU Informatics, Technical University of Denmark, Lyngby, Denmark.
- MARCHEN HVIID
Danish Meat Research Institute, Roskilde, Denmark.
- RASMUS LARSEN
DTU Informatics, Technical University of Denmark, Lyngby, Denmark.
- ELI VIBEKE OLSEN
Danish Meat Research Institute, Roskilde, Denmark.
- SÉBASTIEN OURSELIN
Centre for Medical Image Computing, University College London, United Kingdom.
- MARTIN VESTER-CHRISTENSEN
DTU Informatics, Technical University of Denmark, Lyngby, Denmark.

1.4 Nomenclature

Some of the most commonly used abbreviations and interchangeable terms are listed below.

Abattoir	Slaughterhouse
ASM	Active Shape Model
AAM	Active Appearance Model
CAD	Computer Aided Design
CI	Confidence Interval
CT	X-ray Computed Tomography
DMA	Danish Meat Association
DMRI	Danish Meat Research Institute
GPA	Generalized Procrustes Analysis
HU	Hounsfield Units
ICA	Independent Components Analysis
ICP	Iterative Closest Point
LMP	Lean Meat Percentage
LoCa	Localized Components Analysis
LOO	Leave-one-out
MAT	Medial Axis Transform
MAP	<i>Maximum a Posteriori</i>
MDL	Minimum Description Length
MRF	Markov Random Fields
MRI	Magnetic Resonance Imaging
PA	Parallel Analysis
PC	Principal Component
PCA	Principal Components Analysis
PDM	Point Distribution Model
PGA	Principal Geodesic Analysis
PLSR	Partial Least Squares Regression
Porcine	Related to pigs
PVE	Partial Volume Effects
RBF	Radial Basis Functions
RMS	Root Mean Square
RMSEC	Root Mean Squared Error of Calibration
RMSEP	Root Mean Squared Error of Prediction
SPCA	Sparse Principal Components Analysis
SPHARM	Spherical Harmonics
SSM	Statistical Shape Model
Std.	Standard Deviation
Th. PCA	Threshold Principal Components Analysis
Th. VM	Threshold Varimax
TPS	Thin Plate Spline

US	Ultrasound
VM	Varimax
VS	The Virtual Slaughterhouse

CHAPTER 2

Background

This chapter gives a more detailed description of the meat industry, the challenges it faces and the applications that are used as a basis for the thesis.

2.1 Danish Meat Research Institute

The Danish Meat Association (DMA) is a branch organization for the major meat organizations in Denmark and carries out tasks within areas such as research & development, food safety, veterinary alert systems, marketing, communication, administration and financial management. DMA is owned by the companies running the abattoirs, who are owned by the pig producers, i.e. the farmers. All Research and development activities covering disciplines from when the pigs are picked up at the farmer, through slaughter and processing until consumption are carried out by the Danish Meat Research Institute (DMRI) which is controlled by the DMA. It was founded in 1954 and has a long tradition of collaboration with national and international research organizations. The activities are determined according to the requirements of the industry. The vision is that DMRI must be the leading capacity worldwide concerning product quality, food safety and production efficiency. The goal is to improve the competitive power of the Danish pork and beef industries.

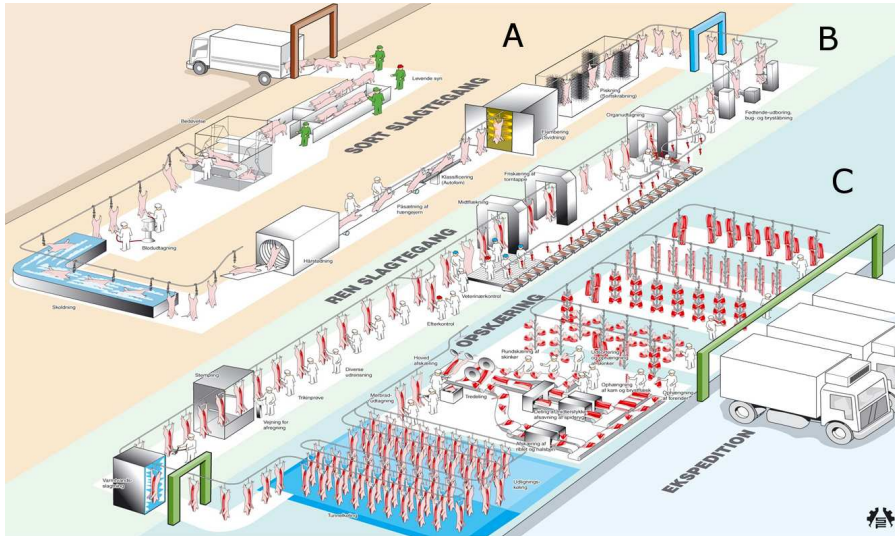


Figure 2.1: Modern abattoir. Part A - sedation, killing and cleaning. Part B - removal of organs, inspection and grading. Part C - Chilling and major cuts. Courtesy of DMA.

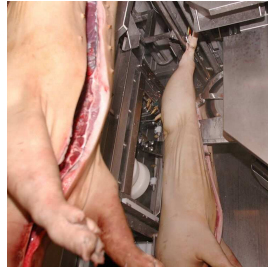
2.1.1 Automating Abattoirs

In recent years modern Danish abattoirs have become more and more automated as a result of the industry's focus on research & development. Figure 2.1 shows a schematic overview of the processes performed in a typical modern abattoir. It consists of three main parts: Part A is where the pigs are sedated, killed and cleaned, part B where internal organs are removed, inspection and grading is performed and the carcasses are split into half. In part C the carcasses are chilled for at least 16 hours and afterwards they are cut into major parts. Especially in part A and B many processes are automated compared to 20 years ago. The remaining processes to automate are quite involved and require substantial knowledge of the biological composition and variability in the pig population. Figure 2.2 shows examples of automated processes in a modern abattoir including removal of organs, carcass splitting, removal of the head, classification using optical probes and removal of bones from the front and middle parts.

The main application of interest in this thesis is modeling a specific part of the pelvic bone structure. Automated cutting of the ham of a carcass is a procedure that has been under development for some years. A part of this procedure involves cutting off the tailbone in a very precise manner. Figure 2.3 shows the



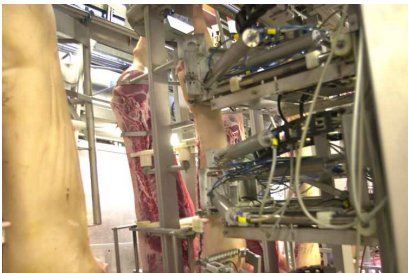
(a) Removal of organs.



(b) Carcass splitting.



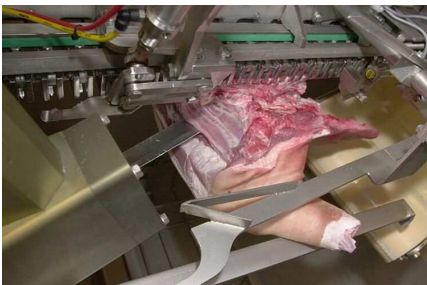
(c) Removal of the head.



(d) Classification using optical probes.



(e) Cutting into 3 parts



(f) Removal of bones in the front part.



(g) Removal of bones in the middle part.

Figure 2.2: Various automated processes in a modern abattoir (Courtesy of DMA).

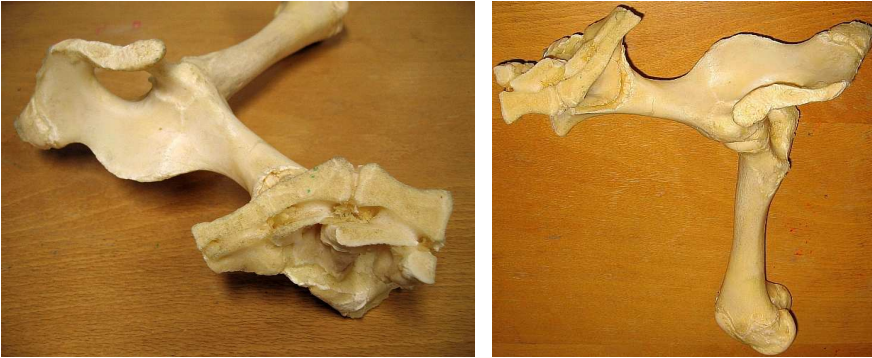


Figure 2.3: Bone structure in the ham of a pig carcass.

bone structure of interest. Many solutions have been tested but no final solution has been agreed upon due to a number of issues. One of the main issues has been to ensure that the cutting tool can handle the biological variation of the pig population in a robust way. Since the requirement for the tool is to do the cut at least as well as a manual butcher, with a high precision, regular methods for tool design have proven insufficient so far. Using statistical shape modeling on CT-scanned data to describe the biological variation of bone structures might be a useful tool for this and other applications, and is the theme of chapters 7 and 8.

2.1.2 Classification of Pig Carcasses

Since the 1930'ies some sort of objective measure for classification of pig carcasses has been used. Today this measure is the lean meat percentage (LMP) which is defined as the proportion of meat in a carcass after removal of all internal organs. It is a simple measure which is quite effective for controlling the amount of meat in Danish pigs. Measuring and standardizing the LMP is given high priority by the DMRI since it is used both to pay the farmer and for sorting the carcasses for optimal use. The LMP is estimated by measuring the loin and fat thickness at certain anatomical positions and by the weight of the carcass. The thicknesses are measured using optical probes, cf. figure 2.2(d), or US, cf. figure 2.4. Every 5 to 10 years these measures are related to the LMP obtained by expert butchers performing a manual dissection of a number of pig carcasses representative of the pig population. This procedure is very costly and has a number of uncertainties incorporated. There is no unique connection between the measures and the LMP, and there is a substantial difference in LMP between butchers when performing the manual dissection, cf. [116]. This is a problem

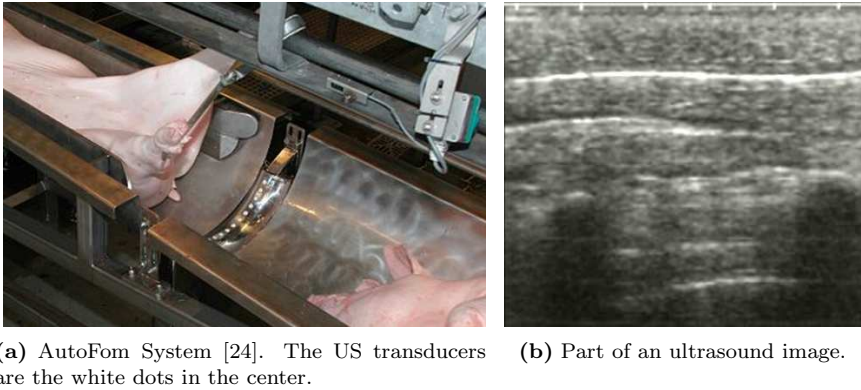


Figure 2.4: Measuring fat thickness using ultrasound. The shadows in (b) are due to two ribs which reflect most of the signal. (Courtesy of DMA).

when the manual dissection is used as a reference for calibration of online equipments throughout the EU. The use of non-invasive imaging, e.g. CT, introduces another way of estimating the LMP, potentially with a much better precision and accuracy than the LMP obtained by manual dissection. This is investigated in chapter 6.

2.1.3 Optimizing the Use of Raw Material

A major challenge for the industry is to optimize the use of pig carcasses. In order to achieve this an improved grading and sorting is necessary such that each carcass is used for the products resulting in the largest yield. The primary measure for sorting carcasses today is the LMP, but there is a general notion in the industry that the LMP is far from a sufficient quality measure when facing the challenges of the future. Even though the present ways of grading pig carcasses in Denmark are state-of-the-art worldwide, the precision is not good enough for sorting the very similar carcasses from the Danish pig population. Moreover the LMP is too simple a measure for describing the meat and fat composition of specific areas of the carcass which is necessary for optimizing its use to specific products.

Contrary to most other types of industry the meat industry faces a reversed type of problem. Instead of assembling many components into a final product, the pig carcass is the only input, and it can end up in a variety of products with some products restricting others. Figure 2.5 shows an example of two very different qualities of the pork loin and the challenge of ensuring a final product of similar quality. Taking the biological variation into account, the current quality



Figure 2.5: Pork loin (Courtesy of DMA).

measures available as well as the logistic limitations in the abattoirs, all makes optimization a very complex task. In [96] Kjærsgaard applies mathematical models for handling some of these challenges and concludes that improving measurements of carcasses results in substantial improvements in profit due to an optimized use of carcasses. The strategic value of improving measurements is estimated to be of similar size or even larger.

2.1.4 The Virtual Slaughterhouse

In 2004 DMRI acquired a medical CT-scanner for research purposes. Through a group of research projects coined "The Virtual Slaughterhouse" (VS) [86] the DMRI is focused on several aspects where non-invasive imaging using CT can be applied. The choice of CT as modality is based on a number of benefits compared to other modalities, cf. section 2.2. First of all CT allows imaging of the full volume of a carcass, it is much cheaper than MRI, the ionizing radiation is less of an issue since it is not live tissue that is scanned, and CT is being used by some industries already. A part of VS is carried out by a number of M.Sc. and Ph.D.-projects concerning different aspects of mathematical modeling, image analysis, shape modeling etc. applied to pig carcasses and related to some of the issues mentioned in section 2.1, cf. [48, 50–54, 74–76, 96, 105, 164–167]. In [165] Vester-Christensen and Larsen investigate the use of image registration as a tool for measuring the quality of virtual cuts. Image registration provides the means to propagate a set of cuts defined in an atlas onto a population of carcasses and estimate the yield of the different cuts.

The goal for VS is to develop new and innovative tools for analyzing 3D models of pig carcasses to be used for optimizing both the production and product

development. Furthermore it is the goal to identify predictors of quality that can be used for online measurements in the future.

2.2 Non-invasive Imaging

The term non-invasive imaging is used for imaging modalities that do not mechanically penetrate the object of interest.

2.2.1 Ultrasound

In Ultrasound (US), cf. e.g. [28, 88], transducers emit high frequency sound pulses (2 – 18MHz) into the tissue. For every tissue transition a part of the signal is reflected and received by the transducers which measure the duration of the pulses. The difference in densities of tissue types determines the signal proportion reflected in a transition. US is used for soft tissue transitions since a significant part of the signal penetrates these transitions. Gases and solids reflect most of the signal such that deeper penetration is impossible. Using several transducers an image can be reconstructed based on the reflections. Low frequencies enable larger penetration depth but lower spatial resolution and vice versa. The advantages of US are that it is inexpensive, handy, a non-ionizing modality (a nice feature for live tissue), suitable for real-time and soft tissue imaging. On the other hand the major limitations of US are that the signal cannot penetrate any gas (e.g. air) between the transducers and the tissue, it cannot penetrate bone, it only detects transitions between tissues and not type of tissues.

2.2.2 Magnetic Resonance Imaging

Magnetic Resonance Imaging (MRI) [28] exploits the fact that some nuclei, e.g. the proton in hydrogen (1H), have a non-zero net spin and therefore a magnetic moment. Spins are normally randomly oriented but when imposing an external static magnetic field \mathbf{H}_0 a fraction of the spins align either parallel or antiparallel with \mathbf{H}_0 resulting in net magnetization. The protons are not exactly aligned with \mathbf{H}_0 but precess around the direction of the field like gyroscopes with a frequency proportional to the strength of the magnetic field. Depending on the temperature some protons adopt the high energy antiparallel state instead of the low energy parallel state. Imposing a radio frequency (RF) pulse with a frequency related to \mathbf{H}_0 , and orthogonal to \mathbf{H}_0 , more proton spins are excited to the high energy antiparallel state. When the RF pulse ends the excited

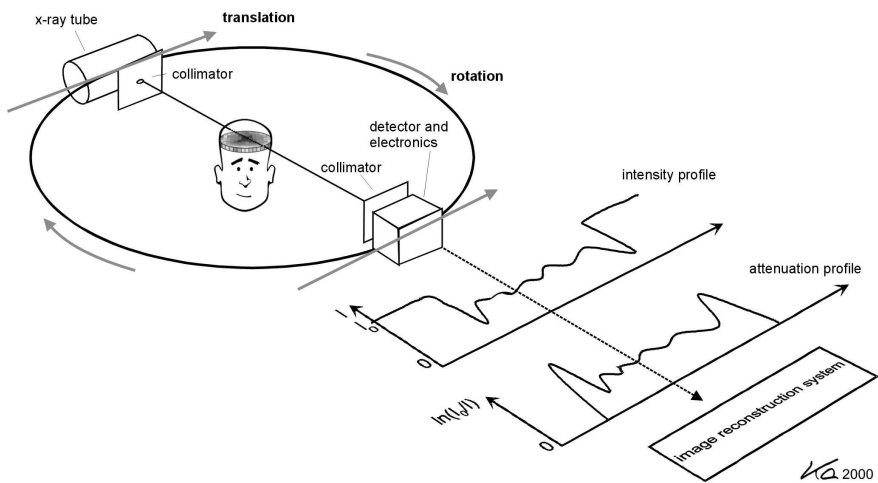
protons return to their equilibrium state by emitting a RF signal with the same frequency, which can be measured. Two relaxation mechanisms occur, the spin-lattice relaxation is longitudinal w.r.t. \mathbf{H}_0 and denoted T_1 and the spin-spin relaxation, which is transversal compared to \mathbf{H}_0 , is denoted T_2 . Superimposing gradient magnetic fields on \mathbf{H}_0 enables extraction of spatial information from the signals and excitation by RF pulses provide contrast information enabling the construction of images. The relaxation constants are quite sensitive to differences in tissue types revealing very good contrast in soft tissue. MRI scanners are expensive and images do not have a fixed scale contrary to CT. On the other hand it does not apply ionizing radiation and a very flexible contrast can be obtained.

2.2.3 X-ray Computed Tomography

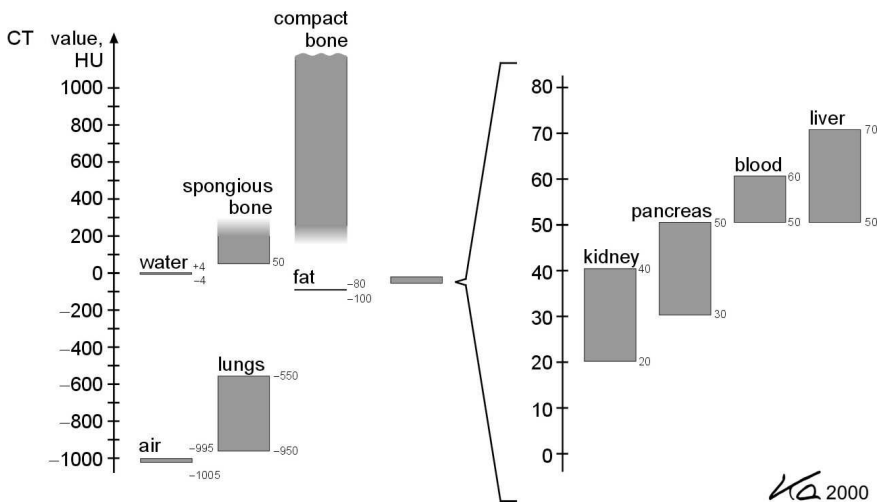
In X-ray Computed Tomography (CT) [28, 94] the attenuation of X-rays through a material is detected. Different tissue types have different densities and attenuation. Rotating the X-ray tube and detectors around the object of interest, line integrals of the linear attenuation coefficients are obtained, cf. figure 2.6(a). Image reconstruction can be done by applying e.g. filtered backprojection which is basically an inverse Radon transform of the line integrals with some filters applied, cf. [28]. The linear attenuation coefficients of the image are scaled to Hounsfield Units (HU), cf. figure 2.6(b), in such a way that water will have the value 0HU and air the value -1000HU , thereby enabling quantitative comparisons across objects, scanners and experiments by a standardized calibration scheme. This and the fact that CT scanners are much less expensive than MRI scanners are the major advantages compared to MRI. CT is better for imaging bone and distinguishing bone and soft tissue, but is inferior to MRI for distinguishing different soft tissue organs. For imaging live tissue CT has the drawback that it uses ionizing radiation, i.e. it introduces a health hazard. Early type scanners acquired one slice at a time and then moved the object to the next position etc. Modern type scanners are both multi-slice acquiring multiple slices for each revolution, and spiral, moving the table while scanning resulting in a spiral type of data acquisition, which speeds up the data acquisition substantially.

2.3 Related Work

Non-invasive imaging has been applied by numerous authors for estimation of body composition of animals such as pigs and lamb. The first applications of CT in meat science was performed by Skjervold *et al.* [143] and Allen & Vangen



(a) Principle of CT.



(b) Hounsfield scale (HU).

Figure 2.6: X-ray Computed Tomography (Courtesy of W. A. Kalender [94]).

[3] in the early 1980'ies. Reviews of major work up until the late 1990'ies are found in [14, 147, 155]. Junkuszew *et al.* [92] compare a single CT-slice and a single US-measurement to manual dissection for estimating lamb carcass composition. Johansen/Kongsro *et al.* [89, 97] apply thresholds to the histogram of 15 anatomically chosen slices of CT-scanned carcasses of lamb to segment fat and meat tissue for prediction of the corresponding weights in a manual dissection. This is compared to other methods for grading lamb carcasses in [98]. Navajas *et al.* [113] use CT to measure specific muscle volumes in lamb. [64] derive and compare estimators of tissue volumes in CT images taking mixed pixels, or Partial Volume Effects (PVE), of fat and meat into account. Vestergaard *et al.* [168] quantify the distribution and penetration of salt in dry-cured ham using CT. Dobrowolski *et al.* [46] and Romvári *et al.* [133] use thresholds in the histogram of CT scans, and Collewet [31] of MRI scans, to segment meat voxels of pig carcasses. Partial least-squares regression (PLSR) of histogram values is applied to model the dissected lean meat content. Common for the above mentioned methods is that they only take into account the histogram value of the voxel to be classified and not any of the neighboring voxels. Monziols *et al.* [110, 111] estimate the fat and meat content in pig carcasses from MRI using (2D) contextual information and modeling fat, meat and mixed pixels of fat and meat. Some of the mentioned work is part of the EUPIGCLASS project [55] which investigates the use of MRI and CT for pig carcass classification.

2.4 Data Sets

The data is acquired with different types of single-slice and multi-slice CT scanners. In general it is chilled parts of pig carcasses that are scanned, where all internal organs are removed.

2.4.1 Ringsted 2008

The Ringsted 2008 data set consists of full body CT scans of 299 half pig carcasses of mixed breeds. They represent the Danish pig population w.r.t. weight and fatness. Voxel dimensions are $[0.9 \times 0.9 \times 10]$ mm with 10mm spacing between each slice. This data set is used in chapter 6.

2.4.2 Duroc

The Duroc data set consists of full body CT scans of 40 half pig carcasses of the Duroc breed, both male and female. Voxel dimensions are $[0.88 \times 0.88 \times 10]$ mm

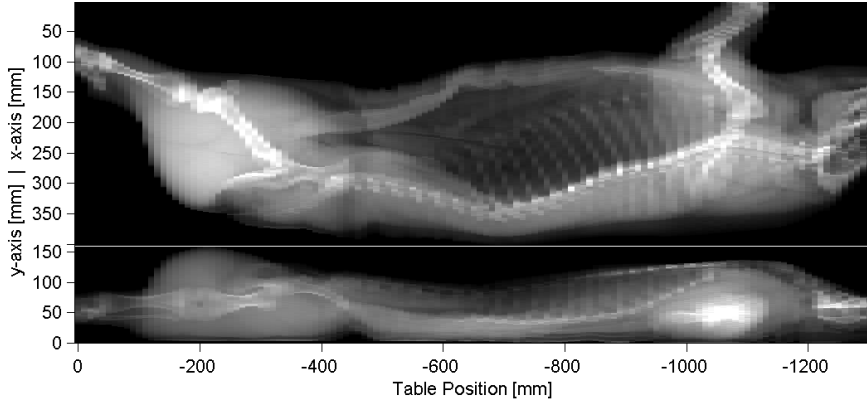


Figure 2.7: CT topogram.

with 10mm spacing between each slice. Figure 2.7 shows a CT topogram, from two views, of a carcass from the *Duroc* data set. In this thesis 33 of the 40 observations in the data set are used for modeling the shape of a specific part of the pelvic bone. The remaining 7 were excluded from the application due to incomplete structures of interest. Chapters 7, 8 and 9 use this data set. Figure 2.3 shows an image of the bones in the ham of a pig carcass. The part of the pelvic bone that is modeled is comprised by the *illium*, *pubis* and *ischium*, cf. [90]. It has genus 1 topology, i.e. it is topologically similar to a torus, but with 2 separate boundaries where the *sacral vertabrae* (tail bone) and the *femur* bone are connected to the pelvic bone. The method chosen for modeling the bone structure should be able to handle such topological complexity.

Shape Analysis

Multivariate analysis of biological shape variation, or morphometrics, have been studied intensively throughout the last decades [18] and several representations for describing anatomical shape have been developed. A brief overview of key methods within statistical shape analysis related to part II is provided in this chapter. Based on the objectives of the thesis and the data used, specific choices are made.

3.1 Shape Descriptors

A widely used method for modeling shape is by their boundary points and their distribution [19]. Cootes *et al.* proposed the point distribution model (PDM) [36] as a statistical shape model (SSM) which encapsulates the variation in a population of shapes. This was extended into the Active Shape Model (ASM) where the PDM is used as a prior for segmentation [34, 35, 37]. The Active Appearance Model (AAM) [38] extended the ASM to include intensity information making it more robust for segmentation purposes and it has been used in numerous medical applications, cf. e.g. [148, 149].

Staib and Duncan [146] model both open and closed genus 0 as well as genus 1 surfaces using fourier basis functions. Shapes are parameterized by fourier coef-

ficients. Genus 1 surfaces with boundaries are not treated with this method. Another parametric surface representation is by spherical harmonics (SPHARM) [20, 62]. It can be used for modeling spherical objects, i.e. of genus 0 topology. The surfaces are parameterized at any level of detail using a number of SPHARM as basis functions. Recent work [84, 140, 153] make use of the implied sampled surface SPHARM-PDM to address some of the limitations of the original SPHARM registration algorithm. Still an inherent property of SPHARM is the limitation to shapes topologically similar to a sphere. Both of these methods are global, hierarchical, and multi-scale representations.

Another type of representation is based on the medial manifold. Blum proposed the Medial Axis Transform (MAT) [16], also denoted the skeleton, as a natural geometry for biological shape. The representation is sensitive to boundary noise but later work considered this issue, cf. e.g. [95]. Golland *et al.* [65] apply a skeleton of fixed topology to remedy the problem of boundary noise. The medial representation M-Reps, suggested by Pizer *et al.* [91, 123–125], is a compact surface parametrization based on a sequence of medial primitives of a shape, denoted medial atoms. Each atom comprises a hub (center), two equal-length spokes which are orthogonal to, and touch, the surface, as well as their unit direction vectors. This representation allows a natural separation of properties such as bending, growth, scale and location, and it is designed to deal with both objects and surrounding ensembles of objects. The drawback is a rather involved shape representation with parameters that are not elements of Euclidean space.

Signed distance maps for shape modeling was introduced by Leventon *et al.* [102] and has been used for both modeling and segmentation [66–68, 160]. Distance maps embed the shape as the zero level set of a higher dimensional distance function, cf. [120, 139]. The closest distance to the shape is assigned to each element of the distance map. If inside an object negative distances are assigned and if outside the object positive distances are assigned. Topological changes can be modeled and there is no need for point correspondence. The drawbacks are that signed distance maps are not uniquely defined for open surfaces, i.e. inside and outside needs to be defined. Furthermore applying Principal Components Analysis (PCA) for building a linear shape model only produces approximated distance maps since convex linear combinations of distance maps do not produce distance maps. Representing shapes with distance maps also add a lot of redundancy to the representation, i.e. a much more dense representation is obtained.

In deformation based morphometry shapes are embedded in volumetric data and then deformation fields obtained from voxel-based registration are used for analyzing complex structures such as the brain, cf. e.g. [9, 152]. The Jacobian of the deformation fields indicates a contraction or expansion enabling voxel-wise hypothesis testing of volume changes.

The specific bone structure modeled in this thesis requires a shape descriptor capable of representing shapes of genus 1 topology with two boundaries. The simple representation using boundary points is capable of that and is applied in chapters 7, 8 and 9. Surfaces are represented by a set of triangles which are defined by vertices/points on the surface. The triangles relate points to each other enabling the calculation of differential properties of the surface.

3.2 Surface Reconstruction

The surfaces need to be extracted from the CT data before a PDM can be built. The Marching Cubes algorithm suggested by Lorensen and Cline [103] extracts iso-surfaces from a regularly sampled volume (e.g. CT or MRI). It is based on a lookup table consisting of the possible triangle configurations of the surface through a voxel. For very anisotropic voxels this might introduce unwanted artifacts and it is sensitive to noise and outliers.

The Power Crust algorithm proposed by Amenta *et al.* [4] is based on an approximation of MAT based on a set of surface points. From this a subset of the vertices of the Voronoi diagram is used to construct the surface of the object.

Since CT data is used in the present application the Marching Cubes algorithm could be applied directly, but this results in too many artifacts due to noise and the highly anisotropic sampled data, cf. section 2.4. Instead another approach is taken, segmenting the surface contours using a simple threshold and some morphology to reduce noise. Using points on these contours as constraints an implicit surface is estimated using Radial Basis Functions (RBF) as done by e.g. Turk and O'Brien [26, 161, 162]. An implicit surface is a mapping $f : \mathbb{R}^3 \rightarrow \mathbb{R}$ from coordinates to a scalar value. The surface is defined as the points in the volume where the scalar value is zero. The aim is to estimate a function, $f(\mathbf{x})$ that minimizes some energy measure, usually the aggregate curvature, subject to some interpolation constraints. This is the Thin Plate Spline (TPS) solution. Using a linear combination of RBF's of the form $\phi(\mathbf{x}) = |\mathbf{x}|^3$ ensures that the energy function is minimized. Other basis functions can also be used, e.g. $\phi(\mathbf{x}) = |\mathbf{x}|$ [26]. These specific basis functions ensure the extension of TPS interpolation into 3D. In the TPS solution areas of large curvature, e.g. sharp edges, need many constraints to be modeled properly. A radial basis function is centered on each data point and the interpolation function can then be written as:

$$f(\mathbf{x}) = \sum_{j=1}^k w_j \phi(\mathbf{x} - \mathbf{c}_j) + P(\mathbf{x}) \quad (3.1)$$

w_j are the weights, $\mathbf{c}_j = (c_j^x, c_j^y, c_j^z)$ are the locations of the constraints and $P(\mathbf{x})$

is a first order polynomial that accounts for linear and constant portions of f which ensures a unique solution. The number of weights to estimate depends on the number of constraints. To ensure that the surface interpolates the constraints of values $h_i = f(\mathbf{c}_i)$, the constraints are substituted into equation 3.1:

$$h_i = \sum_{j=1}^k w_j \phi(\mathbf{c}_i - \mathbf{c}_j) + P(\mathbf{c}_i) \quad (3.2)$$

This can be written as a system of linear equations, where $\phi_{ij} = \phi(\mathbf{c}_i - \mathbf{c}_j)$:

$$\begin{bmatrix} \phi_{11} & \phi_{12} & \dots & \phi_{1k} & 1 & c_1^x & c_1^y & c_1^z \\ \phi_{21} & \phi_{22} & \dots & \phi_{2k} & 1 & c_2^x & c_2^y & c_2^z \\ \vdots & \vdots & \ddots & \vdots & \vdots & \vdots & \vdots & \vdots \\ \phi_{k1} & \phi_{k2} & \dots & \phi_{kk} & 1 & c_k^x & c_k^y & c_k^z \\ 1 & 1 & \dots & 1 & 0 & 0 & 0 & 0 \\ c_1^x & c_2^x & \dots & c_k^x & 0 & 0 & 0 & 0 \\ c_1^y & c_2^y & \dots & c_k^y & 0 & 0 & 0 & 0 \\ c_1^z & c_2^z & \dots & c_k^z & 0 & 0 & 0 & 0 \end{bmatrix} \begin{bmatrix} w_1 \\ w_2 \\ \vdots \\ w_k \\ p_0 \\ p_1 \\ p_2 \\ p_3 \end{bmatrix} = \begin{bmatrix} h_1 \\ h_2 \\ \vdots \\ h_k \\ 0 \\ 0 \\ 0 \\ 0 \end{bmatrix} \quad (3.3)$$

Solving this system with respect to the weights can be done using standard methods and is straightforward up to a couple of thousands of constraints. In addition to the zero-valued constraints defined on the surface, additional constraints are needed to define the sign of the interior and exterior parts of the surface. A typical method is to place constraints at a small distance away from the surface contours along their normal and assign to them the positive or negative distance value.

When the weights are estimated, equation 3.1 can be used to resample the implicit function at an arbitrary resolution, e.g. isotropic. The TPS solution ensures minimum bending energy [17] of the surface, i.e. the smoothest surface given the point constraints. The Marching Cubes algorithm is then applied to extract the surface of the bone. This is described in chapter 7. The drawback of applying TPS RBF's is that they have global support, i.e. each constraint/basis function contributes to all of the implicit surface. This calls for iterative ways of solving the system of linear equations if more than a couple of thousands of constraints are used. Otherwise compactly supported RBF's can be applied [112], but these are only approximately TPS solutions, and cannot be evaluated outside their support.

3.3 Registration

In order to do statistical analysis the observations of interest need to be comparable, i.e. correspondence is necessary. Image Registration is the task of trans-

forming two or more images (2D/3D) such that their corresponding regions are aligned. The transformation can be e.g. rigid, affine or non-rigid and constrained in different ways. Landmark-based methods require defining corresponding features as parameters, e.g. points, surfaces or curves, while intensity-based methods use the image intensity directly. Overviews of registration algorithms are given in [10, 63, 108, 109, 172].

In intensity-based registration it is the deformation field that is analyzed. A variety of voxel-based non-rigid registration algorithms are available. Some include non-parametric physics-based transformation models, e.g. elastic [11, 23], fluid [21, 22, 29] and diffusion [109, 157] registration. The similarity measure used can be based on e.g. intensity directly, correlation or Normalized Mutual Information [151]. Parametric methods include, e.g. the widely used method by Rueckert *et al.* [134–136], which applies B-Splines on a grid to define the deformation field. B-splines are simple and have local support but when used in a hierarchical manner a global-to-local deformation can be obtained [101, 170]. In order to avoid folding of the deformation field, i.e. changing the topology, regularization is applied e.g. by volume preservation or smoothness. Ensuring that the deformations are diffeomorphic, i.e. differentiable and invertible, ensure that no folding occurs. Cootes *et al.* [39, 41] apply compositions of simple diffeomorphic transformations of nodes in a grid for obtaining a more complex but diffeomorphic deformation fields. Using an appropriate kernel function in the interpolation scheme ensures the diffeomorphic nature of the deformation field. In chapter 10 this method is reformulated to improve speed and for incorporating landmark constraints. Nielsen *et al.* [114, 115] formulate the diffeomorphic property in a Bayesian setting as a prior on the warp (transformation) function based on Brownian motion.

The most commonly used method for landmark-based registration is the Iterative Closest Point (ICP) algorithm by Besl and McKay [15]. For each point in a set of points the closest point in the other set of points is determined. Then the optimal rigid transformation between the point sets is determined and applied. This is done until convergence. Several extensions have been applied to the original ICP formulation, cf. [137], e.g. restricting the direction where the closest point search is done. Chapters 7,8 and 9 apply an extended version of ICP using the estimated mean curvature normal to restrict the search. Other work includes Zhang *et al.* [171] who apply a neural network in a 3D surface-based rigid registration system for image-guided surgery on bone structures for automatic real-time registration for intra-operative scans. Andresen *et al.* propose geometry constrained diffusion for non-rigid registration of mandibular surfaces in growth modeling [5–8]. Lüthi *et al.* [106, 107] represent surfaces as signed distance maps and apply Thirion’s Demons algorithm [157] with a curvature based regularization term for surface registration. Darkner *et al.* [42] apply grid-based diffeomorphic warps of distance maps for non-rigid surface registration. Xie

et al. [170] use hierarchical B-Splines in a non-rigid version of ICP for smooth surface registration.

Landmarks can be defined by anatomical or mathematical features (e.g. curvature) and be distributed between these [17]. For simple 2D shapes landmarks can often be obtained manually or semi-automatic. In 3D this is a problem and automated methods are necessary. Davies *et al.* [43, 44] proposed applying the Minimum Description Length (MDL) principle for optimizing correspondences across a set of shapes. It originates from information theory and it is argued that the best model is the one which describes the training set as efficiently as possible. The cost function describes the cost of transmitting the PCA representation of the shapes. Later it has been extended to include curvature in 2D [159], applied in the AAM framework [158] and other optimization procedures have been applied, cf. e.g. [78]. In 3D the MDL method has been applied to spherical shapes (genus 0) by mapping the landmarks to a sphere, cf. e.g. [61, 79]. Styner *et al.* [154] compare MDL-based models with the SPHARM representation and shows that MDL is clearly superior w.r.t. compactness. Horkaew *et al.* extend the MDL to model spherical shapes with boundaries [81], even for complex topologies such as the heart [82]. Paulsen *et al.* [121] apply a smoothing of the correspondence vector field between two surfaces using a Markov Random Field (MRF) formulation .

Due to the complex topology of the bone structure that is modeled in this thesis, no optimization of correspondence is applied, but is left for future work.

3.4 Shape Modeling

When landmark correspondence is obtained the shapes need to be aligned w.r.t. translation, rotation and maybe scale. This is done in an iterative manner by the Generalized Procrustes Analysis (GPA) [47, 71, 72]. The PDM, proposed by Cootes *et al.* [36, 37], is a compact way of describing shape variation in a data set. Let the n shapes be represented by k corresponding 3D points, each arranged in a p -dimensional vector \mathbf{s} ($p = 3k$). The idea is to formulate a parameterized model of the form $\mathbf{s} = M(\mathbf{g})$ describing the variation seen in the data, where \mathbf{g} is a vector of shape parameters of the model M . The sample mean $\bar{\mathbf{s}}$ and sample covariance matrix \mathbf{C} are defined as

$$\bar{\mathbf{s}} = \frac{1}{n} \sum_{i=1}^n \mathbf{s}_i, \quad (3.4)$$

$$\mathbf{C} = \frac{1}{n-1} \sum_{i=1}^n (\mathbf{s}_i - \bar{\mathbf{s}})(\mathbf{s}_i - \bar{\mathbf{s}})^T. \quad (3.5)$$

Since shapes are often represented by very dense point sets, n is much larger than p and a PCA is appropriate for decomposition, cf. [87]. The PCA determines the main axes (eigenvectors ϕ_i) of variation of the data and sorts them according to the amount of variation they describe (eigenvalues λ_i). The model can then be formulated as a perturbation of the mean shape:

$$\mathbf{s} = \bar{\mathbf{s}} + \mathbf{\Phi} \mathbf{g} \quad (3.6)$$

where $\mathbf{\Phi}$ is the matrix composed of the eigenvectors ϕ_i . The model parameters of a new aligned shape \mathbf{s}' can be obtained by projecting it into the parameter space,

$$\mathbf{g}' = \mathbf{\Phi}^T (\mathbf{s}' - \bar{\mathbf{s}}). \quad (3.7)$$

The eigenvectors (or loading vectors) provide the linear combinations (loadings) of points revealing the maximum variation (eigenvalues) of the original data expressed by the minimum number of parameters in the model. The only decomposition where the loading vectors are orthogonal and the principal components (PC), or scores, i.e. the data projected onto the loading vectors, are uncorrelated is the PCA. It is also used for modeling deformation fields obtained from intensity based registration methods, cf. e.g. [117, 118]. An important point to make when interpreting PDM's is that they are purely data-driven. They only show the variability expressed in the data from which they are built. Using such models for prediction should therefore be done with care, considering how well the data represent the population one is trying to predict features from.

In [25] Cadima and Jolliffe discuss the method of truncation of small loadings of the eigenvectors of the PCA, also known as threshold PCA (Th. PCA). It is emphasized that particular care should be taken in cases where the resulting loading vectors are far from orthogonal. Kaiser [93] proposed the varimax criteria (VM) for orthogonal factor rotation. It estimates a rotation matrix \mathbf{R} which is applied to the matrix of the first t eigenvectors $\mathbf{\Phi}_t$. If each element in the $p \times t$ matrix $\mathbf{\Phi}_t$ is denoted ϕ_{ij} , the varimax criterion can be formulated as

$$V(\mathbf{\Phi}_t) = \sum_{j=1}^t \left(\frac{1}{p} \sum_{i=1}^p \phi_{ij}^4 - \left(\frac{1}{p} \sum_{i=1}^p \phi_{ij}^2 \right)^2 \right). \quad (3.8)$$

It seeks to estimate the rotation matrix which maximizes the sum of the column-wise variances of the squared elements. The outcome of such a rotation results in correlated scores, but is likely to reveal modes with more loadings close to 0 or ± 1 which tend to be more localized and therefore easier to interpret. Stegmann *et al.* [150] apply the whole family of orthogonal rotation methods called Orthomax, of which the varimax method is a special case. They apply it on three 2D cases of shape and appearance models. The results show more localized modes than corresponding PCA modes and are recommended for data sets with a large number of variables, e.g. 3D surfaces.

Zou *et al.* [173] propose the sparse PCA (SPCA), which limits the sum of absolute loadings by constraining each loading vector and thereby estimates more sparse loadings more or less close to the original PCA loadings. It is formulated as a regression problem approximating the properties of a PCA, but with sparse modes. The following SPCA criterion is minimized

$$\begin{aligned} (\hat{\mathbf{A}}, \hat{\mathbf{B}}) &= \arg \min_{\mathbf{A}, \mathbf{B}} \sum_{i=1}^n \|\mathbf{x}_i - \mathbf{A}\mathbf{B}^T \mathbf{x}_i\|^2 \\ &+ \lambda \sum_{j=1}^t \|\mathbf{b}_j\|^2 + \sum_{j=1}^t \delta_j \|\mathbf{b}_j\|_1, \\ \text{s.t. } &\mathbf{A}^T \mathbf{A} = \mathbf{I}. \end{aligned} \quad (3.9)$$

\mathbf{x}_i is the i th column of the $p \times n$ matrix \mathbf{X} containing the parameters of the n surfaces. \mathbf{B} contains the t loading vectors (\mathbf{b}_j) and \mathbf{A} projects the scores back into the original space of \mathbf{X} . The first term thereby measures the reconstruction error, while the constraint on \mathbf{A} ensures a solution where \mathbf{B} is close to orthogonal. The remaining terms ensure a unique solution for cases where $p > n$, while driving \mathbf{B} towards a sparse solution. [173] propose an iterative algorithm for solving equation 3.9 w.r.t. \mathbf{B} . It is also shown that if $p \gg n$, then letting $\lambda \rightarrow \infty$, so-called soft thresholding can be used to estimate \mathbf{B}

$$\mathbf{b}_j = (|\mathbf{a}_j^T \mathbf{X} \mathbf{X}^T| - \frac{\delta_j}{2})_+ \text{Sign}(\mathbf{a}_j^T \mathbf{X} \mathbf{X}^T). \quad (3.10)$$

\mathbf{a}_j is the j th column of \mathbf{A} and $(\cdot)_+$ denotes $\max(0, \cdot)$. δ_j sets the weight given to the sparsity term and can be set individually for each mode if desired. Eq. 3.9 is solved iteratively by fixing \mathbf{A} , solving for \mathbf{B} and then recalculating \mathbf{A} . The number of loading vectors t should be set beforehand, and is often set according to the PCA solution. Often a specific sparsity level, in terms of the number of non-zero loadings is used as stopping criteria for the algorithm, and this is achieved by dynamically changing δ_j for each iteration. SPCA is applied by Sjöstrand *et al.* [141] and Ólafsdóttir *et al.* [117] for shape analysis in medical applications. Alcantara *et al.* [2] propose Localized Components Analysis (LoCa), which is a variant of SPCA where a measure of spatial locality is included in the cost function.

In a PDM each shape is seen as an observation in p -dimensional space and the underlying assumption for applying a PCA is that the observations constitute a Gaussian distribution which is often, but not always, the case, e.g. for rotations. Another example is the M-Reps mentioned in section 3.1, which are not elements of Euclidean space but instead are elements of a Lie group. This means that standard PCA based statistics cannot be applied. Fletcher *et al.* [56–58] have generalized the PCA to the nonlinear manifold setting denoting it Principal Geodesic Analysis (PGA), enabling a compact description of variability using medial representations. Kernel PCA has also been applied for nonlinear shape modeling, cf. e.g. Rathi *et al.* [131]. The shapes are mapped from input space via a nonlinear mapping to a higher dimensional feature space where the analysis is

performed by a PCA. Independent Component Analysis (ICA) [33, 85] assumes non-Gaussian signals and minimizes statistical dependence between the signals, using higher order statistics.

Chapter 8 apply a number of methods for obtaining sparse shape models and compares them to the PCA model.

3.5 Sparse Data

In order to estimate the shape model parameters of an unseen shape, full point correspondence is usually needed to be able to project the shape into the parameter space. Obtaining full point correspondence might not be possible in some applications due to restrictions such as acquisition and computation time, dosage (CT) and cost. In such applications there is a need for registration of dense models to incomplete data and for parameter estimation of the unseen shape. The requirements for introducing online industrial CT scanners for scanning pig carcasses in abattoirs are very demanding, so in an application where the goal is to fit a PDM to a new observation it would be a major advantage if full point correspondence is not necessary. A scheme for estimation of shape model parameters without the use of point correspondence is introduced in chapter 9.

Fleute and Lavallée [59, 60] apply an extended ICP algorithm for registration of contours from intra-operatively acquired 2D X-ray images to pre-operatively 3D shape models. In [163] van Assen *et al.* propose a method for fitting a dense model to sparse data. Model points near sparse data points are propagated onto void areas using a Gaussian kernel in order to achieve (pseudo-) correspondence making it possible to estimate model parameters. The framework is applied to segmentation of cardiac MRI data and different sparsity schemes are tested. Rajamani *et al.* [126–129] formulated an algorithm for matching a PDM to sparse digitized points to create patient specific models for pre-operative planning. A linear system of equations is solved to obtain a least squares fit of the model to the digitized points. A Mahalanobis distance based regularization term and M-estimator based weighting of the digitized points are included in the matching algorithm.

Contributions

This chapter summarizes the main results obtained in part II.

4.1 Classification of Pig Carcasses

Chapter 6 investigates the use of CT as a reference when determining the LMP of pig carcasses using online equipment. Today the calibration of online equipment for measuring the LMP, is done by relating their respective measurements to a manual dissection obtained by an expert butcher. Only highly trained butchers are involved in such a dissection and the accuracy of these calibrations are limited by that of the dissection method. There is a significant difference between butchers and countries as reported by Nissen *et al.* [116]. Olsen *et al.* [119] report that, in general, variations between butchers are more important than variations between copies of the same type of instrument when calibrating instruments to manual dissection. CT and MRI have often been suggested as future references for calibration cf. e.g. [31, 133]. Traditionally the number of meat voxels is determined and related to the amount of meat obtained from a manual dissection of the same carcass. Figure 4.1 shows an example of half a pig carcass prepared for scanning.

Instead of calibration against a manual dissection chapter 6 investigates calibration of a virtual dissection via CT against the full weight of pig carcasses, based



Figure 4.1: Left side of a carcass prepared and ready for scanning (Courtesy of DMRI).

on the data described in section 2.4.1. The weight of the pig carcasses can be measured as accurately as necessary using an appropriate scale and as such is better suited as a reference for calibration of the CT-based virtual dissection. It enables the definition of CT as a new reference for calibration of online equipment without the use of the less accurate manually based measurements in a manual dissection. In the method suggested the voxels of the volume are classified into one of three classes, fat, meat or bone using a contextual Bayes classifier [99, 105]. The densities of the tissue types are approximated by modeling the weight of the carcass as a linear combination of the segmented tissue volumes using robust linear regression. The carcass weight is modeled very accurately ($R^2 = 0.9994$, RMSEP= 83.6g), cf. figure 4.2(a) and it is therefore suggested as a reference for calibration of online equipment. Having obtained the density estimates, the carcass weight can be predicted, but more importantly, a CT-based LMP can be computed, which can be used as a reference for calibration of online equipment.

In order to substitute the present reference (manual dissection) which is the basis for paying the farmer, either the CT-based LMP should be calibrated against the present LMP or the CT-based LMP should just substitute it. A significant offset (-3.07 ± 0.57 units of LMP) is found between the two methods, cf. figure 4.2(b). Based on the results presented in chapter 6 it is recommended to define the LMP directly based on the virtual dissection of CT scans and use this as the future reference for calibration of online equipment. Replacing the manually determined LMP with CT based LMP will improve the calibration problem significantly, even though the lack of a perfect relationship is an important issue. Disregarding the fixed costs related to the purchase of a CT scanner and installing it in a trailer, the lower costs using CT is a considerable advantage compared to manual dissection. If only the maintenance of the scanner is taken into account alongside the salary of the operators, a CT based LMP costs less

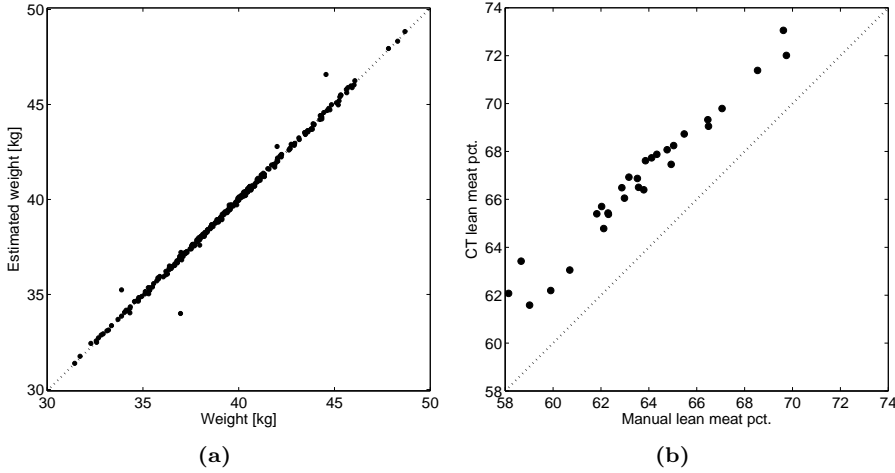


Figure 4.2: (a) CT estimated weight versus measured weight. (b) LMP estimated by manual dissection versus CT estimated LMP.

than half that of a manual dissection.

4.2 Building a Point Distribution Model

The design of robotic tools for automation of labor intense cutting procedures of pig carcasses in abattoirs is a very complex task. Traditionally a trial-and-error approach is used when testing each small change in tool design on a number of carcasses. This iterative approach is very slow, costly and it is difficult to determine how well suited a tool is for cutting a whole population of carcasses.

Chapter 7 proposes a procedure for constructing a 3D point distribution model when faced with highly anisotropic 2D CT scans. It includes segmentation, surface reconstruction from an implicit surface obtained using TPS radial basis functions [162], registration by a modified Iterative Closest Point algorithm [15], building a compact model based on Principal Components Analysis [36, 37] and applying model selection using Parallel Analysis [83]. The algorithms are applied on a specific bone structure from 33 porcine carcasses, cf. section 2.4.2. Figure 4.3 shows the mean shape of the model and the PCA-based model where each of the 8 modes of variation are perturbed $-3/+3$ std. from the mean shape.

A PDM can be useful in a number of ways when developing slaughterhouse

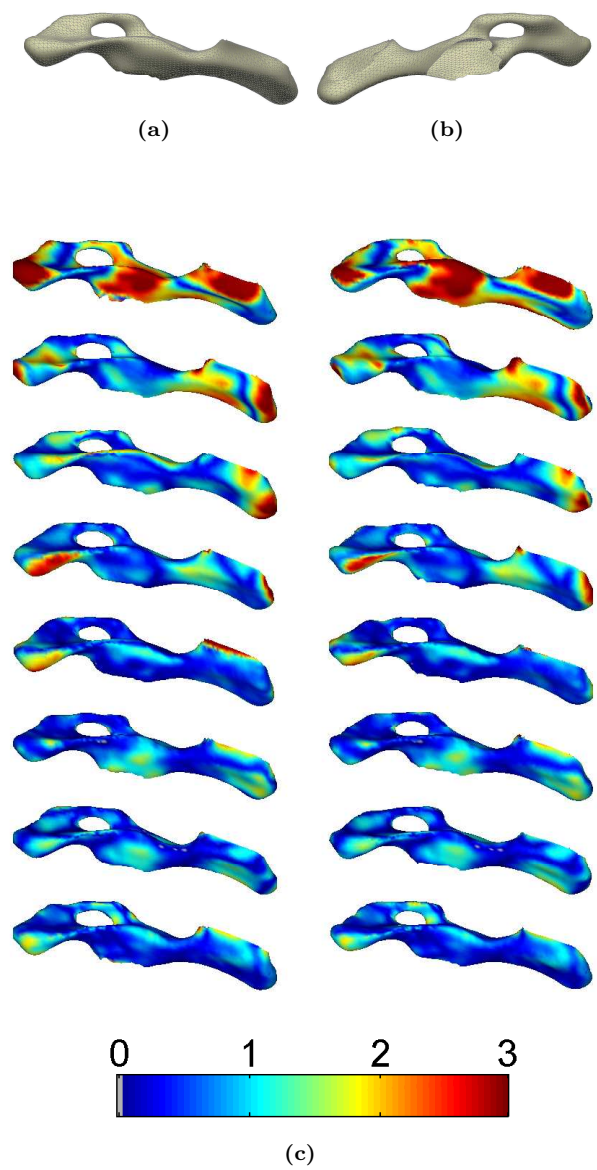


Figure 4.3: (a) & (b) Mean shape seen from two different views. (c) PCA based PDM. Left and right columns are perturbed $-3/+3$ std. from the mean shape. Rows are modes 1-8. The colors show the distance to the mean surface, from blue through red (0-3mm).

robotic tools for doing specific operations such as cutting bones and joints. Of course the quantification of biological variation is of great interest, i.e. how much do specific measures vary over the population. Compared to the standard trial-and-error methods presently used in tool development this information can save a lot of time because the initial tool design can be made based on the model. If the bone model is imported into a CAD system it enables the engineer to test different tool designs on the computer. The model can also be used for prediction, e.g. if the location of a certain part of a bone is known, the model can predict where the rest of the bone is or where other specific parts are located. These are some of the obvious ways of using point distribution models in robotic tool design. In online applications the new bones can be described by the model parameters and this can e.g. be used for deciding the use of the specific part of the carcass.

4.3 Sparse Point Distribution Models

Due to the nature of the PCA, models based on the PCA have a tendency to reveal modes of variation that are global in the sense that they are linear combinations of all of the point coordinates of a shape and therefore difficult to interpret. In recent years methods for obtaining more sparse modes of variation have been proposed, cf. [118, 142, 150, 173]. These are sparse in the sense that the modes of variation are linear combinations of only a subset of point coordinates, i.e. revealing more spatially localized modes that are easier to interpret. In medical applications it is often of interest to be able to model pathologies that are spatially localized.

Chapter 8 compares four sparse PDM's to one based on PCA [36]. The four models are orthogonal rotation by the varimax method (VM) [93], thresholds of small absolute valued loadings of both the PCA (Th. PCA) [25] and the varimax (Th. VM) methods, and finally the SPCA method proposed by Zou *et al.* [173]. Applying a threshold on the varimax rotated loadings have not previously been reported. A quantitative comparison is performed by measuring the reconstruction error and the explained variance of the models. The algorithms are applied on a specific bone structure from 33 porcine carcasses, cf. section 2.4.2.

In figure 4.4 the 5 models are compared with the same level of sparsity. It is found that SPCA is not the best sparse model for this specific application of modeling dense 3D surfaces of bones. The SPCA algorithm does not seem to converge properly, which may be a consequence of the specific application. Instead the proposed threshold varimax model outperforms both the varimax model and the threshold PCA model, making it the preferred sparse model for the application. The standard PCA model has the smallest reconstruction er-

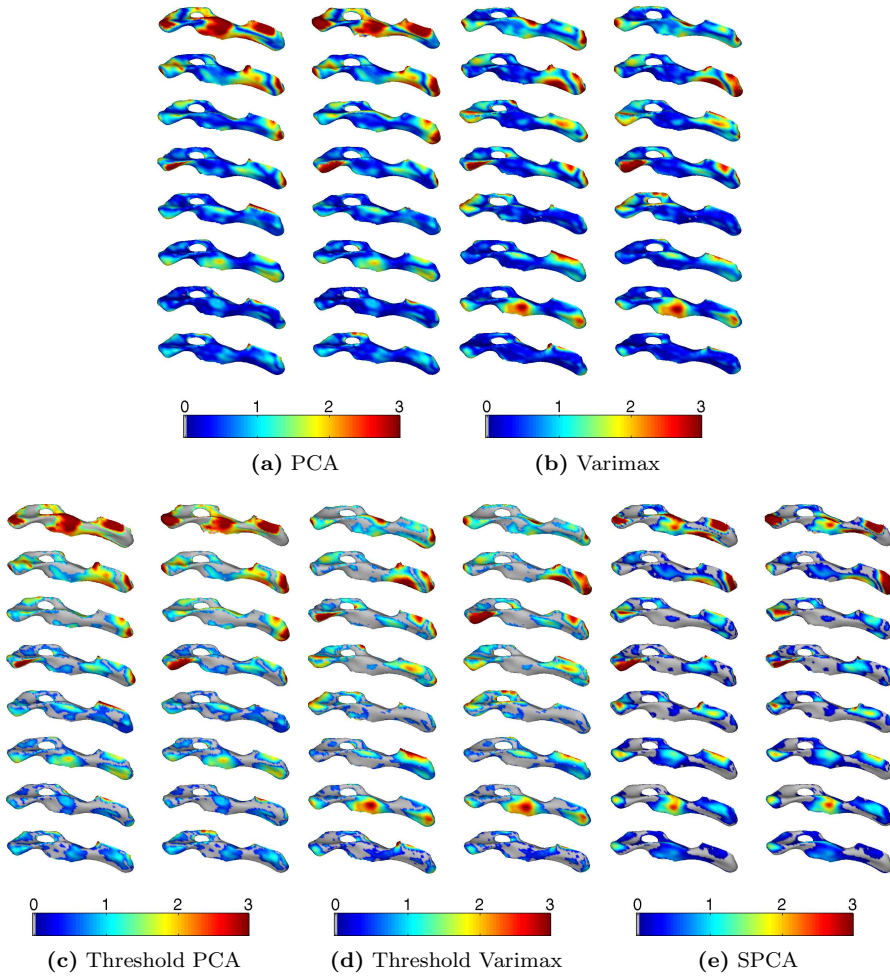


Figure 4.4: 5 shape models are compared. (a) PCA, (b) Varimax, (c) Threshold PCA, (d) Threshold Varimax, (e) Sparse PCA. Left and right columns for each model are perturbed $-3/+3$ std., respectively, from the mean shape. Rows are modes 1-8. The color coding shows the distance to the mean surface, from blue through red ($> 0 \rightarrow 3\text{mm}$). Zero distance is denoted gray. A sparsity level of 30% non-zero loadings is chosen for the three sparse models.

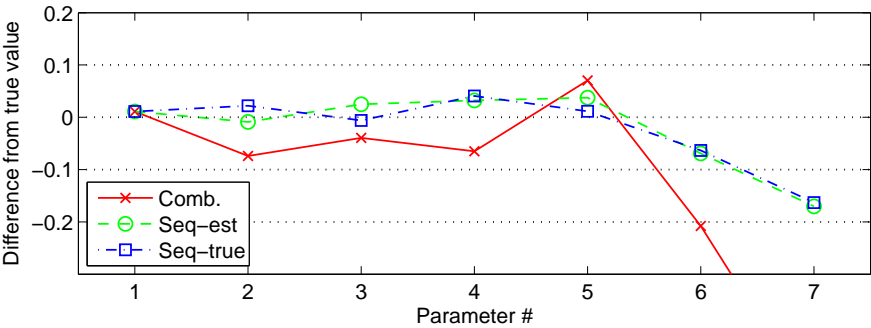
ror, but also contains more global modes of variation which are more difficult to interpret. The Varimax model explains less variation, has more interpretable modes and a slightly larger reconstruction error. For the three sparse models a sparsity level of 30% non-zero loadings was applied. The SPCA model is found not to converge to a suitable solution on the present data set. This results in a very poor reconstruction error compared to the other models. Applying a threshold to the PCA model results in a reconstruction error slightly larger than the full PCA model, but at the same level as the VM and Th. VM models. The Th. VM is considered superior to the Th. PCA since it has a similar performance, but with less total variation explained by the model. This is caused by the choice of a common sparsity level for all modes, considering the more uniform distribution of the explained variance of the VM based models. The interpretation also seems to reveal slightly more localized modes, especially those of higher order, i.e. 5-8. Based on that the Th. VM seems better at capturing the important variation.

Sparse models are not only appropriate for applications where the interpretation of localized structures is of interest, but also for applications where speed and memory are issues due to the nature of the models, e.g. in online applications in abattoirs.

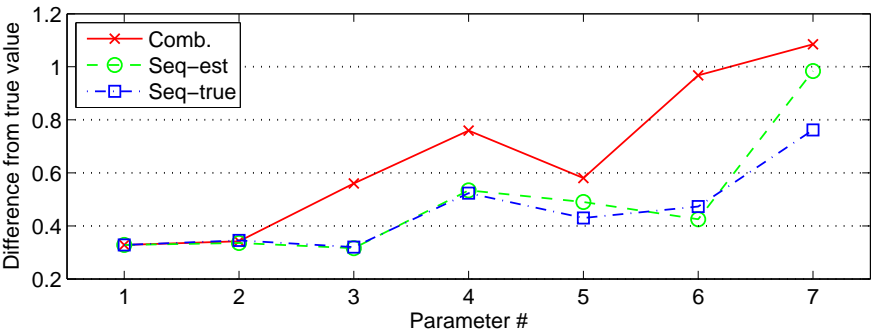
4.4 Fitting a PDM to Sparse Data

Statistical shape models (SSM), or PDM's, are often used to characterize unknown shapes in terms of model parameters which can be used for classification or regression. In order to estimate the shape model parameters of an unknown shape, full point correspondence is usually needed to be able to project the shape into the parameter space. Obtaining full point correspondence might not be possible in some applications due to restrictions such as acquisition and computation time, dosage (CT) and cost. In such applications there is a need for registration of dense models to incomplete data and for parameter estimation of the unseen shape.

In chapter 9 the focus is on how accurate the model parameters can be estimated. For applications where the parameters are used for classification or regression it is important to quantify how trustworthy this estimate is. An iterative Gauss-Newton optimization algorithm, cf. [12, 104], is proposed for fitting a SSM to unseen data using sampled distance maps. It is investigated on dense data, without requiring point correspondence. The proposed method is applied to a SSM of a porcine bone structure, described in section 2.4.2, which can be used in a robotic tool in an abattoir.



(a) Mean



(b) Std.

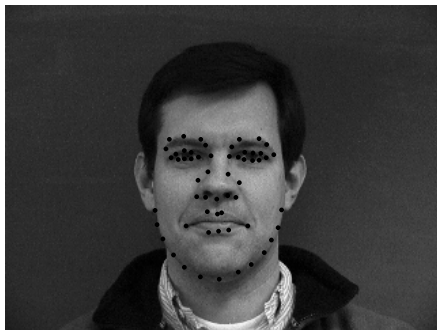
Figure 4.5: Difference between estimated and true parameter values for the three optimization schemes.

Figure 4.5 shows the results of the leave-one-out validation of parameter estimates for the data set. Three primary modes of the statistical shape model can be estimated with a mean difference between $[-0.01, 0.02]$ std. and with a std. of the difference within 0.34. This is done using a sequential estimation scheme (seq-est) where each parameter is estimated sequentially with previous parameters fixed. The difference between the true and the estimated rms error is below 0.01 mm. The rms error decreases when increasing the number of modes, but the parameter estimates are only reliable enough for the first 3 modes in the present application. The model parameters are interesting as they can be used to obtain a relation to specific quality measures of the carcasses.

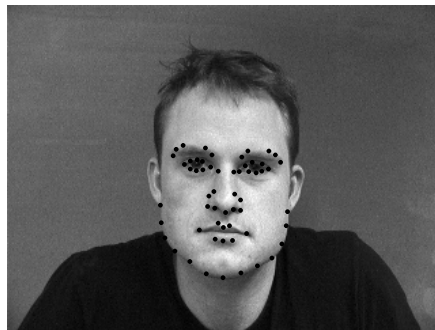
4.5 Accelerated Non-Rigid Image Registration

Chapter 10 presents the acceleration of an image registration algorithm proposed by Cootes *et al.* [39–41], that applies a grid-based warp function parameterized by the displacement of the grid-nodes. By composition of simple diffeomorphic transformations of nodes in the grid, more complex but also diffeomorphic deformation fields can be obtained. Using an appropriate kernel function in the interpolation scheme ensures the diffeomorphic nature of the deformation field. This registration algorithm is formulated using the inverse compositional optimization scheme proposed by Baker and Matthews [12]. It is a Gauss-Newton approach in which the Jacobian and the estimated Hessian can be pre-computed. The memory requirements of standard non-rigid registration algorithms are very demanding. The sparse structure of the Jacobian and Hessian is exploited to obtain a memory efficient algorithm. A comparison to a standard Gauss-Newton approach, as proposed by Lucas and Kanade [104], is performed on 5 3D CT-volumes of the hind part of pig carcasses. The algorithm has a two-fold increase in speed compared to the Lucas-Kanade based algorithm.

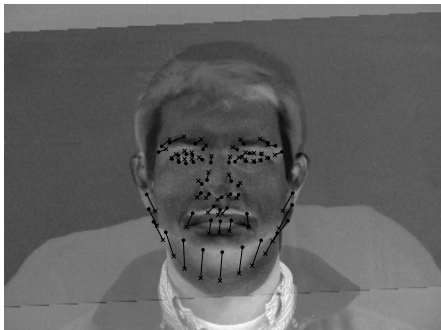
An additional benefit of the Gauss-Newton approach is the ease of which addition of soft constraints on the registration can be added, e.g. from landmarks. This is shown for a 2D affine transformation. Guiding the image registration using a few landmarks as constraints is likely to improve the speed and final result, cf. figure 4.5.



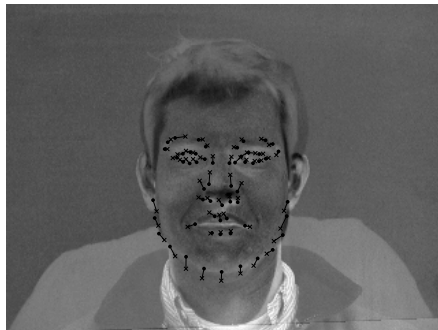
(a) Input image.



(b) Target image.



(c) Difference image, without landmark constraints.



(d) Difference image, with landmark constraints.

Figure 4.6: 2D affine registration of 2 images with and without landmark constraints.

Discussion and Conclusion

This chapter discusses the results obtained in part II in relation to the objectives of the thesis, cf. section 1.1 and presents some concluding remarks.

5.1 Discussion

Several aspects have been treated in this thesis relating medical imaging methodologies to applications in the meat industry.

One objective of the thesis is to investigate the use of CT for measuring the LMP as a common EU reference for classification of pig carcasses. This has previously been suggested but the problem for the previous studies has been that they relate a method that is believed to be very accurate (CT) to an old reference method which is less accurate (manual dissection). This makes it difficult to validate the accuracy of the new method, since the only "ground truth" available is affected by manual intervention. In chapter 6 it is suggested to segment the CT volume into three tissue classes, for modeling the weight of the carcass, which can be measured very accurately. The calibration is done against an accurate measure instead of against a manual dissection prone to operator dependent differences. The LMP can subsequently be determined directly from the model. The problem with this approach is that three tissue classes do not necessarily correspond exactly to the tissue classes of a manual dissection. This

can be caused by inaccuracies and/or differences in the segmentation method and/or in the manual dissection. Chapter 6 reports a very accurate prediction of the carcass weight, but also a significant bias in the prediction of the LMP based on manual dissection, hence it is therefore argued that the CT based LMP is more accurate and is more suitable as a reference for calibration of online equipment. A more accurate reference method for calibration of online equipment is necessary in order to ensure uniform classification of pig carcasses and thereby comparable standards throughout the EU.

The second major objective is to build a statistical shape model of a specific bone structure from a set of CT-scanned pig carcasses. This is meant as an aid for developers of robotic tools for abattoirs. Chapter 7 presents methods for this, given very anisotropic CT data as is the case for the data set described in section 2.4.2. Specific choices are made regarding the various steps and for each step other methods could be applied, but the need for this depends solely on the demands of the specific application the shape model is intended for, and is left for future work. The segmentation of the bone contours is presently done in 2D so it would be interesting to apply 3D methods for obtaining the surface constraints that are used when estimating the 3D implicit surface. Applying compactly supported RBF's and iterative methods for solving the system of equations would also enable the reconstruction of larger parts of bone structures with even finer details available. Optimizing the correspondence is also an issue that should be addressed in future work, e.g. by MDL-like methods or by applying nonrigid image registration as described in chapter 10. The compact shape model obtained is based on a PCA and it describes the major biological shape variation of the bone structure with only 8 parameters. With this model developers of robotic tools are able to test the tools in a CAD system before actually producing the tools, and moreover test the tools on the population of carcasses. Today each test of a tool design is done in the workshop on the actual pig carcass which is not necessarily representative of the distribution of carcasses. Furthermore such a test is destructive in the sense that it cannot be repeated on the same carcass, making it more difficult to compare changes in tool design. A shape model with an interface to a CAD system would therefore entail huge advantages compared to the way tool design is done today. Statistical shape models can also be used for relating the shape of specific muscles to other types of quality measures. Online applications of CT could include segmentation of specific bones or muscles based on statistical shape models, again relating shape to other measures of quality.

The parameters of a PCA based statistical shape model are global in the sense that they are linear combinations of the full set of point coordinates of the shape. This makes the parameters of the PCA based model hard to interpret spatially. Chapter 8 is related to the third objective of the thesis. It compares the PCA based model to other types of shape models that are more sparse in

the sense that the parameters are linear combinations only of a subset of point coordinates, i.e. spatially localized, and therefore easier to interpret. The models are compared by their explained variance and reconstruction error. The SPCA model turns out not to be appropriate for the dense 3D surfaces compared to the other methods. The model of choice is the proposed Threshold Varimax method, which reveals the best tradeoff between sparsity, reconstruction error and interpretability. In future work it would be interesting to compare these to other methods, such as e.g. ICA or Localized Components Analysis (LoCA), for obtaining localized and easier interpretable parameters. Applying sparse models does reveal more interpretable shape parameters of the specific bone structure and this with a model size of less than 1/3 of the PCA based model, making it better suited for online applications where speed and memory are crucial issues.

The final objective of the thesis is to investigate how statistical shape models can be applied to sparse data, i.e. data where only a subset of the information is available e.g. certain CT slices of a bone structure. Full point correspondence is necessary in order to project a new shape into the shape space obtaining its shape parameters. If point correspondence is not available some kind of registration is necessary. Chapter 9 proposes a method for estimation of shape model parameters without the use of point correspondence. It uses distance maps and a Gauss-Newton optimization scheme, and it can be viewed as non-rigid image registration constrained by a statistical shape model. The method is validated using the the corresponding points making it comparable to the shape parameters obtained by projection. For the most important parameters the two methods reveal very similar results. In future work the effect of reducing the amount of data, and how it is sampled, will be investigated, and this will be extremely useful in online applications since it enables the estimation of shape parameters without the need for full point correspondence, i.e. less data is necessary to be acquired by the CT scanner.

5.2 Conclusion

This thesis is the product of highly interdisciplinary work and should be viewed as a bridge between the different worlds of medical imaging and the meat industry. Through specific applications related to the Danish Meat Research Institute, it is demonstrated that non-invasive imaging and image analysis are very strong tools for obtaining detailed information of very complex structures. Results are presented either through scientific publications focusing on methodological contributions or through technical papers focusing on more application oriented aspects.

There is great potential in applying CT as a non-invasive modality in the meat industry, both offline for making population based studies and models of shape, for analyzing carcass composition etc. and, in the future, also for online applications improving the quality measures of pig carcasses for optimization of the use of each pig carcass.

Part II

Contributions

Virtual Dissection of Pig Carcasses

Martin Vester-Christensen, Søren G. H. Erbou, Mads F. Hansen, Eli V. Olsen, Lars B. Christensen, Marchen Hviid, Bjarne K. Ersbøll and Rasmus Larsen

Abstract

This paper proposes the use of computed tomography (CT) as a reference method for estimating the lean meat percentage (LMP) of pig carcasses. The current reference is manual dissection which has a limited accuracy due to variability between butchers. A contextual Bayesian classification scheme is applied to classify volume elements of full body CT-scans of pig carcasses into three tissue types. A linear model describes the relation between voxels and the full weight of the half carcass, which can be determined more accurately than that of the lean meat content. 299 half pig carcasses were weighed and CT-scanned. The explained variance of the model was $R^2 = 0.9994$ with a root-mean-squared error of prediction of 83.6g. Applying this method as a reference will ensure a more robust calibration of sensors for measuring the LMP, which is less prone to variation induced by manual intervention.

6.1 Introduction

Throughout the European Union (EU) the lean meat percentage (LMP) is used for classifying pig carcasses and is defined as the ratio of weighed lean meat versus the weight of the pig carcass. Measuring the LMP is typically done using ultrasound or optical sensors which are calibrated towards a common manual dissection method of half pig carcasses, cf. Commission of the European Communities (EC) [32] and Walstra and Merkus [169]. The accuracy and precision

of these calibrations are limited by that of the dissection method. Only highly trained butchers are involved in such a dissection. Even so there is still a significant difference between butchers as reported by Nissen *et al.* [116]. The maximum difference in estimated LMP between 8 butchers is found to be 1.96 LMP units and the jointing of the carcasses is found to be a critical point in the EU dissection method. Furthermore variation between countries were also found. Olsen *et al.* [119] report that in general variations between butchers is more important than variations between copies of the same type of instrument, when calibrating instruments to manual dissection.

X-ray computed tomography (CT), cf. Cho *et al.* [28], is a non-invasive technique that measures the radio-density of a material, i.e. the relative attenuation of X-rays through the material and is measured in the Hounsfield scale. The scale is calibrated such that air is at -1000 Hounsfield Units (HU) and water at 0 HU, making HU-values comparable across scanners and settings. Fat tissue is usually around -60 HU, meat tissue around $+60$ HU and bone tissue above ~ 150 HU. The CT-volume consists of discrete volume elements (voxels) and are not necessarily isotropic. Voxels might also consist of more than one class of tissue. The latter is denoted partial volume effects (PVE) and results in overlapping probability density functions (pdf) of the different tissues. Figure 6.1 shows a typical histogram in the fat/meat range for a CT-scanned pig carcass. The left peak represents fat and the right peak represents meat. Bone is above the range shown.

The fixed Hounsfield scale of CT is a major reason for using CT instead of magnetic resonance imaging (MRI) because it is comparable across scanners. Applying different settings, or protocols, in a specific CT-scanner has been shown by Christensen *et al.* [30] to give quite robust results w.r.t. LMP. Based on 23 pig carcasses and using 7 different protocols they find a maximum difference of 0.27 LMP units and a maximum difference in the estimated carcass weight of 0.22 kg.

Typically a simple threshold in the CT histogram is used to distinguish fat, meat and bone tissue, but this will often result in errors caused by noise in the reconstruction, artifacts and PVE.

Several attempts have been made on calibration of CT-scans of pigs carcasses to predict the lean meat content of manual dissections. Glasbey and Robinson [64] derive and compare estimators of tissue volumes in CT-images taking mixed pixels, or PVE, of fat and meat into account. A moment-based estimator performs best in both a simulation study and in a particular application where tissue composition of sheep is estimated. The improvement in precision is reported to be minor compared to Cavalieri sampling, cf. Roberts *et al.* [132].

Dobrowolski *et al.* [46] and Romvári *et al.* [133] use thresholds in the histogram

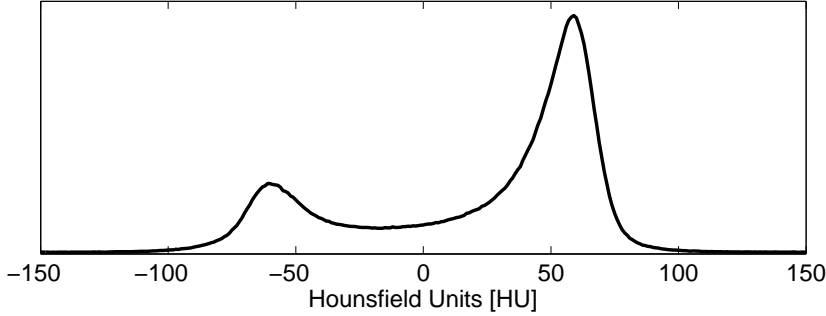


Figure 6.1: Histogram of a CT-volume of a pig carcass. The ordinate is scaled to show the distribution of fat (left) and meat voxels (right).

of CT and Collewet *et al.* [31] of MRI scans to segment meat voxels. In these studies partial least-squares regression (PLSR) of histogram values is applied to model the dissected lean meat content. Table 6.1 summarizes their results along with those of Johansen *et al.* [89]. R^2 is the explained variance and RMSEP/C are the root-mean-squared errors of prediction/calibration. Johansen *et al.* [89] apply thresholds to the histogram of 15 anatomically chosen slices of 120 CT-scanned carcasses of lamb to segment fat and meat tissue. A multidimensional PLSR model is applied on the histogram values of fat and meat to predict the corresponding weights in a manual dissection. The RMSEP of the meat content is reported to be 772g before and 561g after bias correction, with an $R^2 = 0.96$. Common for the above mentioned methods is that they only take into account the histogram value of the voxel to be classified and not any of the neighboring voxels.

Lyckegaard *et al.* [105] apply a multivariate Bayesian 2D contextual classification scheme to each slice as described by Larsen [99]. Certain combinations of neighboring voxels are taken into account modeled in a Bayesian scheme with priors obtained from thresholds in the histogram. Linear regression is used to estimate the parameters of a model mapping the volume of fat, meat and bone to the total weight of the carcass, with an $R^2 = 0.991$ and a RMSEP= 584g.

This paper presents an experiment consisting of 299 pig carcasses, which are weighed and CT-scanned. Applying methods from image processing along with a contextual classification scheme the CT-volume is classified into several types of tissue. A linear model determines the mapping from voxels to the full weight of the half carcass, which is then used for estimating the CT-based LMP.

Paper	Dobrowolski <i>et al.</i> [46]	Collewet <i>et al.</i> [31]	Romvári <i>et al.</i> [133]
Modality	CT (full, 150 sl.)	MRI (full)	CT (full)
Vox/spac. [mm]	—/—	[0.77, 1.02, 8]/10	[~ 1 , ~ 1 , 10]/10
Comment	1/2 pig carc.	1/2 pig carc.	1/2 pig carc.
Amount	60	120	60
R^2	0.990	—	0.992
RMSEP/C [g]	270/—	465/400	—/232
Bias [g]	16	—	—
Paper	Johansen <i>et al.</i> [89]	Lyckegaard <i>et al.</i> [105]	
Modality	CT (15 anat. sl.)	CT (full)	
Vox/spac. [mm]	[0.78, 0.78, 3]/var.	[1, 1, 10]/10	
Comment	Lamb carc.	1/2 pig carc.	
Amount	120	57	
R^2	0.961	0.991	
RMSEP/C [g]	772/—	584/554	
Bias [g]	530	—	

Table 6.1: Previous work. Papers [46], [31], [133] and [89] apply PLSR-methods on histograms for meat pixels, modeling the lean meat weight obtained from dissection. [105] apply a contextual Bayesian classifier and linear regression for predicting the full weight of half carcasses. R^2 is the explained variance, RMSEP/C are the rms errors of prediction/calibration, with the corresponding bias reported in some cases.

6.2 Materials and Methods

6.2.1 Data

299 carcasses representing the Danish pig population with respect to weight (warm slaughter weight) and fatness (fat depth between the 2nd and 3rd hind-most thoracic vertebra) were selected. Half of which were gilts and the rest castrates. The pigs were slaughtered at a commercial Danish abattoir and cooled. The day after slaughtering the left side of the carcasses were prepared for dissection. The preparation was done according to Walstra and Merkus [169], but the head except the cheek and toes were cut off before scanning. All half carcasses were weighed on a DIGI DS160 industrial scale with an accuracy of 20g. Subsequently they were scanned with a GE HiSpeed CT/i single-slice scanner. In the following the term carcass weight denotes the weight of the scanned left side of the carcass. The scanning protocol parameters were: 140kV voltage, $0.9 \times 0.9 \times 10$ mm voxel size, 0.7mm spot size and 10mm between slice centers, yielding 299 CT-volumes of pig carcasses with corresponding weight. Figure 6.2 shows a left side of a carcass prepared and ready for scanning.

6.2.2 Full Dissection

Of the 299 carcasses scanned, a subsample of 29 carcasses with 13 gilts and 16 castrates were selected. The subsample was selected representing the distribu-

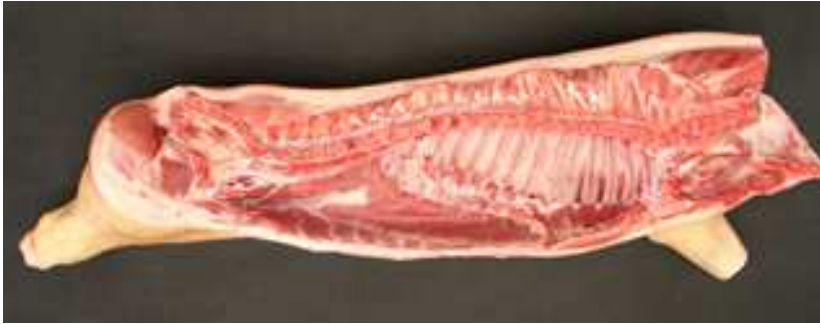


Figure 6.2: Left side of a carcass prepared and ready for scanning.

tion of weight and fatness. After scanning a full dissection was made on the same carcass to calculate the lean meat content. The LMP is defined as the ratio of the meat and the total weight of the carcass exclusive head and toes. Full dissection is not standardized yet. In this trial the meat fraction consists of all muscles including tendons, fascia and periosts. Periosts appear by, e.g. extraction of ribs, femur bone in ham and front part. Tendons from certain muscles stretch around the bones as e.g. *Biceps brachii* and other muscles in the front part and ham. These tendons are not left entirely on the muscles, but are cut off where they touch the bone. The fat fraction consists of subcutaneous and inter-muscular fat including skin and glands, veins and loose membrane tissue. Loose membrane tissue is defined as all membrane tissue which can be lifted between two fingers and can be cut without damaging the underlying muscle. The bone fraction consists of all bones including cartilage. No bones are scraped to remove periosts or remains of tendon.

6.2.3 Tissue Classification

For identifying meat voxels, the tissue from CT is traditionally classified by applying thresholds in the histogram. This method introduces errors due to PVE as mentioned earlier. In the current work a multivariate Bayesian 2D contextual classification scheme is applied to each slice, cf. Larsen [99]. Background voxels are removed and tissue voxels are classified into three classes; fat, meat and bone. The classifier takes certain configurations of neighboring voxels into account as well as the prior probability as described in Lyckegaard *et al.* [105]. All fat, meat and bone tissue irrespective of their anatomical position are regarded as belonging to the same corresponding class. As a postprocessing step the bones are morphologically closed such that marrow will be part of the bone class. In CT skin voxels are more similar to meat. When comparing the LMP obtained by CT to that obtained by manual dissection the skin is segmented separately and

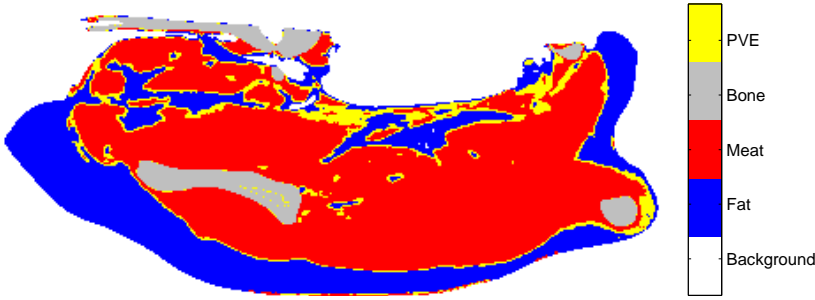


Figure 6.3: Partial volume effects shown in a CT-slice from the shoulder part of half a pig carcass. Yellow denotes voxels with a probability above 0.5 and below 1.0 of belonging to the meat class.

considered as fat such that the LMP can be computed according to Commission of the European Communities (EC) [32]. Segmentation of the skin is done using mathematical morphology, cf. Gonzalez and Woods [70].

6.2.4 Density Estimation

Estimating the weight of a carcass requires an approximation of the densities ρ of the tissue types in every voxel. The carcass weight is modeled as a linear combination of the weights of the tissue classes. Labeling of a particular voxel is done by choosing the class with *maximum a posteriori* (MAP) probability, see Larsen [99]. The MAP model applied for a single carcass with three tissue classes is,

$$w_i = \rho_f n_f v + \rho_m n_m v + \rho_b n_b v + \epsilon_i, \quad (6.1)$$

where v is the voxel volume, n_f, n_m and n_b are the number of voxels classified as fat, meat and bone, respectively. w_i is the measured i^{th} carcass weight and $\epsilon_i \in N(0, \sigma_i)$. Including all carcasses and using linear regression the density approximations can be obtained.

Due to PVE a single voxel might consist of more than one type of tissue. However, in the model in eq. (6.1) each voxel is labeled as either fat, meat or bone. Including PVE in the model can be done using the value of the posterior probability of each class. Thus all voxels have a weighted contribution from all classes. Figure 6.3 illustrates the issues with PVE. The figure depicts a slice in the shoulder part of the carcass where voxels with a posterior probability above 0.5 and below 1 of belonging to the meat class are yellow, indicating that they contain something else than meat. These are primarily located where the meat

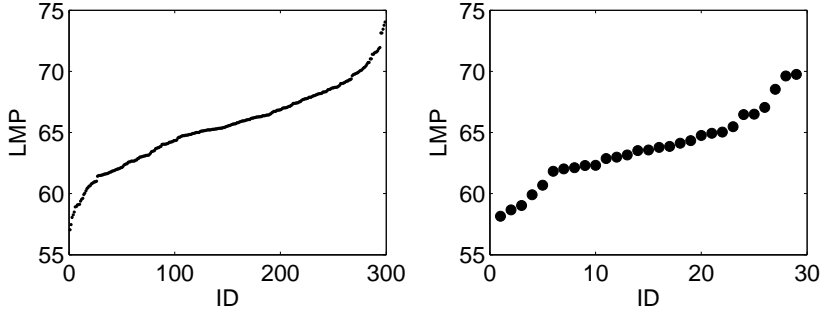


Figure 6.4: The resulting LMP estimated by CT, 299 carcasses (left), and by manual dissection, 29 carcasses (right), sorted by LMP.

interfaces with fat. Integrating PVE in the carcass weight model yields

$$w_i = \rho_f \sum_{i=1}^n p(c_f|x_i)v + \rho_m \sum_{i=1}^n p(c_m|x_i)v + \rho_b \sum_{i=1}^n p(c_b|x_i)v + \epsilon_i, \quad (6.2)$$

where n is the total number of voxels. $p(c_f|x_i)$, $p(c_m|x_i)$ and $p(c_b|x_i)$ are the posterior probabilities of voxel x_i belonging to the fat, meat or bone class respectively, and $\epsilon_i \in N(0, \sigma_i)$. Both the MAP and the PVE model are applied with and without an additional constant term c , for comparison.

To avoid the effect of outliers the linear regression problem is solved using an iteratively re-weighted least-squares algorithm presented in Holland and Welsch [80]. Leave-one-out cross-validation is performed and the root-mean-squared error of the residuals of prediction (RMSEP) is reported as well as the bias and explained variance (R^2).

6.3 Results and Discussion

6.3.1 Comparison with manual dissection

Figure 6.4 shows the range of LMP for both CT (left) and manual dissection (right) and is approximately [55, 75] units. The half carcass weight range is seen in figure 6.6 to be approximately [31, 49]kg. Data used in both dissection methods cover the variation in LMP of the Danish pig population. Table 6.2 and figure 6.5 compare the estimated tissue content from the manually dissected carcasses with the corresponding estimate from the CT-dissection. On average CT-scanning identifies 1227g more meat, 968g less fat and 225g less bone in a

Tissue Type	Fat	Meat	Bone
Res. mean \pm std [%]	2.49 \pm 0.55	-3.07 \pm 0.57	0.58 \pm 0.33
Res. mean \pm std [g]	968 \pm 181	-1227 \pm 210	227 \pm 130

Table 6.2: Mean and standard deviations of the residuals obtained by comparing CT-dissection with manual dissection.

Model	R^2	RMSEP [g]	Bias [g]
MAP	0.9994	83.6	2.6
PVE	0.9994	79.0	2.3
MAP+ c	0.9994	79.1	1.8
PVE+ c	0.9994	75.5	1.7

Table 6.3: Predictive performance of the two models, with and without a constant term c , using leave-one-out cross-validation.

carcass than manual dissection. It is expected that tissues like tendons, fascia, periosts and cartilage, which consist of protein, will be considered as meat in a CT-scan. From the description of the three main groups of tissue, meat, fat and bone obtained with manual dissection, it is seen that only a part of all protein-containing tissues is defined as meat. It seems reasonable that the limitations of manual separation together with the definition of meat cause the main contribution to the differences between LMP determined with CT and manual dissection. Furthermore table 6.2 indicates a larger standard deviation when compared to the mean value of the residuals of the bone class than for the meat and fat classes.

6.3.2 Modeling total weight

Applying both models described in section 6.2.4 reveal similar results. Figure 6.6 shows a plot of the correlation between estimated carcass weight and measured carcass weight using the MAP model, cf. eq. (6.1). The estimated parameters and correlation results for the MAP model and the PVE model, with and without constant terms c , are reported in table 6.3. In all regressions the robust algorithm detects 5 outliers, which are identified as errors in the data acquisition. These are subsequently removed in the calculation of the parameters and the correlation results as well.

Table 6.3 shows that the four models perform equally well with large correlations to the measured weight. Applying a one way analysis of variance (ANOVA) on the weight estimates from all models reveals no significant difference between them. Including a constant term would make the definition of the LMP ambiguous, since it does not belong to a specific tissue class. Subsequently the simple

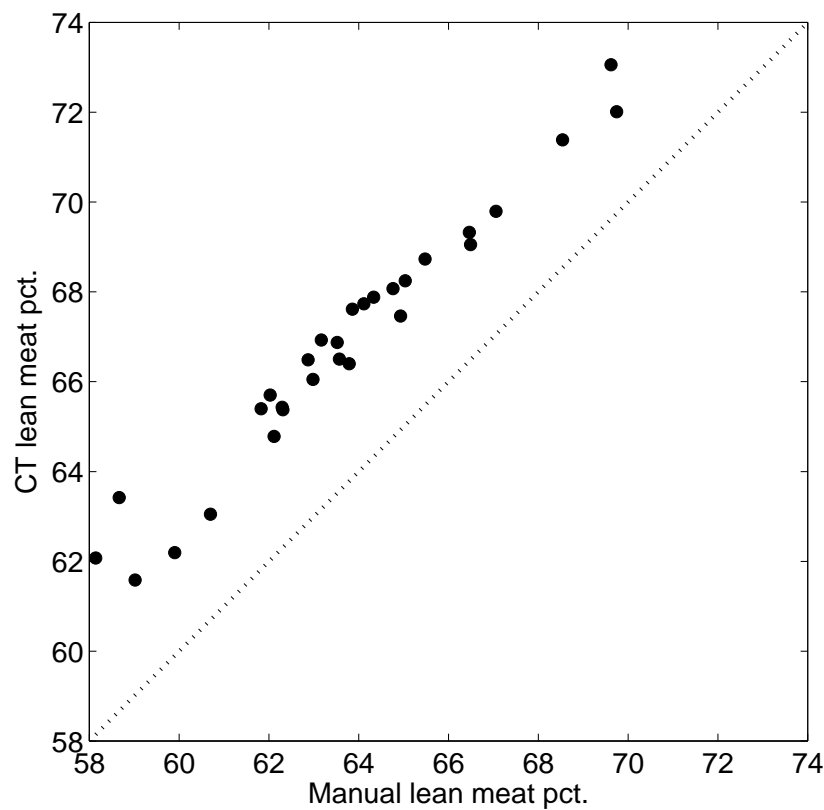


Figure 6.5: LMP estimated by manual dissection versus CT-estimated LMP using the MAP model.

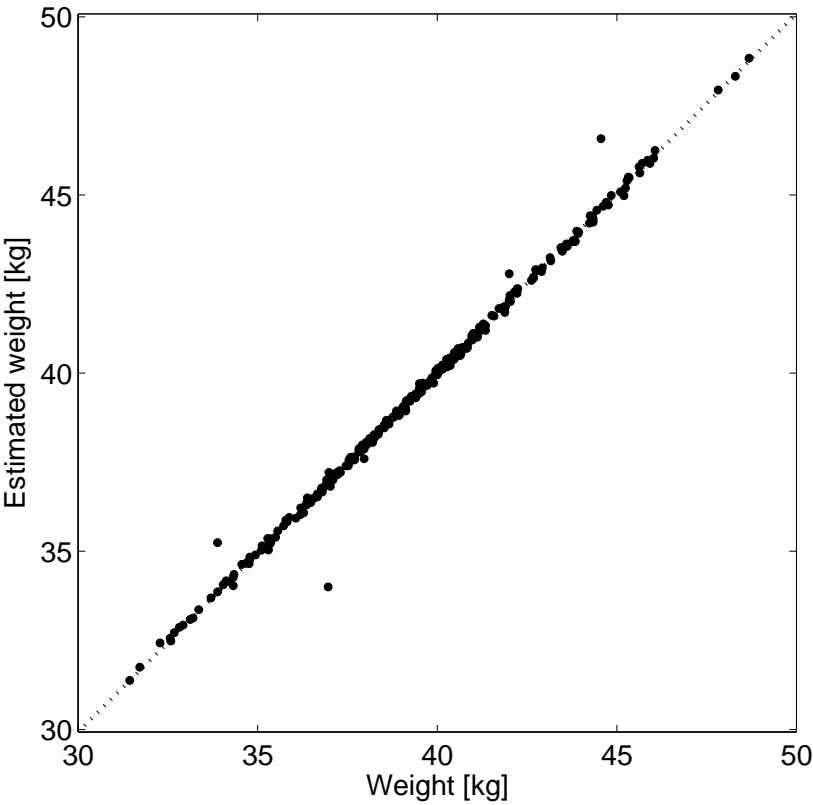


Figure 6.6: Estimated weight using the MAP model versus measured weight.

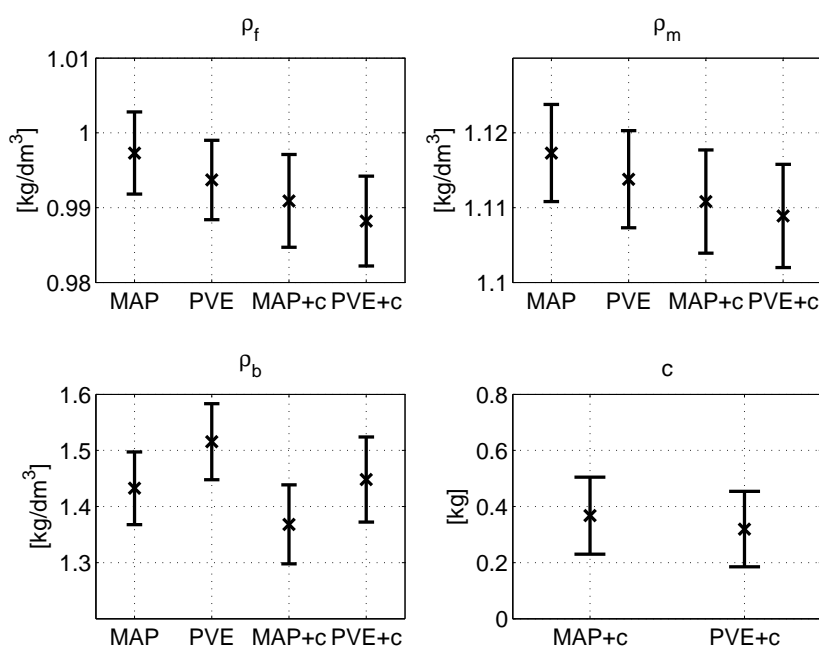


Figure 6.7: Estimated parameters and their corresponding 95% confidence intervals for the two models, with and without a constant term c .

Model	ρ_f [CI]	ρ_m [CI]	ρ_b [CI]	c [CI]
MAP	0.997 [0.992 1.003]	1.117 [1.111 1.124]	1.433 [1.368 1.497]	
PVE	0.994 [0.988 0.999]	1.114 [1.107 1.120]	1.516 [1.448 1.583]	
MAP+c	0.991 [0.985 0.997]	1.111 [1.104 1.118]	1.368 [1.298 1.438]	0.367 [0.230 0.505]
PVE+c	0.988 [0.982 0.994]	1.109 [1.102 1.116]	1.448 [1.372 1.524]	0.319 [0.185 0.454]

Table 6.4: The resulting parameters for the MAP and PVE models excluding and including a constant term c . 95% confidence intervals are shown in brackets.

MAP model without a constant term is preferable. Modeling PVE has no effect on the quality of the predicted weight. In a randomly chosen carcass only 1.6% of all the voxels classified as meat have a fat probability above 0.1. Thus the influence of PVE is very limited with regards to the total weight. Table 6.4 and figure 6.7 show that the values of the parameters of fat and meat are not significantly different when comparing the PVE and MAP models contrary to the bone parameter. A voxel containing both bone and soft tissue will tend to be classified by the MAP model as bone. A voxel in the PVE model contributes to all tissue types. This results in more bone voxels using MAP than using PVE.

All in all the results obtained are very encouraging when compared to table 6.1. The simple MAP based model has an explained variance of $R^2 = 0.9994$, a bias of 2.6g and RMSEP=83.6g estimated using leave-one-out cross-validation.

For all models the three tissue types are assumed to have the same properties regardless of their anatomical position. Thus the parameters ρ_f , ρ_m , and ρ_b can be viewed as the average density of all fat, meat and bone in the half carcass. Previous work (Romvári *et al.* [133]) reports the importance of modeling different tissue properties, and they do this by manually separating the CT-volume into three carcass parts. This is prone to operator dependent errors. In this study, it is argued that using average tissue properties yields a more robust estimate of the carcass weight due to operator independency. It should be noted though, that the parameters might not have a strict physical interpretation as densities of the specific tissue classes.

Even though there is a clear definition of which of the three tissue fractions the tendons and glands etc. belong to, the specific butcher makes the final decision. Nissen *et al.* [116] report considerable variation between butchers and separation of muscles and especially small muscles are very dependent on the butcher. The contribution from the butchers affects mainly the precision of dissection and less the average result. Two main sources of error are present when calibrating online instruments to LMP. One is the error or variation, which expresses the imperfect relation between the reference LMP and the online measurements, including the accuracy of the online measurements, and the other one is the accuracy of the dependent variable, i.e. the reference LMP.

LMP based on CT is a very promising candidate for an instrumental reference for pig carcass classification. Previous investigations have shown very high repeatability. However, before CT-LMP can be used as a global reference, it has to be documented that the results can be reproduced independently of CT-instruments, time and pig population. The method described in this paper is based on a specific scanning protocol and reconstruction algorithm. Although the method seems robust to these factors a thorough documentation will be necessary. Especially the choice of slice thickness, resolution and reconstruction algorithm has to be general and available on all types and makes of CT-scanners. A possible tool to ensure the reproducibility over time, including a possible bias correction, could be calibration using phantoms that mimic different types of carcasses with known values of LMP. How such phantoms should be designed is an area of future research.

Replacing the manually determined LMP with CT-based LMP will improve the calibration problem significantly, even though the lack of a perfect relationship is an important issue. Disregarding the fixed costs related to the purchase of a CT-scanner and installing it in a trailer, the lower costs using CT is a considerable advantage compared to manual dissection. If only the maintenance of the scanner is taken into account alongside the salary of the operators, a CT-based LMP costs less than half that of a manual dissection.

6.4 Conclusions

Previous work shows CT-based methods as robust compared to manual dissection, and as such constitute a suitable reference. This work presents a robust and accurate calibration reference, where variation due to manual intervention is minimized. Given a model of the carcass weight, the LMP can be estimated based on the classification of the volume elements (voxels) in the CT-volume. Using this more accurate method as a reference will make the calibration procedures of other LMP sensors much more standardized and accurate.

Contextual models based on segmentation of the carcass into three classes is validated on a large data set of 299 half pig carcasses. Incorporating the influence of partial volume effects is found not to be significantly better than a maximum-a-posteriori model. All models correlate very well with the full weight of the half carcasses, with the simple maximum-a-posteriori based model being the model of choice. The model has an explained variance of $R^2 = 0.9994$, a bias of 2.6g and a root-mean-squared error of prediction of RMSEP=83.6g. These results are very encouraging compared to previous work, for which reason the method is suggested as a new reference for calibration of sensors used for pig carcass grading.

Acknowledgements

The CT data was provided by the Danish Meat Research Institute as a part of the project "The Virtual Slaughterhouse" funded by the Danish Pig Levy Fund and the Directorate for Food, Fisheries and Agri Business.

From CT to Shape Model

Søren G. H. Erbou, Bjarne K. Ersbøll

Abstract

This paper proposes a procedure for constructing a 3D point distribution model when faced with highly anisotropic 2D CT scans. It includes segmentation, surface reconstruction from implicit surfaces, registration by a modified Iterative Closest Point algorithm, a model based on Principal Components Analysis and model selection using Parallel Analysis. The algorithms are applied on a specific bone structure from 33 porcine carcasses and the model can be used for optimizing and validating the functionality of robotic tools in slaughterhouses. Robotic tools are important in slaughterhouses when automating labor intensive procedures. However, developing these tools can be very time consuming due to the biological variation in carcasses.

7.1 Introduction

The design of robotic tools for automation of labor intense cutting procedures of porcine carcasses in slaughterhouses is a very complex task. Traditionally a trial-and-error approach is used when testing each small change in tool design on a number of carcasses. This iterative approach is very slow, costly and it is difficult to determine how well suited a tool is for cutting a whole population of carcasses. This paper describes a procedure for registration of 3D surfaces of porcine bone structures extracted from highly anisotropic 2D CT scans of 33 carcasses and construction of a compact 3D point distribution model (PDM). The model quantifies biological variation of the bone structures and can be used for developing robotic tools for the Danish Meat Research Institute (DMRI).

PDM's are often used to encapsulate biological variation in medical applications. [34, 36, 37] describe such compact 2D PDM's. The model assumes that corresponding contour points are available on a data set of similar shapes. Removal of variation due to translation, rotation and scaling is done by applying the Generalized Procrustes Analysis (GPA), cf. [72] and [47]. This ensures that the remaining variation is due to true shape variability only. Performing a principal components analysis (PCA), cf. [87], on the coordinates enables a compact description of the shape variability by discarding modes that represent minimal variation. The model is truncated to consist only of the eigenvectors with the t largest eigenvalues, based on the assumption that the smaller eigenvalues only represent noise. PDM's are typically used to obtain a deeper understanding of biological variation of many types of shapes, e.g. corpus callosum, the heart, bones and joints, cf. [37] and [149]. Often it is studies of normal vs. abnormal/pathological cases that are of interest.

Defining landmarks on shapes manually can be a very time consuming and tedious procedure, especially in 3D. [162] describe a method for estimating an implicit surface in 3D by use of thin-plate-spline (TPS) radial basis functions (RBF) and variational interpolation. Points on the surface are used as constraints when solving a system of linear equations subject to minimizing the aggregate curvature, revealing a set of weighted basis functions that can be used to sample the surface isotropic and arbitrarily dense. When faced with highly non-uniform distributed point constraints the TPS solution is a reasonable choice for sampling the surface more densely.

Registration of shapes consists of determining the optimum correspondence between shapes and this can be done using rigid or non-rigid methods. The Iterative Closest Point algorithm (ICP) by [15], obtains the rigid transform that minimizes the sum of Euclidian distances between corresponding points in an iterative manner. If the initialization is good, convergence is reached quite fast. Several authors have proposed improvements to the original ICP, e.g. including the surface normal or curvature measures and extending it to multiple view registration, cf. references in [137]. [108, 109, 172] present comprehensive surveys of image registration methods, both intensity-based and landmark-based. Some applicable non-rigid registration methods are described in [42, 134, 166]. Minimum Description Length (MDL) [43, 44] is an iterative method for optimizing point correspondences with an objective function based on information theory that promotes compact models. For 3D surfaces the MDL has only been applied to genus 0 topologies since they can be mapped to a sphere in a one-to-one manner (homeomorphic) cf. e.g. [61, 79]. Horkaew *et al.* [82] model the heart with two spheres and a number of boundaries. So far no work has been published applying the MDL for surface topologies higher than genus 0.

Typically not much attention is focused on model selection after applying the

PCA, or on methods to improve interpretation of the modes. Model selection, i.e. how to determine the number of principal components to retain can be done in a number of ways. [87] and [77] provide excellent overviews of many of these methods. Especially Parallel Analysis (PA) proposed by [83] has been shown to perform well as a criterion for model selection of statistical shape models, cf. [122]. [100] suggest a probabilistic framework for model selection based on either the noise adjusted PCA transform (Minimum Noise Fraction) or the Maximum Autocorrelation Factor (MAF) transform, where the log-likelihood is penalized using the Bayesian Information Criterion (BIC), cf. [138], or Akaikes Information Criterion (AIC), cf. [1].

7.2 Methods

In order to build a PDM as described in [37] corresponding points/landmarks are required. For surfaces in 3D automated methods for defining points and determining point correspondence are necessary. Several processing steps are applied in order to obtain a PDM of a surface based on CT-scans.

- 2D segmentation of bone contours from CT-scans.
- 3D implicit surface from 2D-contours.
- Registration.
- PDM.
- Model selection.

7.2.1 Segmentation

X-ray computed tomography (CT), cf. Cho *et al.* [28], is a non-invasive technique that measures the radio-density of a material, i.e. the relative attenuation of X-rays through the material and is measured in the Hounsfield scale. The scale is calibrated such that air is at -1000 Hounsfield Units (HU) and water at 0 HU, making HU-values comparable across scanners and settings. Fat tissue is usually around -60 HU, meat tissue around $+60$ HU and bone tissue above ~ 150 HU. Due to the large difference between soft tissue and bone tissue in the Hounsfield scale, a simple threshold can distinguish the two. The CT-volume consists of discrete volume elements (voxels) which are not necessarily isotropic. Voxels might also consist of more than one class of tissue, denoted partial volume effects (PVE), which results in overlapping probability density functions (pdf) of

the different tissues. This limits the degree of detail obtainable from the specific data set. Other artifacts also occur, mainly due to the data acquisition and the way the image is reconstructed from the raw CT data. Using mathematical morphology the segmentation of bones is made less sensitive to noise, resulting in a robust segmentation of closed bone contours in the images. The number of points along the contour is reduced by fitting a Fourier series to the points and sampling along the curve, taking curvature and sampling distance into account, cf. [130].

7.2.2 Implicit surface

An implicit surface is a mapping $f : \mathbb{R}^3 \rightarrow \mathbb{R}$ from coordinates to a scalar value. The surface is defined as the points in the volume where the scalar value is zero. The resampled points on the contours described in section 7.2.1 are used as constraints in 3D in the reconstruction of the bone surfaces using variational interpolation and RBF's, cf. [161, 162]. The aim is to estimate a function, $f(\mathbf{x})$ that minimizes some energy measure, usually the aggregate curvature, subject to some interpolation constraints. Using a linear combination of radial basis functions of the form $\phi(\mathbf{x}) = |\mathbf{x}|^3$ ensures that the energy function is minimized. Other basis functions can also be used, e.g. $\phi(\mathbf{x}) = |\mathbf{x}|$ [26]. These specific basis functions ensure the extension of TPS interpolation into 3D. A drawback of applying TPS interpolation is that constraints have global support, which limits the number of constraints that can be applied while obtaining a solution in reasonable time. Morse *et al.* [112] apply compactly supported basis functions which can be solved using many more constraints. The drawback of this is that they do not obtain the TPS solution and that some areas might not have any support when sampling the implicit surface. In the TPS solution areas of large curvature, e.g. sharp edges, need many constraints to be modeled properly. This is taken into account when resampling the contours as described previously. A radial basis function is centered on each data point. The interpolation function can then be written as:

$$f(\mathbf{x}) = \sum_{j=1}^k w_j \phi(\mathbf{x} - \mathbf{c}_j) + P(\mathbf{x}) \quad (7.1)$$

w_j are the weights, $\mathbf{c}_j = (c_j^x, c_j^y, c_j^z)$ are the locations of the constraints and $P(\mathbf{x})$ is a first order polynomial that accounts for linear and constant portions of f which ensures positive definiteness of the solution. The number of weights to estimate depends on the number of constraints. To ensure that the surface interpolates the constraints of values $h_i = f(\mathbf{c}_i)$, the constraints are substituted

into equation 7.1:

$$h_i = \sum_{j=1}^k w_j \phi(\mathbf{c}_i - \mathbf{c}_j) + P(\mathbf{c}_i) \quad (7.2)$$

This can be written as a system of linear equations, where $\phi_{ij} = \phi(\mathbf{c}_i - \mathbf{c}_j)$:

$$\begin{bmatrix} \phi_{11} & \phi_{12} & \dots & \phi_{1k} & 1 & c_1^x & c_1^y & c_1^z \\ \phi_{21} & \phi_{22} & \dots & \phi_{2k} & 1 & c_2^x & c_2^y & c_2^z \\ \vdots & \vdots & \ddots & \vdots & \vdots & \vdots & \vdots & \vdots \\ \phi_{k1} & \phi_{k2} & \dots & \phi_{kk} & 1 & c_k^x & c_k^y & c_k^z \\ 1 & 1 & \dots & 1 & 0 & 0 & 0 & 0 \\ c_1^x & c_2^x & \dots & c_k^x & 0 & 0 & 0 & 0 \\ c_1^y & c_2^y & \dots & c_k^y & 0 & 0 & 0 & 0 \\ c_1^z & c_2^z & \dots & c_k^z & 0 & 0 & 0 & 0 \end{bmatrix} \begin{bmatrix} w_1 \\ w_2 \\ \vdots \\ w_k \\ p_0 \\ p_1 \\ p_2 \\ p_3 \end{bmatrix} = \begin{bmatrix} h_1 \\ h_2 \\ \vdots \\ h_k \\ 0 \\ 0 \\ 0 \\ 0 \end{bmatrix} \quad (7.3)$$

Solving this system with respect to the weights can be done using standard methods and is straightforward up to a couple of thousands of constraints. In addition to the zero-valued constraints defined on the surface, additional constraints are needed to define the sign of the interior and exterior parts of the surface. A typical method is to place constraints at a small distance away from the surface contours along their normal and assign to them the positive or negative distance value.

When the weights are estimated, equation 7.1 can be used to resample the implicit function arbitrarily dense. $f(\mathbf{x})$ is resampled densely over the whole volume, and the isosurface at $f(\mathbf{x}) = 0$ is extracted by triangulation of the resampled volume similar to the "Marching Cubes" algorithm by [103]. The triangulated mesh is smoothed to avoid triangles that are nearly degenerate, cf. [156]. Only a specific rigid part of the bone structure is modeled in the present application therefore structures of no interest connected to the rigid part of the bone are removed manually.

7.2.3 Registration

The aim of registration is to estimate the optimal transformation between two objects or data sets in order to place them in a common coordinate frame. In this paper a modified ICP algorithm is applied, which determines the similarity transformation, i.e. rotation, translation and scaling that minimizes the euclidian distance between corresponding points, applies the transform, and then determines new corresponding closest points. This is done iteratively until convergence to a local minimum. The procedure requires a good initial estimate of the transform, which often can be acquired by aligning the principal directions of the data sets. Registration using ICP also requires a large amount of

overlap between the underlying shapes that the data sets represent in order for the search not to be trapped in a non-optimal local minimum. However, with a good initialization the convergence is reached quite fast. Non-rigid registration methods, e.g. [42, 134, 166] could be interesting to apply as well for comparison, but this is left for future work.

The modification of the ICP consists of not just choosing the closest point as corresponding point, and instead applying an algorithm similar to ray-racing, cf. [27, 137]. When the optimal transformation is given by the ICP, the mean curvature normal \mathbf{n}_i of the i^{th} point/vertex on the surface is estimated as the area-weighted mean of the normals in the triangles/faces adjacent to each vertex, cf. [45].

$$\mathbf{n}_i = \frac{1}{4A} \sum_{k=1}^f (\cot \alpha_k + \cot \beta_k)(v_i - v_k) \quad (7.4)$$

$\|\mathbf{n}_i\|$ is the value of the estimated mean curvature and A is the total area of the f faces adjacent to the vertex v_i . α_k and β_k are the remaining angles of the two faces which are opposite to the edge given by vertices v_k and v_i . The mean curvature normal could also be estimated as the mean of the adjacent face normals, but that would not be a robust estimate if the areas of each of the adjacent faces are not of similar size. The corresponding point is then restricted to be on a line along the mean curvature normal, at the location where it coincides with the surface, as long as the point-to-surface distance is within some limit. Otherwise the closest point on the surface is chosen. Especially around convex structures this modified ICP improves the registration compared to standard ICP. It might introduce minor discontinuities, e.g. near surface edges, but these are not considered to be an issue in the current data set and application.

Initially a specific shape is chosen as a reference and registered to all other shapes. In order to reduce the bias towards the specific reference shape, the mean shape of the initial registration is computed and then registered to all shapes. This procedure is done several times in order to reduce the bias towards the choice of initial reference shape, cf. [73]. Having obtained point correspondence between the mean reference shape and all original shapes, it is now possible to do statistical analysis on the distribution of the points, and to construct a compact model describing the shape variation. To account for translational, rotational and scaling effects a Generalized Procrustes Analysis is performed, cf. [47] and [72]. Given the point correspondence the procedure iteratively estimates the mean of the shapes and minimizes the Euclidian distance between the mean and each shape, applying translation, rotation and scaling of the shapes.

7.2.4 Point distribution model

PDM's were proposed by Cootes *et al.* as a compact way of describing shape variation in a data set [36, 37]. Let the n shapes, or in this case 3D surfaces, be represented by k corresponding 3D points, each arranged in a p -dimensional vector \mathbf{s} ($p = 3k$). The idea is to formulate a parameterized model of the form $\mathbf{s} = M(\mathbf{g})$ describing the variation seen in the data, where \mathbf{g} is a vector of shape parameters of the model M . The sample mean ($\bar{\mathbf{s}} = 1/n \sum_{i=1}^n \mathbf{s}_i$) and sample covariance matrix ($\mathbf{C} = 1/(n-1) \sum_{i=1}^n (\mathbf{s}_i - \bar{\mathbf{s}})(\mathbf{s}_i - \bar{\mathbf{s}})^T$) are then computed. Since the original parameter space is usually much larger than the number of observations ($p \gg n$) applying PCA on the covariance matrix is an obvious choice for dimensionality reduction, cf. [87]. The PCA determines the main axes (eigenvectors ϕ_i) of variation of the data and sorts them according to the amount of variation they describe (eigenvalues λ_i). The model, or principal components (PC), can then be formulated as a perturbation of the mean shape:

$$\mathbf{s} = \bar{\mathbf{s}} + \Phi \mathbf{g} \quad (7.5)$$

where Φ is the matrix composed of the eigenvectors ϕ_i . The model parameters of a new aligned shape \mathbf{s}' can be obtained by projecting it into the parameter space,

$$\mathbf{g}' = \Phi^T (\mathbf{s}' - \bar{\mathbf{s}}). \quad (7.6)$$

An important point to make when interpreting PDM's is that they are purely data-driven. They only show the variability expressed in the data from which they are built. Using such models for prediction should therefore be done with care, considering how well the data represent the population one is trying to predict features from.

7.2.5 Model selection

Only the first t eigenvectors of Φ is used in eq. (7.5) and (7.6), assuming that subsequent eigenvectors only contain noise. Often not much attention is focused on model selection after applying the PCA, or on methods to improve interpretation of the modes. Model selection, i.e. how to determine the number of principal components to retain can be done in a number of ways. [87] and [77] provide excellent overviews of many of these methods.

Working with data-driven models some level of noise is to be expected, often set to 5%. In such cases t should be chosen so that the sum of the first t eigenvalues only just exceeds 95% of the total variation. If no prior knowledge is at hand this method is not recommended. Another widely used method is a graphical

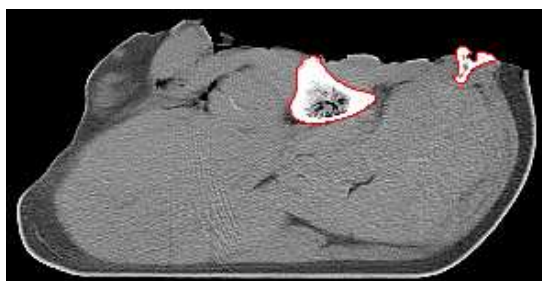
technique called the scree test, where the eigenvalues are plotted in descending order and only the modes above the "elbow" of the plot are kept. The problem with this method is that the "elbow" is not always well defined. The method used here is named parallel analysis (PA) and is a variant of that originally proposed by Horn [83]. In PA each variable is randomized across observations a number of times (e.g. 100 times). Each time a new PCA is computed and the eigenvalues are plotted in a scree plot alongside the eigenvalues of the PCA of the original data. Only the modes of the original data with values above the corresponding values of the randomized data should be kept. The eigenvalues of the randomized data gives an estimate of the amount variation that cannot be explained by chance alone. Using this level for model selection and only keeping modes of the original data with eigenvalues that are larger than that level is a conservative, but widely used, estimate.

7.3 Results

The data consists of 2D CT scans of 33 porcine carcasses separated along the medial plane, cf. figure 7.1(a). Only the right hand side of the half carcasses is used. Figure 7.1(b) shows an image of the bone structure in the ham of a pig carcass. Each slice has a thickness of 10mm with a spacing of 10mm between each slice. Voxel dimensions are $[x, y, z] = [0.88, 0.88, 10]$ mm. Approximately 30 scans per carcass are used in this application, covering the region around the pelvic bone which is modeled. On the order of 10000 points along bone contours is the typical result of the segmentation, cf. figure 7.1(c).

7.3.1 Surface Reconstruction

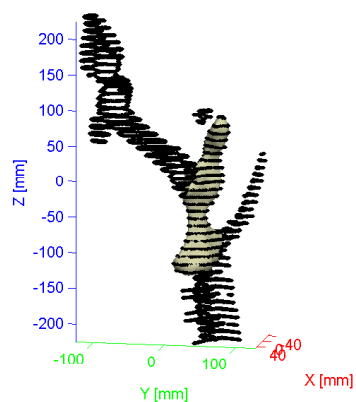
The number of contour points is reduced to around 2000 points when fitting a Fourier series to the points and resampling along the curve. The resolution in the image plane (x,y) is more than 10 times higher than in the z-direction, supporting the data reduction in the image plane before estimating the 3D surface. Each of these points are used as constraints in the estimation of the implicit surface. Furthermore, for each surface constraint used a corresponding constraint is introduced, which is placed perpendicular to each point constraint in the image plane. Assuming that the additional constraints should be in the image plane introduces an error, but since the distance to the surface is small compared to the entire volume ($< 1\%$ of the voxel dimension perpendicular to the image plane) this error is neglected. The implicit surface is re-sampled to an isotropic resolution $3 \times 3 \times 3$ mm, based on a trade-off between the computational complexity, the level of detail and the resolution of the CT-volume. An



(a) Slice



(b) Pelvic bone structure



(c) Surface

Figure 7.1: (a) shows a CT slice with the bone contour segmented (red). (b) shows an image of the bone structure in the ham of a pig carcass and (c) shows the segmented contour points for the hind part of a carcass with the estimated surface of the pelvic bone structure.

algorithm similar to the "Marching Cubes" algorithm by Lorensen *et al.* [103] is applied for obtaining a triangle based surface representation. Then the femur bone and part of the tail bone is cut away manually in order to end up with the pelvic bone structure of interest. Finally an algorithm for fairing the triangles, i.e. repairing nearly degenerate triangles is applied, cf. [156]. The specific part of the pelvic bone that is modeled has genus 1 topology, i.e. same topology as a torus, but with two open ends due to the parts that are removed manually.

All shapes are shown in figures 7.8 and 7.9. In general the surfaces seem reasonable with minor issues, e.g. small spikes near parts of the edges. It may seem that there for some shapes are kind of a bulging structure near the left end of the bone. This could be an effect of the additional constraints being placed in the image plane and the structure being far from orthogonal to the image plane. It should be noted though that the angle of view emphasizes this effect. The hole in the structure seems to be reconstructed in a reasonable way. An obvious way to improve the surface reconstruction would be to improve the segmentation of bone contours, e.g. by doing it in 3D instead of in 2D. In addition the additional constraints perpendicular to the surface could be estimated in 3D as well avoiding their restriction to be placed in the image plane. Using compactly supported basis functions and also iterative methods for solving the system of equations would also be of interest in comparison with the present work.

7.3.2 Registration

The modified ICP algorithm is used for registration of the surfaces. Optimization using the MDL method is not applied since the surface of interest has genus 1 topology. Figure 7.2 shows parts of two triangulated surfaces, where vertices of the dark gray bone is registered to the surface of the light gray bone. The black lines show the correspondence between vertices of one shape and the surface of the other shape along the direction of the estimated mean curvature normals for each vertex.

Shape no. 6 is chosen as a reference based on visual inspection and consists of 3815 vertices and 7397 faces. The reference shape is registered to all other shapes, and a mean shape is computed. The new mean shape is then used as a reference and registered to all shapes and a new mean is computed. This procedure converges in only 3 iterations determining the final point correspondence. After that the Generalized Procrustes Analysis is applied resulting in a data set of aligned shapes. Figure 7.3 shows the mean shape from two views.

Figure 7.4 shows box plots of distances from vertices in the mean shape to the surface of each of the shapes. Each box corresponds to the 1st and 3rd quartile, with the horizontal line showing the median. The reference shape does not have

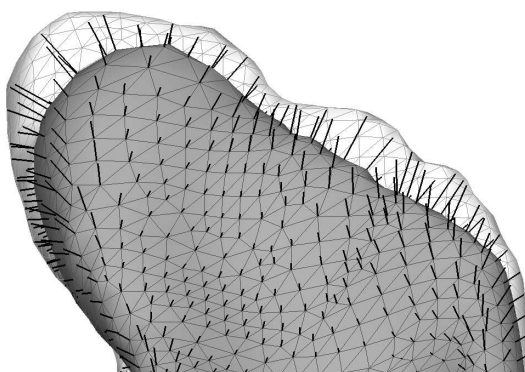


Figure 7.2: Triangulated surfaces of a small part of two bones. Black lines denote correspondence between vertices in the dark gray bone, and the surface of the light gray bone along the estimated mean curvature normal.

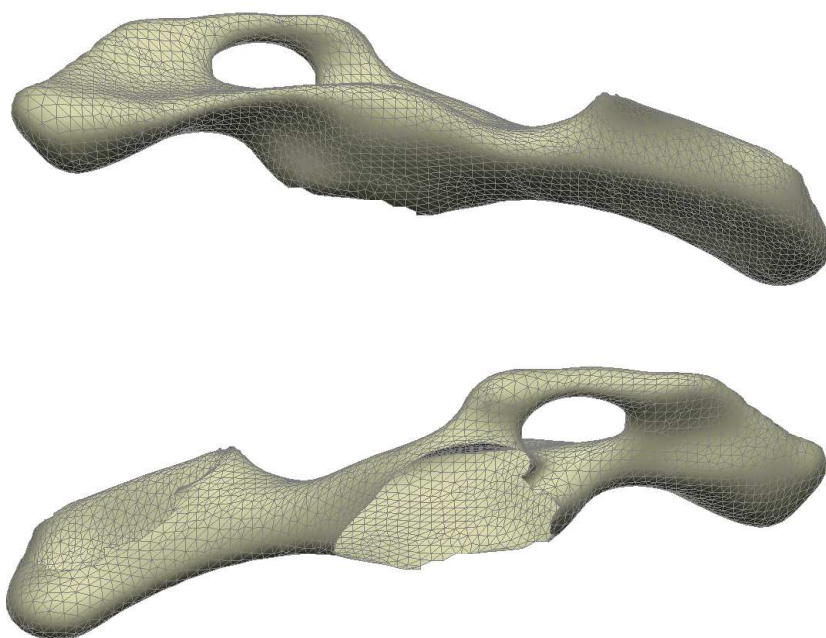


Figure 7.3: Mean shape seen from two different views.

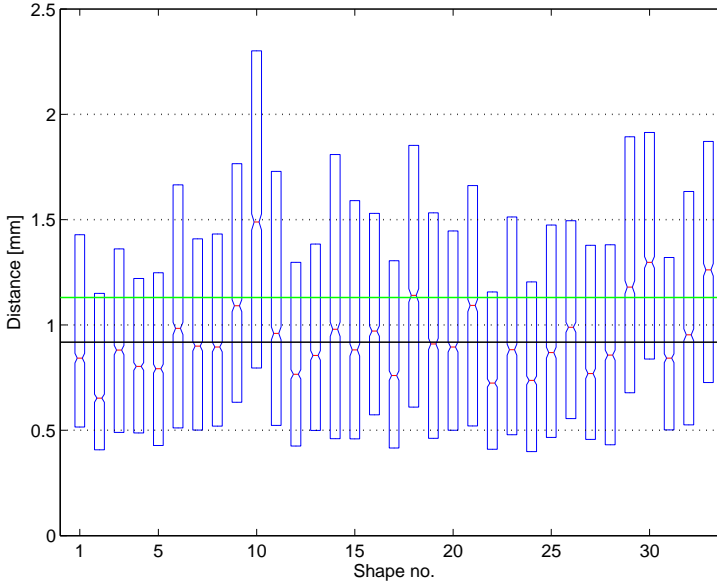


Figure 7.4: Plots of distances between vertices of the mean shape and the surface of each of the other shapes. Shape no. 8 is used as initial reference. Boxes denote lower quartile, median and upper quartile. The horizontal green line denotes the overall mean of the distances for each shape, which is $1.13 \pm 0.18\text{mm}$ (mean \pm std). The black line denotes the overall median (0.92mm).

the smallest median and interquartile distance to the mean reference shape, indicating that the mean reference shape is not particularly biased towards the initial reference shape. The overall mean distance between the shapes and the mean reference is $1.13 \pm 0.18\text{mm}$ (mean \pm std), shown by the green line. The black line shows the overall median, which is 0.92mm. Shape no. 10 seems to be the shape most different from the mean, based on the distribution of point-to-surface distances.

The modified ICP algorithm for registration seems to give reasonable results in the specific application. It would be interesting to compare it to non-rigid registration methods to see if a PDM then would capture some other/more interesting information.

7.3.3 Point Distribution Model

Each of the $n = 33$ shapes now consists of $m = 3815$ points/vertices in 3D, i.e. $p = 11445$ variables. Figure 7.5 shows the scree plot of the PCA and how the

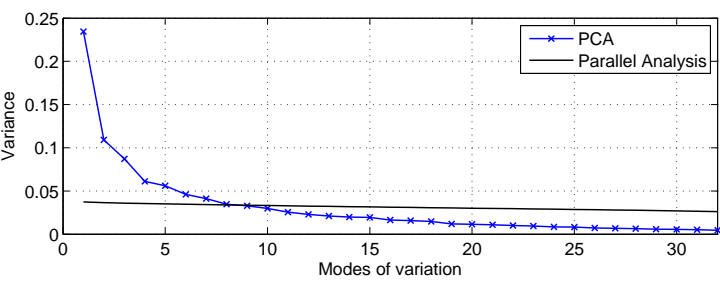


Figure 7.5: Model selection. Parallel Analysis (upper 95% CI) suggests to keep 8 modes of the original PCA, describing 67.0% of the total variation in the data.

Principal component	1	2	3	4	5	6	7	8
Variance explained [%]	23.5	10.9	8.7	6.1	5.6	4.6	4.1	3.5

Table 7.1: Variance explained by each mode in the PCA model. 8 modes explain 67.0% of the total variation.

final model is truncated to $t = 8$ modes, based on parallel analysis (upper 95% confidence limit). The first 8 modes of the PCA express 67.0% of the variation in the original data. cf. table 7.1.

Applying eq. 7.6 projects the shapes into the parameter space. Figure 7.6 shows scatter plots of this projection into parameter space with iso-contours at 1, 2 and 3 std. from the mean. The blue triangles denote the original reference shape (no. 6) and it should be noted that it is not an outlier in any of the modes and therefore a suitable choice of reference. The red squares show a shape (no. 22) that is an extreme in PC5 but not in the other modes. The green diamonds denote shape no. 10 which has the largest absolute value of mode 1. This corresponds well to figure 7.4 where shape no. 10 (cf. figure 7.8(j)) had larger distances to the mean shape than the other shapes and to the fact that PC1 alone expresses 23.5% of the variation in the original data.

Figure 7.7 shows the modes of the PCA based model. For each of the 8 modes (rows) two shapes are shown, varying the mode $-3/+3$ std. from the mean shape. The color coding shows the distance to the mean shape ranging from 0-3mm (blue→red). PC1 varies quite globally as expected from table 7.1. 3 spatial areas in the left, central and right part of the bone show large variation in PC1. PC1,2,4,5 all show variation in both ends of the bone. This makes the interpretation of the modes quite complex. PC5 and to some extent PC4 show variation around an edge which is partly due to registration errors. Still the PCA based PDM is a very compact representation of the biological variation reducing more than 11,000 variables to 8 parameters, explaining 67% of the

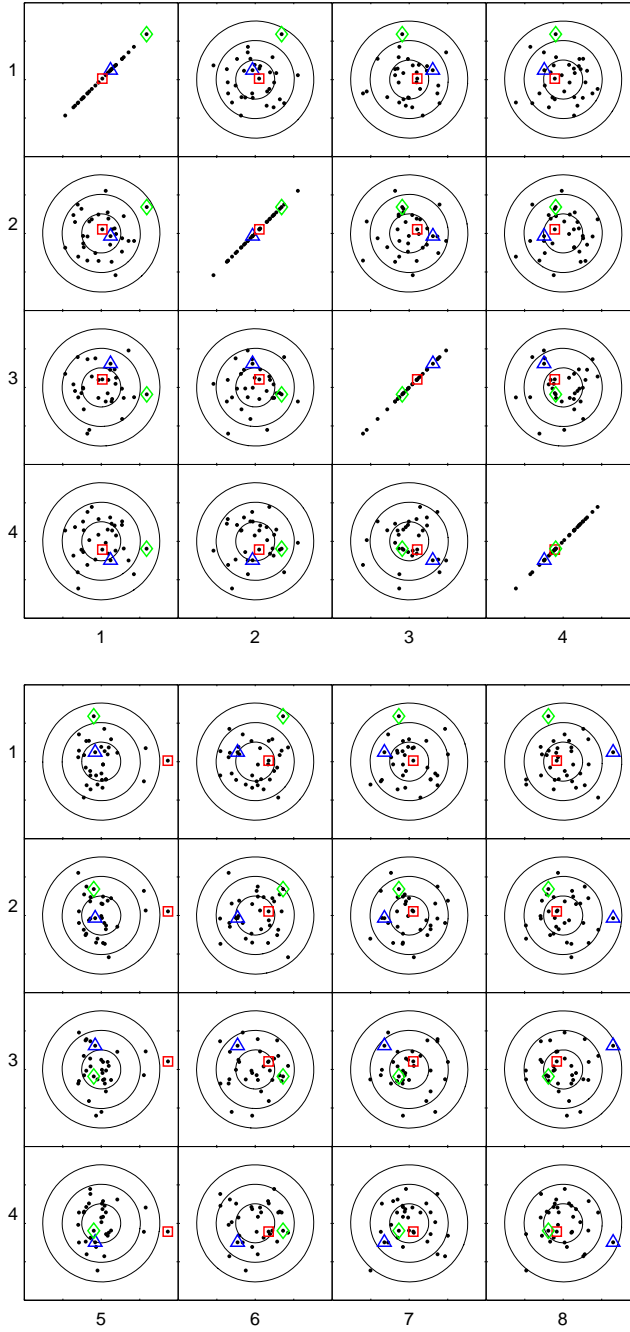


Figure 7.6: Scatter plots of the surfaces projected onto combinations of PCA modes. The blue triangles denote the original reference shape (no. 6) and the red squares show a shape (no. 22) is an extreme in mode 5, but not in the other modes. The green diamonds denote shape no. 10 which has the largest absolute value of mode 1. The black circles are iso-contours of 1, 2 and 3 std. of each parameter.

original variation. More sparse methods may reveal modes of variation that are easier to interpret, this is investigated in [54].

7.3.4 Discussion

A point distribution model can be useful in a number of ways when developing slaughterhouse robotic tools for doing specific operations such as cutting bones and joints. Of course the quantification of biological variation is of great interest, i.e. how much do specific measures vary over the population. Compared to the standard trial-and-error methods presently used in tool development this information can save a lot of time because the initial tool design can be made based on the model. If the bone model is imported into a CAD system it enables the engineer to test different tool designs on the computer. The model can also be used for prediction, e.g. if the location of a certain part of a bone is known, the model can predict where the rest of the bone is or where other specific parts are located. These are some of the obvious ways of using point distribution models in robotic tool design. In online applications the new bones can be described by the model parameters and this can e.g. be used for deciding the use of the specific part of the carcass. In such applications there are very tough time constraints for which reason some other ways of estimating the model parameters would be useful, without the demand for point correspondence. This is investigated in [53].

In future work some more elaborate ways of determining surface constraints before surface reconstruction should be investigated as well as testing compactly supported basis functions and iterative methods for solving the system of equations. Furthermore applying non-rigid registration methods for comparison, and other decompositions than PCA which might be easier interpretable, should be investigated.

7.4 Conclusion

This paper presents algorithms for obtaining a 3D point distribution model of bones from highly anisotropic 2D CT-scans. All the steps from segmentation, surface reconstruction, registration to the actual point distribution model are described.

2D contours are segmented from the CT-scans, fitted with a Fourier series and resampled less densely in the image plane. Points on the contours along with their normals are then used as constraints when estimating a 3D implicit sur-

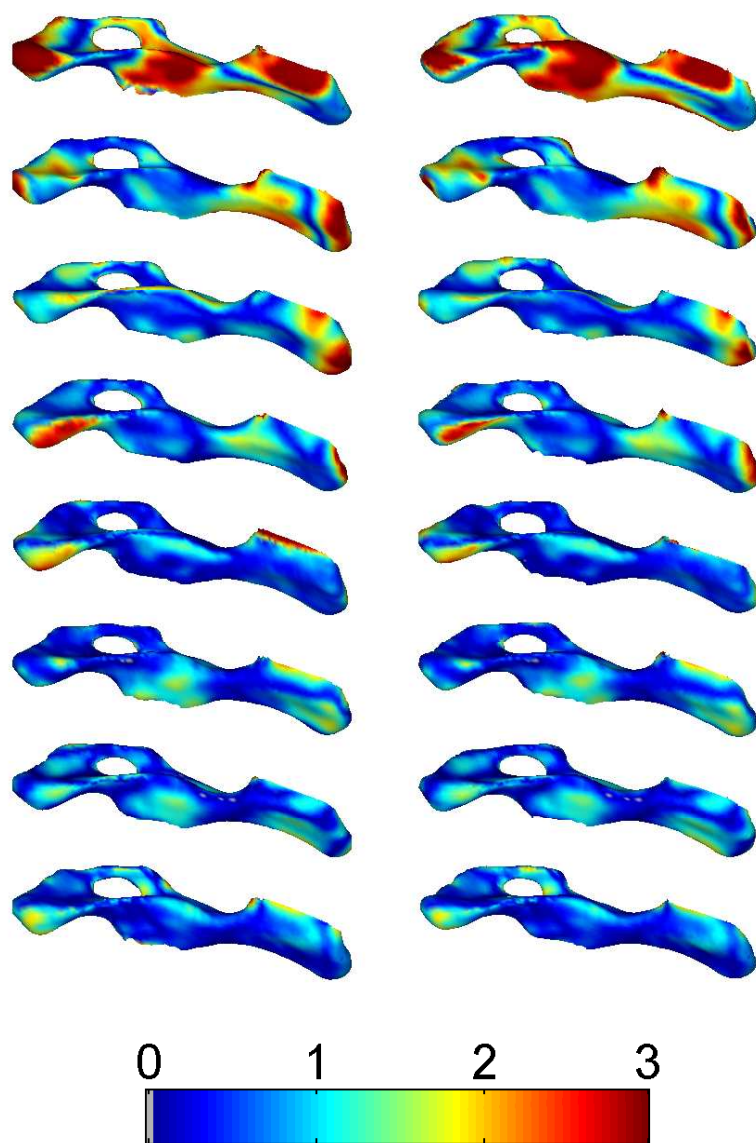


Figure 7.7: PCA based PDM. Left and right columns are perturbed $-3/+3$ std. from the mean shape. Rows are modes 1-8, cf. table 7.1. The color coding shows the distance to the mean surface, from blue through red (0-3mm).

face of the bone using Radial Basis Functions. Each surface is resampled more densely than the original resolution perpendicular to the image plane, and the densely sampled 3D surfaces are registered using an ICP based algorithm modified with a ray-tracing step to a mean shape which is based on a specific reference shape. A compact point distribution model is built based on Principal Components Analysis of corresponding point locations and parallel analysis is used for model selection.

The methods are applied to model bone structures of 33 CT-scanned pig carcasses and the model consists of 8 parameters describing 67% of the total variation of the original data.

The Danish Meat Research Institute is focused on using easy interpretable statistical shape models such as this in developing robotic tools for slaughterhouses. The quantification of the biological variation and the use of models in predictive ways can speed up the development process and facilitate more intelligent tool designs. Statistical shape models can also be used for incorporating prior knowledge in segmentation tasks of previously unseen data, or in online applications.

Acknowledgements

The authors would like to thank Eli V. Olsen, Lars B. Christensen and Finn Hansen from the Danish Meat Research Institute for their help in this work. The CT data was provided by the Danish Meat Research Institute as a part of the project "The Virtual Butcher" funded by the Danish Pig Levy Fund and the Directorate for Food, Fisheries and Agri Business.

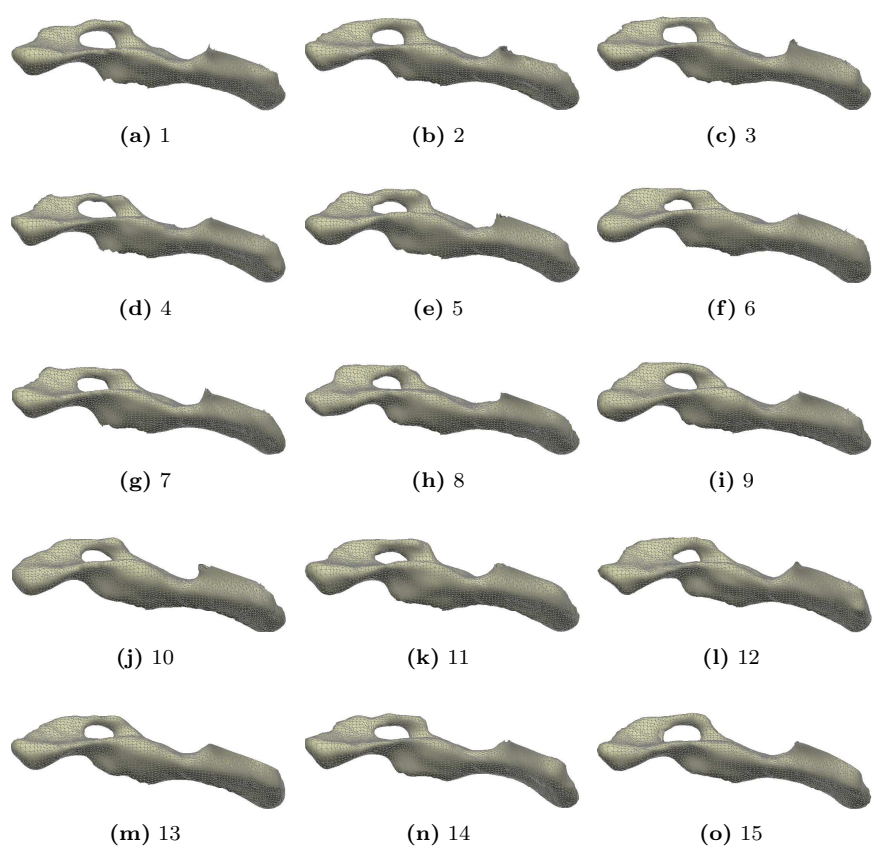


Figure 7.8: Surfaces 1-15

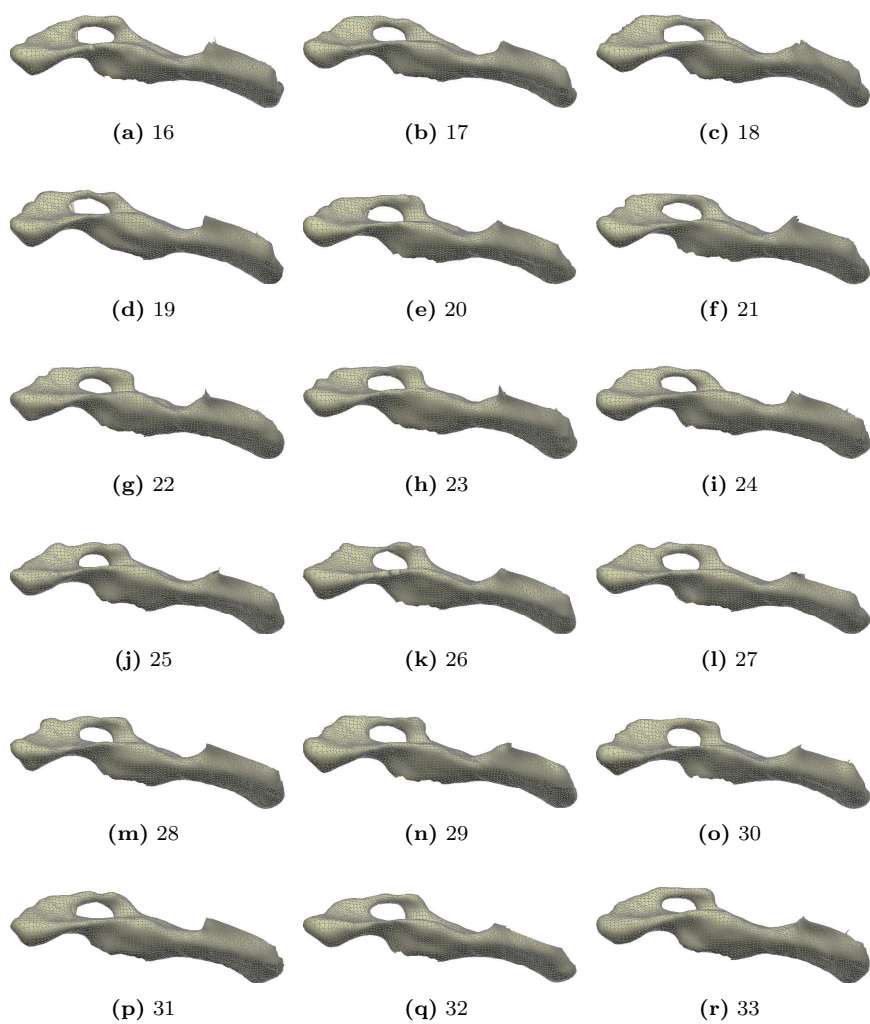


Figure 7.9: Surfaces 16-33

Comparison of Sparse Point Distribution Models

Søren G. H. Erbou, Martin Vester-Christensen, Rasmus Larsen, Lars B. Christensen, Bjarne K. Ersbøll

Abstract

This paper compares several methods for obtaining sparse and compact point distribution models suited for data sets containing many variables. These are evaluated on a database consisting of 3D surfaces of a section of the pelvic bone obtained from CT scans of 33 porcine carcasses. The superior model with respect to sparsity, reconstruction error and interpretability is found to be a varimax rotated model with a threshold applied to small loadings. The models describe the biological variation in the database and are used for developing robotic tools when automating labor-intensive procedures in abattoirs.

8.1 Introduction

Point distribution models (PDM), or statistical shape models, [37] are used to encapsulate, e.g. biological variation of shape in medical applications. They are typically used to obtain a deeper understanding of the variability of shapes in a population, e.g. corpus callosum, the heart, bones and joints, cf. [37] and [149]. Studies of normal versus abnormal/pathological cases are often of interest. The shapes are described by corresponding point coordinates and principal components analysis (PCA) can be applied to obtain a compact model description. Due to the nature of PCA, these models have a tendency to reveal modes of variation that are global since they are linear combinations of all of the point

coordinates. This makes the interpretation of each mode more difficult. In recent years, methods for obtaining more sparse modes of variation have been proposed, c.f. [118, 142, 150, 173]. These are sparse in the sense that the modes of variation are linear combinations of only a subset of point coordinates, i.e. revealing more spatially localized modes that are easier to interpret.

This paper compares a PCA-based PDM of 3D surfaces of porcine bone structures with four models that are more sparse. A quantitative comparison is performed by measuring the reconstruction error and the explained variance of the models.

In [25], Cadima and Jolliffe discuss the method of truncation of small loadings of the eigenvectors of the PCA, also known as threshold PCA (Th. PCA). It is emphasized that particular care should be taken in cases where the resulting loading vectors are far from orthogonal. Kaiser [93] proposed the varimax criteria (VM) for orthogonal factor rotation. It seeks to determine the rotation matrix \mathbf{R} maximizing the sum of the column-wise variances of the squared elements. The outcome of such a rotation is likely to reveal modes with more loadings close to 0 or ± 1 . This corresponds to a more localized model with modes that are easier to interpret. Stegmann *et al.* [150] apply the whole family of orthogonal rotation methods called Orthomax, of which the varimax method is a special case. They apply this on three 2D cases of shape and appearance models. The results show more localized modes than corresponding PCA modes and are recommended for data sets with a large number of variables, e.g. 3D surfaces. Zou *et al.* [173] propose a method called sparse PCA (SPCA). It is an iterative method for obtaining a more sparse model which is still close to the PCA solution. The sum of absolute and squared loadings constraints the solution.

Varimax and SPCA only make use of the second-order information given by the covariance matrix, assuming that the underlying signals of interest are Gaussian. If this is not the case, higher order methods such as independent component analysis (ICA) [85] would be more appropriate. ICA assumes non-Gaussian signals and maximizes statistical independence between the signals. Alcantara *et al.* [2] propose localized components analysis (LoCa), which is a variant where a measure of spatial locality is included in the cost function. This has been compared to SPCA and ICA on small data sets, with a similar performance but with more interpretable modes. ICA is reported to result in a reconstruction error significantly worse than that of SPCA and LoCa, because many more modes are needed to explain the same variation. The drawback of LoCa is that it is very costly to compute. Ólafsdóttir *et al.* [118] apply and compare PCA, ICA and SPCA for clustering two types of mice based on 3D craniofacial deformation fields and find that the more localized modes of ICA and SPCA result in better clustering features than the PCA. Non-linear methods such as

Kernel PCA have also been applied to shape modeling, cf. e.g. [131], but are found to be out of the scope of the present paper.

The loadings in PCA are orthogonal and the principal components, or scores, i.e. the data projected onto the loading vectors, are uncorrelated. Only the PCA solution can have both properties. In varimax rotation the loadings are orthogonal but the scores are correlated, and Th. PCA, SPCA and ICA have neither property. Zou *et al.* [173] propose to apply Gram-Schmidt orthogonalization to the scores matrix before computing the variance explained by each mode, in order to account for variance explained by several modes. Sjöstrand *et al.* [142] take this idea a step further and suggest ordering the modes according to this adjusted variance.

In the present work PCA and varimax rotation, along with their threshold counterparts and SPCA, are applied in PDMs of 3D bone surfaces. The specific data set is characterized by a large number of variables p (point coordinates) compared to the number of observations n , $p \gg n$. A comparison of these methods applied to dense PDMs and focusing on their reconstruction ability, has not previously been reported.

The models quantify the biological variation of specific bone structures and are intended for use when developing robotic tools by the Danish Meat Research Institute (DMRI) and for determining shape parameters for previously unseen surfaces for classification purposes.

8.2 Methods

The data consists of CT volumes of 33 porcine carcasses separated along the medial plane. Each scan has a slice thickness of 10mm with a spacing of 10mm between each slice. Voxel dimensions are $[x, y, z] = [0.88, 0.88, 10]$ mm. Approximately 30 slices per carcass are used in this application, covering the region around the pelvic bone.

In order to build a PDM as described in [37] corresponding points/landmarks are required. For surfaces in 3D, automated methods for defining points and determining point correspondence are necessary. The method applied here consists of several preprocessing steps. First a 2D segmentation of bone contours from CT scans is performed using a simple threshold and mathematical morphology is applied for noise reduction. Next a 3D implicit surface is estimated from 2D contours using variational interpolation and Radial Basis Functions [162]. The implicit surface is re-sampled to an isotropic resolution and the "Marching Cubes" algorithm [103] is applied for obtaining a triangle-based surface repre-

sentation. Lastly point correspondence between surfaces is obtained using the ICP algorithm [15] with an additional step where a method similar to ray-racing is applied, cf. [137]. The corresponding point is restricted to being on a line along the mean curvature normal of each point/triangle vertex, at the location where it coincides with the surface, as long as the point-to-surface distance is within some limit. Otherwise the closest point on the surface is chosen. This might introduce minor discontinuities but these are not considered to be an issue in the current data set and application.

Initially a specific shape is chosen as a reference and registered to all other shapes. In order to reduce the bias towards the specific reference shape, the mean shape of the initial registration is computed and then registered to all shapes. This procedure is done several times in order to reduce the bias towards the choice of initial reference shape. It is now possible to do statistical analysis on the distribution of the points, and to construct a compact model describing the shape variation. To account for translational, rotational and scaling effects, a Generalized Procrustes Analysis is performed, cf. [47] and [72]. The procedure iteratively estimates the mean of the shapes and minimizes the Euclidean distance between the mean and each shape, using translation, rotation and scaling of the shapes. This ensures that the remaining variation is due to biological variation only.

8.2.1 Point distribution model

PDMs were proposed by Cootes *et al.* as a compact way of describing shape variation in a data set [37]. Let the n shapes, or in this case 3D surfaces, be represented by k corresponding 3D points, each arranged in a p -dimensional vector \mathbf{s} ($p = 3k$). The idea is to formulate a parameterized model of the form $\mathbf{s} = M(\mathbf{g})$ describing the variation seen in the data, where \mathbf{g} is a vector of shape parameters of the model M . The sample mean ($\bar{\mathbf{s}} = 1/n \sum_{i=1}^n \mathbf{s}_i$) and sample covariance matrix ($\mathbf{C} = 1/(n-1) \sum_{i=1}^n (\mathbf{s}_i - \bar{\mathbf{s}})(\mathbf{s}_i - \bar{\mathbf{s}})^T$) are then computed. Since the original parameter space is usually much larger than the number of observations ($p \gg n$), applying PCA on the covariance matrix is an obvious choice for dimensionality reduction. The PCA determines the main axes (eigenvectors ϕ_i) of variation of the data and sorts them according to the amount of variation they describe (eigenvalues λ_i). The model, or principal components (PC), can then be formulated as a perturbation of the mean shape:

$$\mathbf{s} = \bar{\mathbf{s}} + \Phi \mathbf{g}, \quad (8.1)$$

where Φ is the matrix composed of the eigenvectors ϕ_i . The coefficients of this matrix are also known as the loadings. The model parameters of a new aligned

shape s' can be obtained by projecting it into the parameter space,

$$\mathbf{g}' = \Phi^T(\mathbf{s}' - \bar{\mathbf{s}}). \quad (8.2)$$

An important point to make when interpreting PDMs is that they are purely data-driven. They only show the variability expressed in the data from which they are built. Using such models for prediction should therefore be done with care, considering how well the data represent the population one is trying to predict features from.

8.2.2 Model selection

Only the first t eigenvectors of Φ are used in eqs. 8.1 and 8.2, assuming that subsequent eigenvectors only contain noise. Often not much attention is focused on model selection after applying the PCA, or on methods to improve interpretation of the modes. Model selection, i.e. how to determine the number of principal components to retain, can be done in a number of ways. Jackson [87] and Hayton *et al.* [77] provide excellent overviews of many of these methods.

Traditionally a certain level of noise is assumed in the data, e.g. 5% noise, in which case t is chosen so that the sum of the first t eigenvalues only just exceeds 95% of the total variation. If no prior knowledge is at hand, this method is not recommended. Another widely used method is a graphical technique called the scree test, where the eigenvalues are plotted in descending order and only the modes above the "elbow" of the plot are kept. The problem with this method is that the "elbow" is not always well defined. The method used here is named parallel analysis (PA) and was originally proposed by Horn [83]. In PA each variable is randomized across observations a number of times (e.g. 100 times). Each time, a new PCA is computed and the eigenvalues are plotted in a scree plot alongside the eigenvalues of the PCA of the original data. Only the modes of the original data with values above the corresponding values of the randomized data should be kept. The eigenvalues of the randomized data give an estimate of the amount of variation that cannot be explained by chance alone. A conservative, but widely used, estimate is obtained by using this level for model selection and only keeping modes of the original data with eigenvalues that are larger than the level.

8.2.3 Comparing models

The PDMs are compared with respect to reconstruction error, sparsity and interpretability. The mean and standard deviation (std.) of the root-mean-

squared (rms) reconstruction error are reported in millimeters (mm). These are a measure of the model's ability to describe an unknown surface. The sparsity level of a model is given by the percentage of non-zero loadings in each mode. The more loadings that are zero, the more sparse the mode is and the more localized the variation it describes will be. Interpretability and sparsity are closely related in the sense that the interpretation of a specific mode of variation is easier and more intuitive if the variation described is spatially localized, which sparse modes tend to be. In the standard PCA-based model, this is often not the case for the first couple of modes. More sparse models are therefore preferred if they fulfill other requirements for the model, e.g. a certain level of the reconstruction error and explained variance. The explained variance of a model is important if the aim is to cover the variation described by the data from which the model is made. In this paper the term "adjusted variance" is used, cf. sect. 8.2.6, which only takes into account variation that is not explained by previous modes.

Comparing models is finding the best trade-off between obtaining a reasonable amount of the total adjusted variance explained, minimizing the amount of non-zero loadings to improve interpretability, while controlling the reconstruction error. As an example it might be reasonable to accept a smaller adjusted variance explained if the reconstruction error is not affected and the model is more sparse, since the modes of variation will probably be easier to interpret.

8.2.4 Varimax rotation

Kaiser [93] proposed the varimax criteria (VM) for orthogonal factor rotation. It estimates a rotation matrix \mathbf{R} which, when applied to the matrix of the first t eigenvectors $\mathbf{\Phi}_t$, maximizes the sum of the column-wise variances of the squared loadings. The outcome of such a rotation is likely, but not certain, to reveal modes with more loadings close to 0 or ± 1 which tend to be more sparse and localized. The incentive is that more sparse and localized modes are easier to interpret. Rotating the eigenvectors results in correlated scores. If each element in the $p \times t$ matrix $\mathbf{\Phi}_t$ is denoted ϕ_{ij} , the value of the varimax criterion can be formulated as

$$V(\mathbf{\Phi}_t) = \sum_{j=1}^t \left(\frac{1}{p} \sum_{i=1}^p \phi_{ij}^4 - \left(\frac{1}{p} \sum_{i=1}^p \phi_{ij}^2 \right)^2 \right). \quad (8.3)$$

The varimax rotation (VM) results in more sparse modes of variation and the ordering of VM modes is traditionally set according to the measure of sparsity of eq. 8.3. The ordering is therefore different to that of a PCA-based model, where the ordering is done according to the eigenvalues, i.e. the explained variance.

The effect of this is that the variation explained by each VM mode is not ensured to be monotonically decreasing for increasing modes. In this work, ordering is done according to the adjusted variance explained by each mode, cf. sect. 8.2.6.

8.2.5 Sparse PCA (SPCA)

SPCA was proposed by Zou *et al.* [173] and is formulated as a regression problem approximating the properties of a PCA, but with sparse modes. The following SPCA criterion is minimized

$$\begin{aligned} (\hat{\mathbf{A}}, \hat{\mathbf{B}}) = & \arg \min_{\mathbf{A}, \mathbf{B}} \sum_{i=1}^n \|\mathbf{x}_i - \mathbf{A}\mathbf{B}^T \mathbf{x}_i\|^2 + \\ & \lambda \sum_{j=1}^t \|\mathbf{b}_j\|^2 + \sum_{j=1}^t \delta_j \|\mathbf{b}_j\|_1, \end{aligned} \quad (8.4)$$

s.t. $\mathbf{A}^T \mathbf{A} = \mathbf{I}.$

\mathbf{x}_i is the i th column of the $p \times n$ matrix \mathbf{X} containing the parameters of the n surfaces. \mathbf{B} contains the t loading vectors (\mathbf{b}_j), and \mathbf{A} projects the scores back into the original space of \mathbf{X} . The first term thereby measures the reconstruction error, while the constraint on \mathbf{A} ensures a solution where \mathbf{B} is close to orthogonal. The remaining terms ensure a unique solution for cases where $p > n$, while driving \mathbf{B} towards a sparse solution. Zou *et al.* [173] propose an iterative algorithm for solving eq. 8.4 with respect to \mathbf{B} . It is also shown that if $p \gg n$, then letting $\lambda \rightarrow \infty$, so-called soft thresholding can be used to estimate \mathbf{B}

$$\mathbf{b}_j = (|\mathbf{a}_j^T \mathbf{X} \mathbf{X}^T| - \frac{\delta_j}{2})_+ \text{Sign}(\mathbf{a}_j^T \mathbf{X} \mathbf{X}^T). \quad (8.5)$$

\mathbf{a}_j is the j th column of \mathbf{A} and $(\cdot)_+$ denotes $\max(0, \cdot)$. δ_j sets the weight given to the sparsity term and can be set individually for each mode if desired. Equation 8.4 is solved iteratively by fixing \mathbf{A} , solving for \mathbf{B} and then recalculating \mathbf{A} . The number of loading vectors t should be set beforehand, and is often set according to the PCA solution. Often a specific sparsity level, in terms of the number of non-zero loadings, is used as stopping criteria for the algorithm, and this is achieved by dynamically changing δ_j for each iteration. The Matlab implementation used was supplied by Sjöstrand *et al.* [142] who apply SPCA to a number of PDM applications. In [118] Ólafsdóttir *et al.* apply soft thresholding SPCA in order to build a statistical deformation model of mice skulls from micro CT scans. The model is used for discrimination purposes, and does not focus on the reconstruction error.

8.2.6 Adjusted Variance

No other linear combination of the original data than the PCA results in both orthogonal loading vectors and uncorrelated principal components or scores.

One or both properties are sacrificed when applying other loading vectors. Zou *et al.* [173] therefore propose a method to compute the adjusted variance of each mode. This is simply done by factoring out the variation explained by previous modes of the model before computing the variance explained by the current mode. This is also known as Gram-Schmidt orthogonalization. Sjöstrand *et al.* [142] propose ordering the modes according to the adjusted variance, an approach adopted for all the methods compared in this work, apart from the PCA. The notation is adopted from [142]. Denote the scores matrix of any method \mathbf{Z} , where the columns have been sorted according to decreasing order. The adjustment of \mathbf{z}_j for all higher order components can be done by applying

$$\hat{\mathbf{z}}_j = \mathbf{z}_j - \mathbf{Z}_{(j-1)}(\mathbf{Z}_{(j-1)}^T \mathbf{Z}_{(j-1)})^{-1} \mathbf{Z}_{(j-1)}^T \mathbf{z}_j, \quad (8.6)$$

where $\mathbf{Z}_j = [\mathbf{z}_1, \dots, \mathbf{z}_j]$. The adjusted variance of the j th mode can then be estimated as the variance of $\hat{\mathbf{z}}_j$.

8.2.7 Sparse loadings by threshold

Thresholding PCA loadings of small absolute value is often used for comparison with more elaborate ways of obtaining sparse loadings. Cadime and Jolliffe [25] discuss the pitfalls that should be avoided using this method. Applying too high a threshold might reveal loading vectors that are far from orthogonal. In order to account for the variation lost by truncating some loadings, each loading vector should be normalized to unit length afterwards.

Threshold PCA is applied in this work for comparison with the SPCA. The actual sparsity level is chosen in such a way that it results in the same number of non-zero loadings as the corresponding SPCA model that it is compared to. Furthermore the effect of applying a threshold to the varimax-rotated loading vectors is investigated. Due to the more uniform variance spectrum of the varimax modes, compared to that of the PCA, it makes more sense to apply the same sparsity level for each varimax mode than it does for each PCA mode.

8.3 Results and discussion

For registration with the ICP algorithm, the similarity transformation is applied (translation, rotation and scaling), since speed is an issue in a future online application. The ICP is done sequentially with three different capture ranges, [20, 10, 5]mm, for each surface registered to the mean surface. This reduces the large effect of possible outliers on the cost function and makes the registration more robust to initialization. The triangulation from the initial shape is kept,

so that only the vertex positions are changed. Each of the $n=33$ shapes now consists of $k=3,815$ points in 3D, i.e. $p=11,445$ variables.

Five models are compared with respect to reconstruction error, the standard PCA model, VM with orthogonal rotated loading vectors, the SPCA, and threshold versions of the PCA (Th. PCA) and varimax (Th. VM). The best model is regarded as that which results in the best trade-off between sparsity, reconstruction error and interpretability.

The reconstruction error is defined as the mean rms error of all the shapes in a leave-one-out (LOO) validation scheme. The rms error for a specific case is computed as the rms value of the point-to-point distances less than 5mm, only taking into account distances where the closest point does not belong to the edge of the surface. This makes the error measure more robust to outliers and parts missing or non-corresponding. In the LOO scheme one surface is left out and each model is built from the all-but-one surfaces. The surface left out is then registered to the models and the rms error is computed. The model parameters are estimated sequentially using line search, since this revealed a lower rms error for the PCA-based models than by using the projected parameters (cf. eq. 8.2), when only using the first t modes.

8.3.1 Explained Variance

In each PCA model of the LOO scheme, PA is performed to set the number of modes t to retain. In 21 out of the 33 cases, PA found that t should be 8, and in the last 12 cases either 7 or 9. On this basis t is set to 8 modes of variation for all models. For each of the three sparse models the number of non-zero loadings is varied from 5 to 95% in order to investigate the effect on the reconstruction error and the variance explained. The same level of sparsity is applied to all modes. This favors models with a more uniform variance spectrum such as the VM rotated models, since the same amount of loadings is zero. All the models are sorted according to the adjusted variance explained.

Figure 8.1 (left) shows the total adjusted variance spectrum of the five models, each with eight modes included, as a function of the amount of non-zero loadings for the three sparse models. Figure 8.1 (right) shows the adjusted variance explained by each mode for the five models, with the number of non-zero loadings set to 30%. Both figures are from a specific LOO model. The right figure shows the more uniform variance spectrum of the VM/Th. VM models. The left figure shows that the Th. VM model converges to its maximum explained variance before the Th. PCA. This supports the assumption that the threshold VM is better suited for a fixed sparsity level for all modes than the Th. PCA.

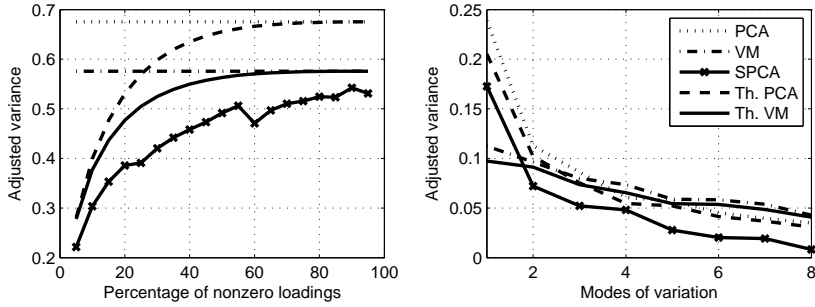


Figure 8.1: For a specific LOO model, the total adjusted variance explained is plotted (left) as a function of the percentage of non-zero loadings, with eight modes included in all five models. In the right figure the adjusted variance explained by each mode is plotted for a sparsity level of 30% non-zero loadings for the three sparse models.

Model	Var. expl. [%]	Rms error [mm] mean (std.)
PCA	67.5	1.564 (0.123)
VM	57.6	1.570 (0.125)
Th. PCA	59.8	1.580 (0.124)
Th. VM	52.5	1.578 (0.121)
SPCA	42.0	1.630 (0.137)

Table 8.1: For a specific LOO model, the total adjusted variance explained is shown for each of the five models, along with the mean and std. of the rms error for all LOO models. Eight modes of variation are included and a sparsity of 30% non-zero loadings is chosen for the three sparse models.

Table 8.1 shows the total adjusted variance explained by the models, including eight modes for a specific LOO model, and also the mean and std. of the rms reconstruction error over all LOO models. Th. VM has a similar mean rms error, while explaining less of the total adjusted variance, which indicates that it is slightly superior to Th. PCA when using fixed sparsity levels for all modes. The std. of the rms error of the five models is rather large compared to the difference in their mean value. A comparison of the adjusted variance explained for the five models with eight modes and 30% non-zero loadings is done by performing paired t tests. The H_0 hypothesis is that there is no significant difference in the adjusted variance explained. Table 8.2 shows that this hypothesis is rejected at a 0.1% confidence level, meaning that the adjusted variance explained is significantly different for all combinations of models. This seems reasonable when comparing the five models at 30% non-zero loadings for a specific LOO-model in figure 8.1.

Model	VM	Th. PCA	Th. VM	SPCA
PCA	1	1	1	1
VM		1	1	1
Th. PCA			1	1
Th. VM				1

Table 8.2: Paired t test of the difference in adjusted variance explained being zero (H_0) at a 0.1% significance level. 1 denotes H_0 -reject, i.e. the adjusted variance explained is significantly different for each pair of models. A sparsity level of 30% non-zero loadings is chosen for the three sparse models.

The SPCA explains the least variation by far, which might indicate a more sparse model. The adjusted variance explained by the higher order modes of the SPCA is significantly less than for the other models. This would be a nice result if the reconstruction error was comparable to that of the PCA model. It turns out that the reconstruction error for the SPCA is much higher than for all the other models. Taking a closer look at the correlations of the SPCA loading vectors, it turns out that many of them are highly correlated, i.e. far from orthogonal, which means that the scores become extremely correlated. The adjusted variance takes this into account, making the total adjusted variance explained much less than for the other models. The SPCA should reveal a near-orthogonal solution due to the constraint on \mathbf{A} in eq. 8.4, therefore the solution given does not seem to converge properly on the given data set with the given number of modes. Reducing the number of modes until a near-orthogonal solution is reached is an option, but then much less of the original variation would be explained by the model, for which reason the SPCA solution is not pursued further. Since no previous work reports the reconstruction error from a SPCA PDM model on 3D surfaces with large p , it cannot be concluded that the SPCA in general has convergence issues for such data sets, or if it is just a coincidence that it does not converge on the data set in the present application. For discrimination purposes, it is reported to reveal good results on large p data sets [118].

8.3.2 Sparsity

Figure 8.2 shows the mean and std. of the rms errors for each model as a function of sparsity, when including one and eight modes respectively. When including only the first mode of variation, the SPCA converges to the same error level as the PCA. Comparing that to the eight-mode SPCA is another indication of a solution that does not converge, i.e. has far from orthogonal loading vectors. In both cases the Th. VM converges to the VM solution at a sparser level than the Th. PCA does to the PCA solution. This is another indication of the Th. VM

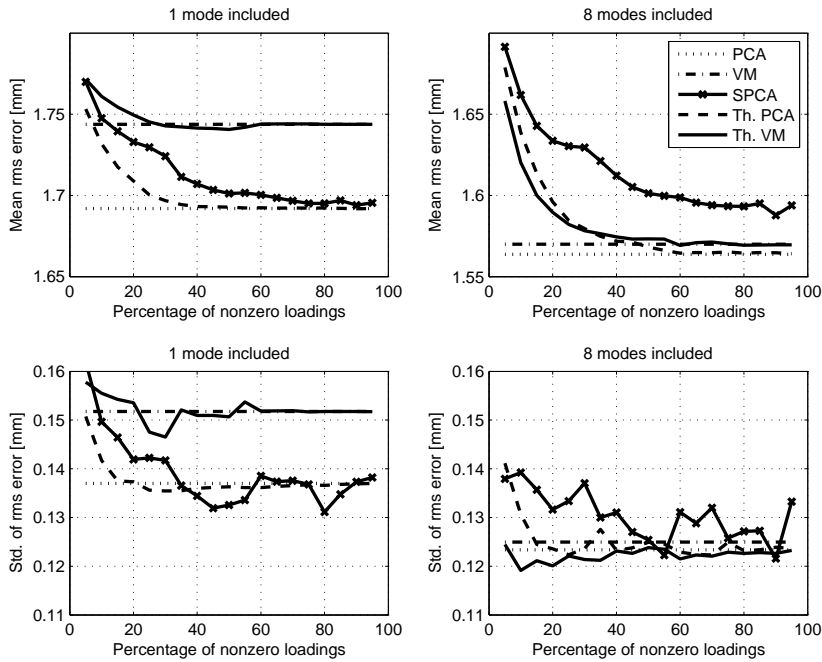


Figure 8.2: Reconstruction error. The top row shows the mean rms error as a function of the percentage of non-zero loadings (note the scaling of the axes). The bottom row shows std. of the rms error. The left column shows the results with only one mode included and the right column shows results with eight modes included.

being slightly superior to the Th. PCA for a fixed sparsity level on all modes. For both threshold methods the loading vectors are near-orthogonal. The std. of the rms error is higher for the VM-based models than for the PCA based models when including only one mode, but when including all eight modes, the std. is similar for a large number of non-zero loadings, while the Th. VM performs better than the Th. PCA when the number of non-zero loadings is below 20%.

In figures 8.3,8.4,8.5,8.6 and 8.7 the modes of the five shape models are compared. Left and right columns for each model are perturbed $-3/+3$ std., respectively, from the mean shape. Rows are modes 1-8, cf. figure 8.1. The color coding shows the distance to the mean surface, from blue through red ($> 0 \rightarrow 3$ mm). Zero distance is denoted gray in order to emphasize sparse regions and the localized nature of the modes in the sparse models. Gray regions of each mode are not affected by the corresponding mode, which makes the interpretation more simple. A sparsity level of 30% non-zero loadings is chosen for the three sparse models, based on the variance explained and reconstruction error of figures 8.1 and 8.2. For sparsity levels less than 30% non-zero loadings the Th. VM still outperforms the Th. PCA, although the reduction in explained variance severely affects the reconstruction error negatively.

PCA1 varies quite globally as expected from figure 8.1. It seems that the variation of PCA1 is to some extent the variation also expressed by VM1 and VM7. Furthermore the common variation of modes PCA2 and PCA3 seems to be concentrated in one VM mode, VM2. In general there is a tendency towards areas of variation in the higher order PCA modes becoming more yellow/red in the VM modes, e.g. PCA6 compared to VM7. This corresponds to the VM modes describing more variation in the same areas, i.e. localizing the variation.

Of course the threshold versions of PCA and VM in general show the same patterns as their non-sparse counterparts, and the same conclusions can be drawn from these models. The benefit of choosing the sparse versions is of course a more compact model, 1/3 the size, at the expense of a very little increase in the mean rms reconstruction error. The reduction in variance explained by the sparse models compared to the full models is therefore likely to mainly consist of noise. The SPCA seems to do a reasonable job of estimating the first few modes, e.g. SPCA2 compared to Th. VM2, but the higher order modes show much of the same variation, which was also noted when looking at the correlation of the loading vectors.

8.3.3 Error distribution

Figure 8.8(a) shows the distribution of the reconstruction error of the PCA model projected onto the mean surface. Colors show the LOO rms error of

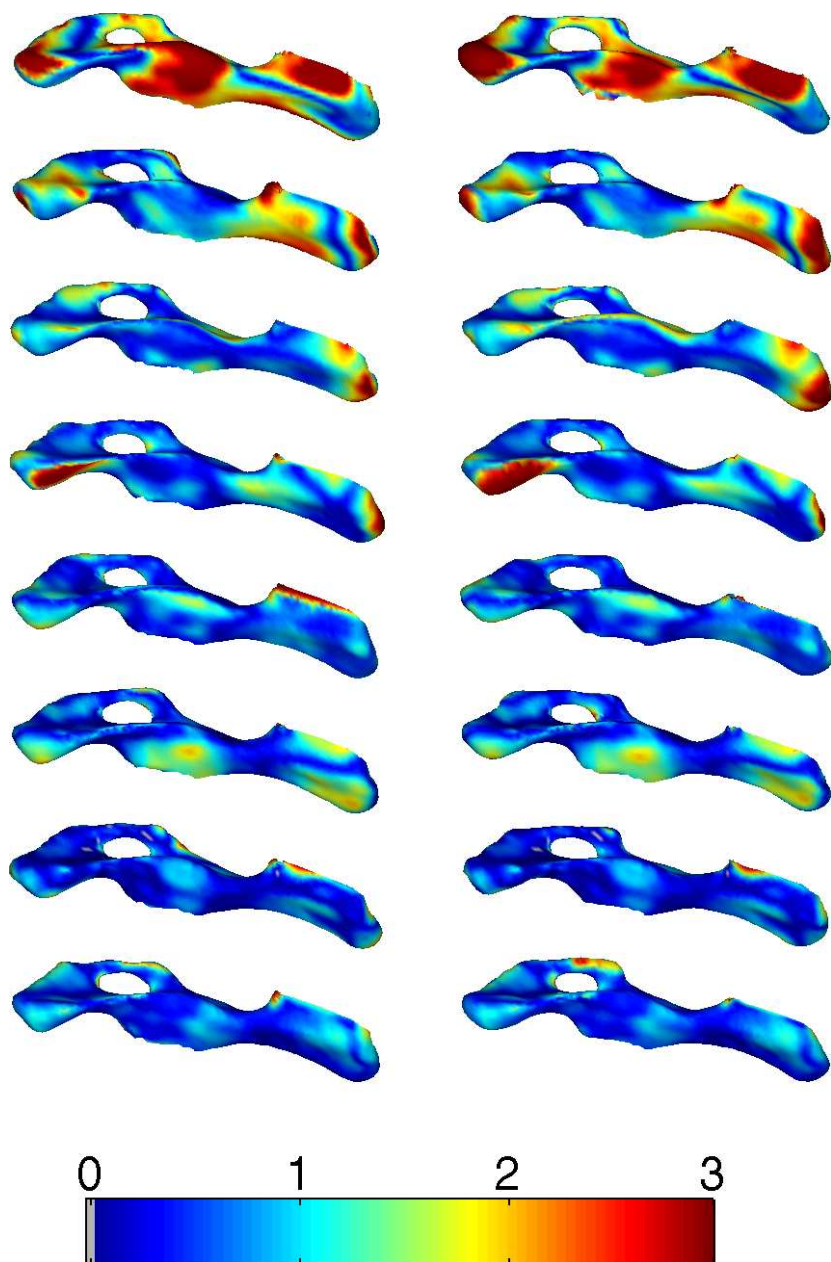


Figure 8.3: PCA model. Left and right column is perturbed $-3/+3$ std., respectively, from the mean shape. Rows are modes 1-8, cf. figure 8.1. The color coding shows the distance to the mean surface, from blue through red ($> 0 \rightarrow 3\text{mm}$). Zero distance is denoted gray.

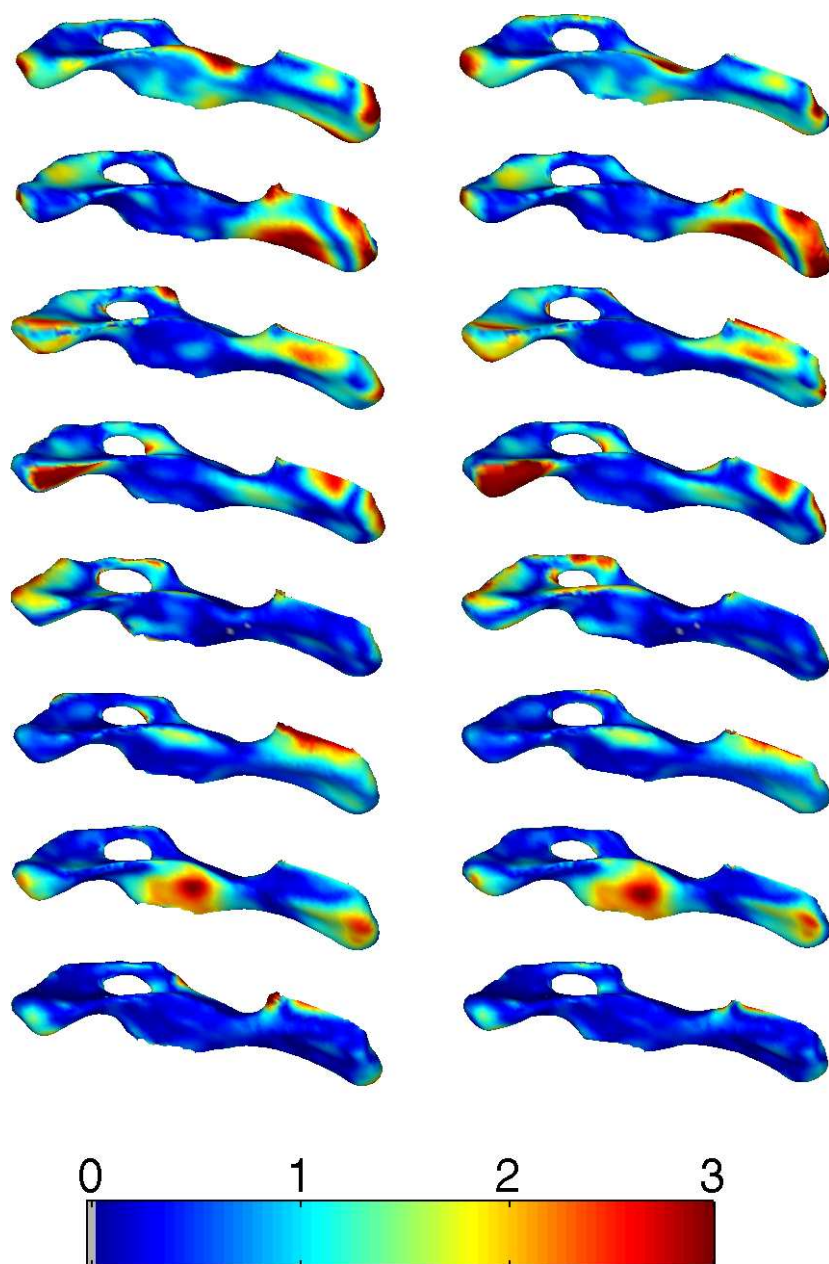


Figure 8.4: Varimax model. Left and right column is perturbed $-3/+3$ std., respectively, from the mean shape. Rows are modes 1-8, cf. figure 8.1. The color coding shows the distance to the mean surface, from blue through red ($> 0 \rightarrow 3\text{mm}$). Zero distance is denoted gray.

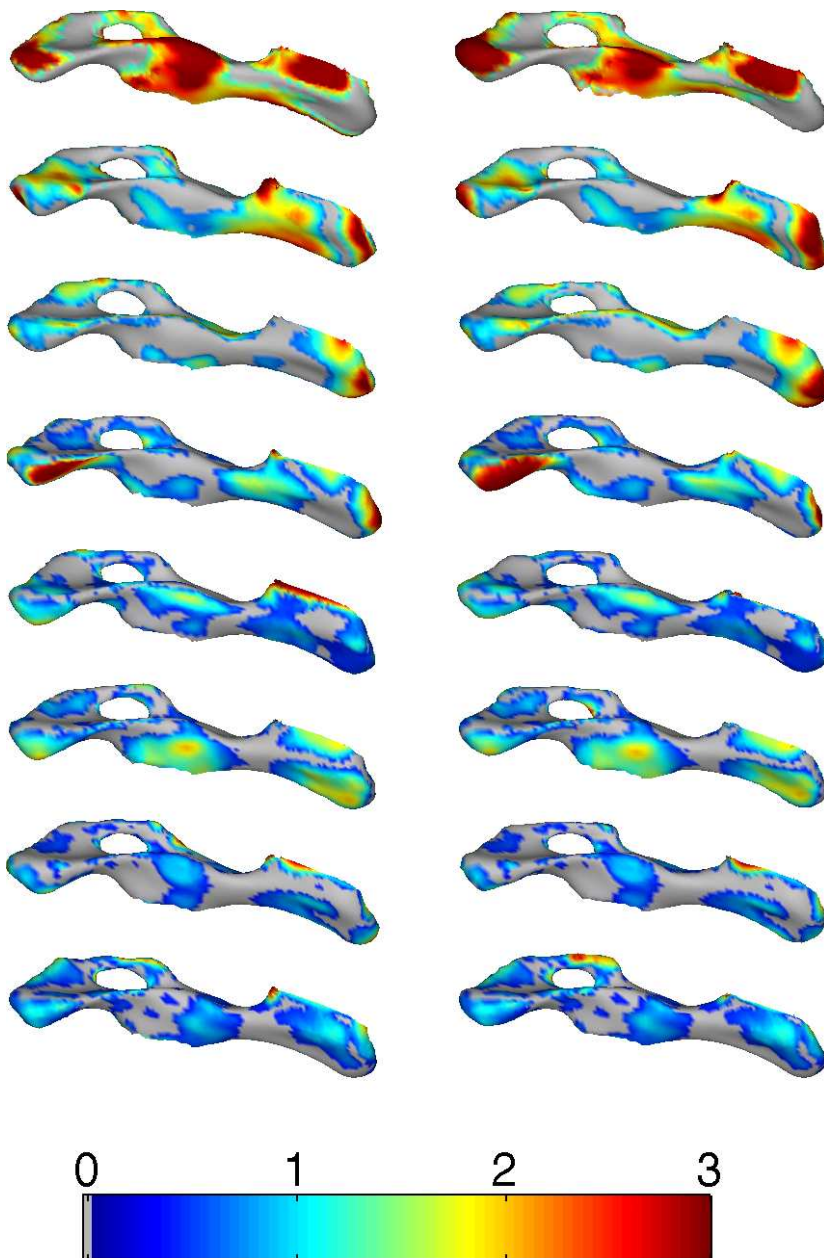


Figure 8.5: Threshold PCA model. Left and right columns for each model are perturbed $-3/+3$ std., respectively, from the mean shape. Rows are modes 1-8, cf. figure 8.1. The color coding shows the distance to the mean surface, from blue through red ($> 0 \rightarrow 3\text{mm}$). Zero distance is denoted gray.

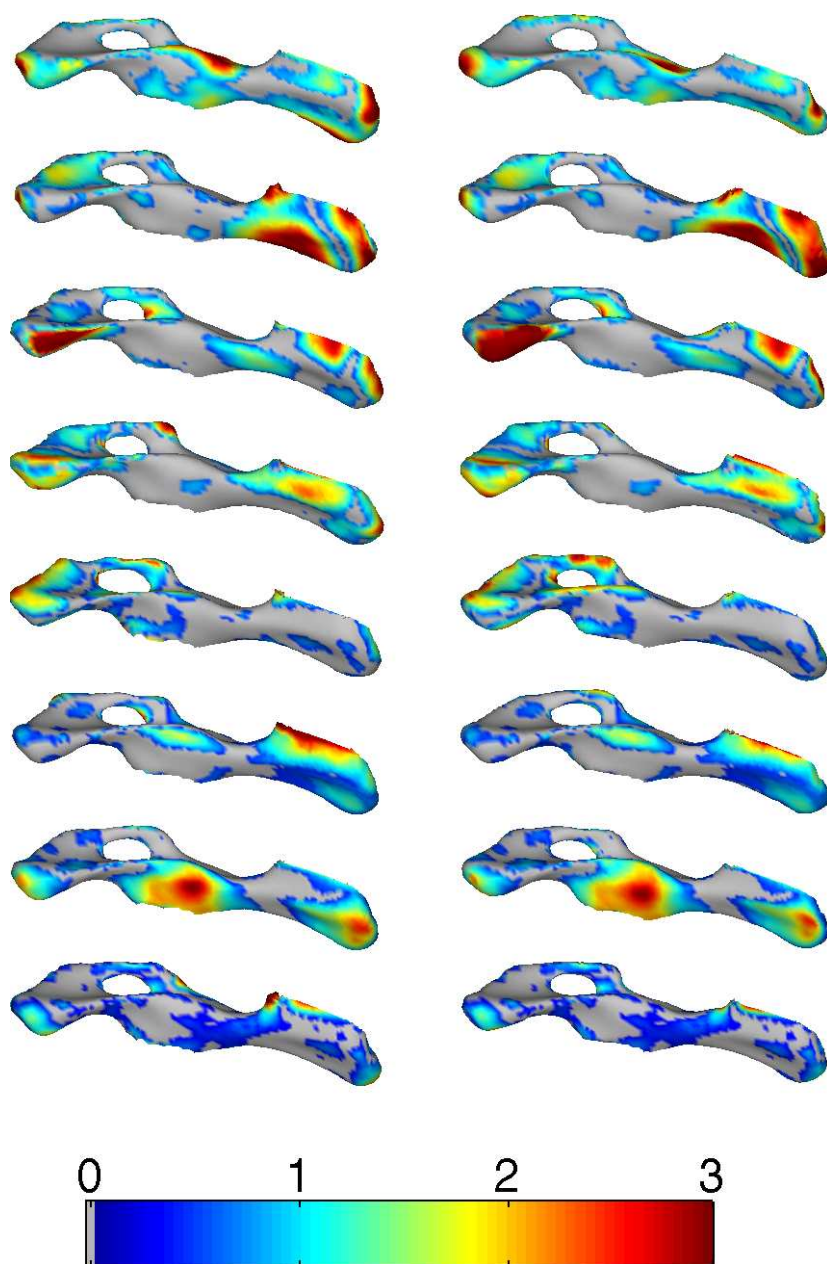


Figure 8.6: Threshold Varimax model. Left and right columns for each model are perturbed $-3/+3$ std., respectively, from the mean shape. Rows are modes 1-8, cf. figure 8.1. The color coding shows the distance to the mean surface, from blue through red ($> 0 \rightarrow 3\text{mm}$). Zero distance is denoted gray. A sparsity level of 30% non-zero loadings is chosen.

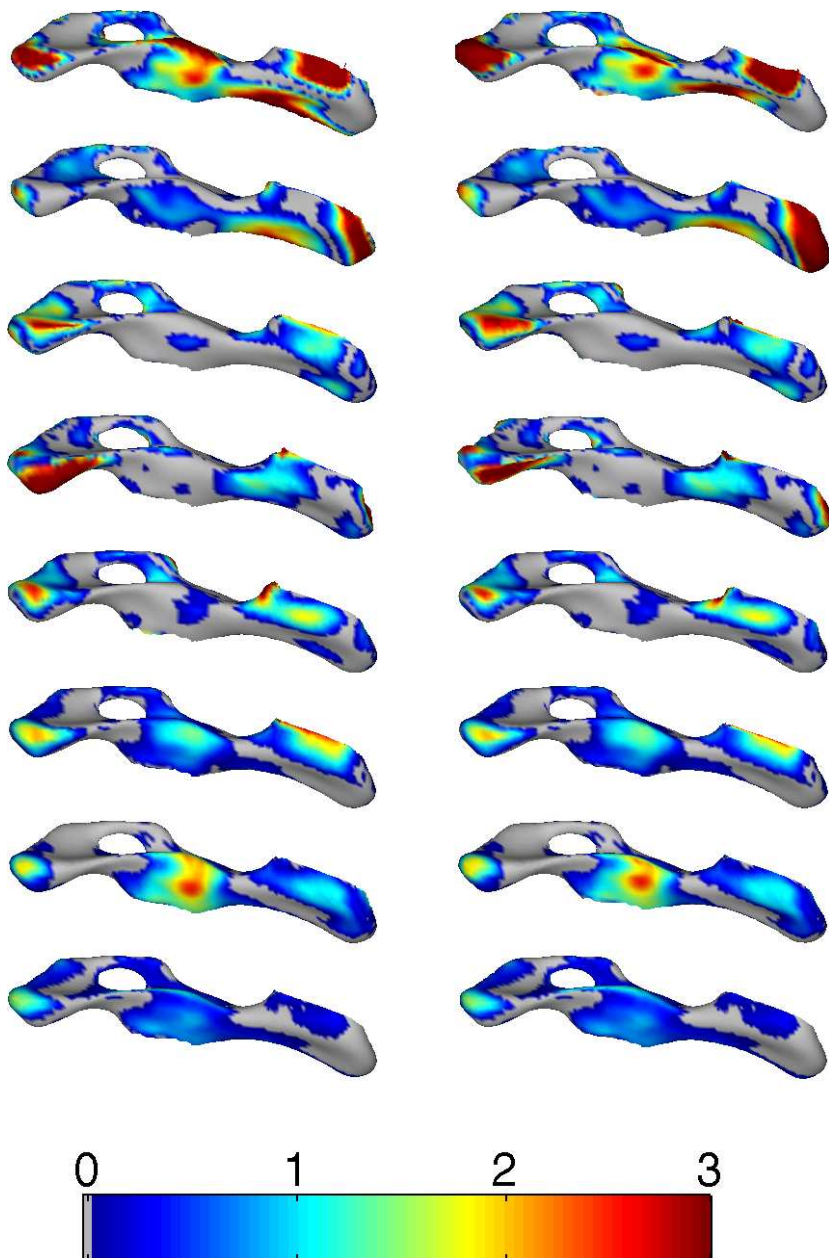


Figure 8.7: SPCA model. Left and right columns for each model are perturbed $-3/+3$ std., respectively, from the mean shape. Rows are modes 1-8, cf. figure 8.1. The color coding shows the distance to the mean surface, from blue through red ($> 0 \rightarrow 3\text{mm}$). Zero distance is denoted gray. A sparsity level of 30% non-zero loadings is chosen.

Model	VM	Th. PCA	Th. VM	SPCA
PCA	1	1	1	1
VM		0	0	1
Th. PCA			0	1
Th. VM				1

Table 8.3: Paired t test of the mean difference in spatial rms error being zero (H_0) at a 0.1% significance level. 1 denotes H_0 -reject, i.e. the difference in rms error is different from zero, with the model in the row having smaller spatial rms error than the model in the column.

each point on the surface. Areas with high curvature or near edges have higher rms errors than more central parts with low curvature. Figure 8.8(b) shows the distribution of the mean spatial rms error of the PCA model subtracted from the errors of each of the four other models, VM / Th. PCA / Th. VM / SPCA from the top down. Areas of bluish show better performance than the PCA model and areas of reddish perform worse. The SPCA model clearly performs quite badly as previously indicated. The three other models perform similarly with a slight improvement in the central part, and larger errors at the ends.

A number of paired t tests are performed, comparing the five methods pairwise. The rms error at each surface point is paired for two methods and the null hypothesis (H_0) is that the difference in rms error belongs to a normal distribution with zero mean, i.e. that there is no significant difference between the two methods. Since the number of samples is large the central limit theorem applies for the normal assumption. A significance level of 0.1% is applied. Table 8.3 shows the result of these tests. Zero denotes H_0 -accept and 1 denotes H_0 -reject, the latter indicating the method in the row having the smaller mean rms error. The Th. PCA model has a significantly lower spatial rms error than all the other models, which was expected. The SPCA performs worse than all the other models. For the chosen levels of sparsity there is no significant difference between the VM/Th., PCA/Th. and VM models. In other words any of these three models will reveal similar spatial rms errors. The favored model would therefore be the Th. VM, since it has more interpretable modes than the Th. PCA and is more sparse than the VM model. It explains the least amount of variance of the three models, but having the same error level it must have a better signal-to-noise ratio.

8.3.4 Discussion

PCA-based PDMs have been applied in numerous biological and medical applications for modeling shape. The need for more localized and easier interpretable

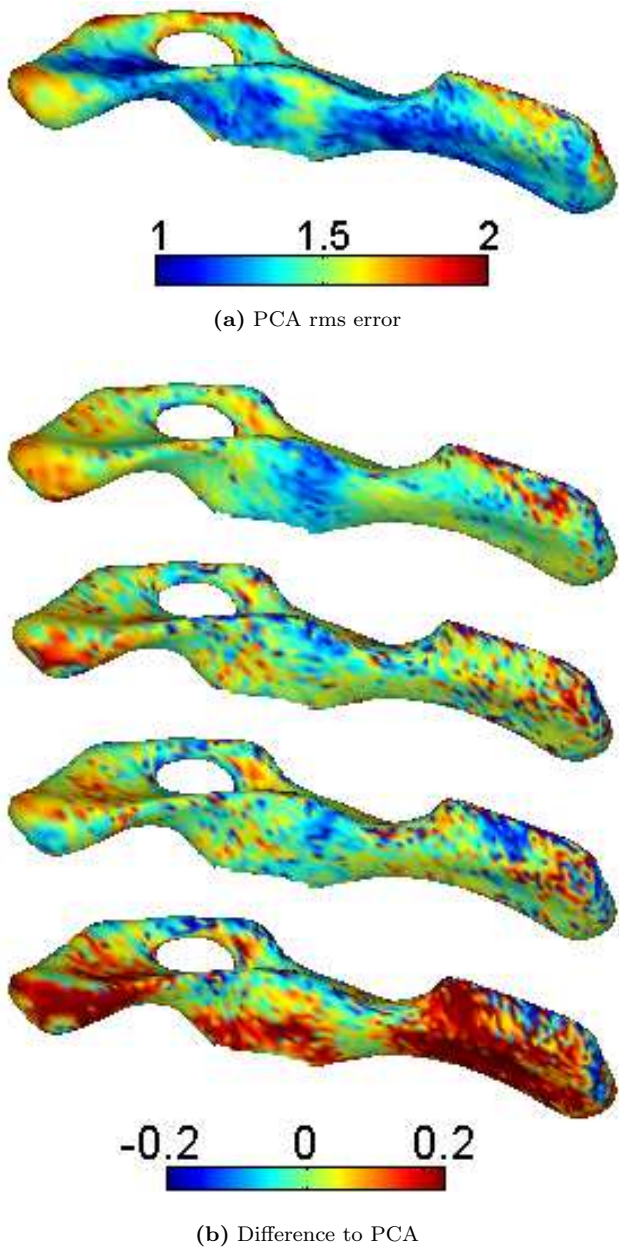


Figure 8.8: Spatial error distribution [mm]. (a) rms error distribution using PCA model. (b) difference in rms error distribution between, from the top down, VM / Th. PCA / Th. VM / SPCA and PCA respectively. Negative differences (bluish) denote smaller rms errors, and positive differences (reddish) denote larger rms errors, than the PCA model.

modes of variation has driven research in the direction of sparse models. In medical applications it is often of interest to be able to model pathologies that are spatially localized. Sparse models, such as the ones applied in this paper, are appropriate for shapes with a large number of variables, e.g. 3D surfaces. Ólafsdóttir *et al.* [118] report the SPCA as superior to other sparse models when applied to 3D deformation fields and evaluated for discrimination purposes.

Results of the present paper, where focus is on the reconstruction error and the explained variance, show that the SPCA is not the best sparse model for this specific application of modeling dense 3D surfaces of bones. The SPCA algorithm does not seem to converge properly, which may be a consequence of the specific application. Instead the proposed threshold varimax model outperforms both the varimax model and the threshold PCA model, making it the preferred sparse model for the application. Sparse models are not only appropriate for applications where interpretation of localized structures is of interest, but also for applications where speed and memory are issues due to the nature of the models.

8.4 Conclusion

This paper presents a comparison of four sparse point distribution models (PDMs) with one based on principal components analysis (PCA). The four models are orthogonal rotation by VM, thresholds of small absolute valued loadings of both PCA and VM, and finally the sparse SPCA method proposed by Zou *et al.* [173].

Eight modes of variation are included, based on parallel analysis, and a fixed level of sparsity is used for all eight modes. The standard PCA model has the smallest reconstruction error, but also contains more global modes of variation which are more difficult to interpret. The Varimax model explains less variation, has more interpretable modes and a slightly larger reconstruction error. For the three sparse models, a sparsity level of 30% non-zero loadings was applied. The SPCA model with eight modes is found not to converge to a suitable solution on the present data set. This results in a very poor reconstruction error compared to the other models. Applying a threshold to the PCA model results in a reconstruction error slightly larger than the full PCA model, but at the same level as the VM and Th. VM models. The Th. VM is considered superior to the Th. PCA since it has a similar performance, but with less total variation explained by the model. This is caused by the choice of a common sparsity level for all modes, considering the more uniform distribution of the explained variance of the VM-based models. The interpretation also seems to reveal slightly more localized modes, especially those of higher order, i.e. 5-8. On the basis of this the Th. VM seems better at capturing the important variation. Reducing the

sparsity level to less than 30% non-zero loadings results in a substantial reduction in the explained variance of the sparse models, which severely affects the reconstruction error. Still the Th. VM outperforms the Th. PCA model.

The Danish Meat Research Institute is focused on using easily interpretable PDMs such as these in developing robotic tools for abattoirs and for future online applications. The quantification of the biological variation and the use of models in predictive ways can speed up the development process and facilitate more intelligent tool designs. PDMs can also be used for incorporating prior knowledge in segmentation tasks of previously unseen data.

For use in the present application, the most suitable approach was found to be to threshold the varimax model, as it allowed an appropriate trade-off between sparsity, near-optimal reconstruction error and interpretability of the modes. The choice of sparsity is based on the reconstruction error since this is essential to the application at hand.

Acknowledgements

The authors would like to thank Eli V. Olsen and Finn Hansen from the Danish Meat Research Institute for their help in this work. Karl Sjöstrand kindly supplied the Matlab toolbox used for the SPCA and Jurgen Fripp along with the anonymous reviewers are acknowledged for several suggestions which greatly improved the manuscript. Simon Palmer is acknowledged for proofreading the manuscript. The CT data was provided by the Danish Meat Research Institute as a part of the project "The Virtual Butcher" funded by the Danish Pig Levy Fund and the Directorate for Food, Fisheries and Agri Business.

Estimation of Shape Model Parameters for 3D Surfaces

Søren G. H. Erbou, Sune Darkner, Jurgen Fripp, Sébastien Ourselin, Bjarne K. Ersbøll

Abstract

Statistical shape models are widely used as a compact way of representing shape variation. Fitting a shape model to unseen data enables characterizing the data in terms of the model parameters. In this paper a Gauss-Newton optimization scheme is proposed to estimate shape model parameters of 3D surfaces using distance maps, which enables the estimation of model parameters without the requirement of point correspondence. For applications with acquisition limitations such as speed and cost, this formulation enables the fitting of a statistical shape model to arbitrarily sampled data. The method is applied to a database of 3D surfaces from a section of the porcine pelvic bone extracted from 33 CT scans. A leave-one-out validation shows that the parameters of the first 3 modes of the shape model can be predicted with a mean difference within $[-0.01, 0.02]$ from the true mean, with a standard deviation less than 0.34.

9.1 Introduction

Statistical shape models (SSM) [37] are often used to characterize unseen shapes in terms of model parameters which can be used for classification or regression. In order to estimate the shape model parameters of an unseen shape, full point correspondence is usually needed to be able to project the shape into the parameter space. Obtaining full point correspondence might not be possible in

some applications due to restrictions such as acquisition and computation time, dosage (CT) and cost. In such applications there is a need for registration of dense models to incomplete data and for parameter estimation of the unseen shape.

In [163] van Assen *et al.* proposed a method for fitting a dense model to sparse data. Model points near sparse data points are propagated onto void areas using a Gaussian kernel in order to achieve (pseudo-) correspondence making it possible to estimate model parameters. The framework is applied to segmentation of cardiac MRI data and different sparsity schemes are tested. Rajamani *et al.* [129] formulated an algorithm for matching a SSM to sparse digitized points to create patient specific models for pre-operative planning. A linear system of equations is solved to obtain a least squares fit of the model to the digitized points. A Mahalanobis distance based regularization term and M-estimator based weighting of the digitized points are included in the matching algorithm. Due to the nature of their applications both papers focus on the reconstruction error but not on how well the actual model parameters are estimated.

In this paper the focus is on how accurate the model parameters can be estimated. For applications where the parameters are used for classification or regression it is important to quantify how trustworthy this estimate is. An iterative Gauss-Newton optimization algorithm is proposed for fitting a SSM to unseen data using sampled distance maps. It is investigated on dense data, without requiring point correspondence and in future papers the effect of reducing the amount of data, i.e. increasing sparsity, will be investigated. Several authors, e.g. Golland *et al.* [66], have proposed representing shapes using distance maps. This results in a more dense model which would not be feasible in the present application.

The proposed method is applied to a SSM of a porcine bone structure which will be used in a slaughterhouse robotic tool. In this specific application the model parameters are interesting as they can be used to obtain a relation with specific quality measures of the carcasses. The method is also applicable in a range of biomedical applications.

9.2 Methods

9.2.1 Statistical shape models

SSM's were proposed by Cootes *et al.* as a compact way of describing shape variation in a data set [37]. Let the n shapes, or in our case 3D surfaces, be represented by k corresponding 3D points, each arranged in a $3k$ vector \mathbf{s} . The

idea is to formulate a parameterized model of the form $\mathbf{s} = M(\mathbf{b})$ describing the variation seen in the data, where \mathbf{b} is a vector of shape parameters of the model M . To exclude the effects of translation, rotation and scaling, a generalized Procrustes alignment is performed before constructing the shape model [72]. The sample mean ($\bar{\mathbf{s}} = 1/n \sum_{i=1}^n \mathbf{s}_i$) and sample covariance matrix ($\mathbf{C} = 1/(n-1) \sum_{i=1}^n (\mathbf{s}_i - \bar{\mathbf{s}})(\mathbf{s}_i - \bar{\mathbf{s}})^T$) are then computed. Since the original parameter space is usually much larger than the number of observations ($3k \gg n$) applying principal components analysis (PCA) on the covariance matrix is an obvious choice for dimensionality reduction. The PCA determines the main axes (eigenvectors ϕ_i) of variation of the data and sorts them according to the amount of variation they describe (eigenvalues λ_i). The model can then be formulated as a perturbation of the mean shape:

$$\mathbf{s} = \bar{\mathbf{s}} + \Phi \mathbf{b} \quad (9.1)$$

where Φ is the matrix composed of the eigenvectors ϕ_i .

The model parameters of a new aligned shape \mathbf{s}' can be obtained by projecting it into the parameter space,

$$\mathbf{b}' = \Phi^T (\mathbf{s}' - \bar{\mathbf{s}}). \quad (9.2)$$

This is only possible if all the k points of the aligned shape are available.

9.2.2 Optimization algorithm

The Lucas-Kanade algorithm for image registration was originally formulated using image intensities [12, 104] and was typically applied within fields such as stereo vision and motion analysis. It is an iterative Gauss-Newton optimization algorithm. In the following the parameter estimation of the SSM is considered as a constrained registration problem, thus the Lukas-Kanade approach can be applied. This allows parameter estimation without all the points being available.

Let I be the signed distance map of the input surface and T the signed distance map of the template surface, with regions of the template surface that are within the input surface having negative distance. Furthermore let $\mathbf{x} = (x, y, z)^T$ be a vector of sample points in the distance maps, \mathbf{p} be a set of parameters and $\mathbf{W}(\mathbf{x}; \mathbf{p})$ a warp of \mathbf{x} with \mathbf{p} . The objective function to be minimized is the sum of squared differences between the warped I , and T ,

$$\sum_{\mathbf{x}} [I(\mathbf{W}(\mathbf{x}; \mathbf{p})) - T(\mathbf{x})]^2. \quad (9.3)$$

This can be formulated iteratively with incremental updates of \mathbf{p} using a Gauss-

Newton scheme [104],

$$\sum_{\mathbf{x}} [I(W(\mathbf{x}; \mathbf{p} + \Delta \mathbf{p})) - T(\mathbf{x})]^2. \quad (9.4)$$

For each step the parameters are updated,

$$\mathbf{p} \leftarrow \mathbf{p} + \Delta \mathbf{p}, \quad (9.5)$$

and this procedure is repeated until convergence. Linearizing by performing a first order Taylor expansion of eq. 9.4 results in,

$$\sum_{\mathbf{x}} [I(\mathbf{W}(\mathbf{x}; \mathbf{p})) + \nabla I \frac{\partial \mathbf{W}(\mathbf{x}; \mathbf{p})}{\partial \mathbf{p}} \Delta \mathbf{p} - T(\mathbf{x})]^2. \quad (9.6)$$

where ∇I is the gradient of I evaluated at $\mathbf{W}(\mathbf{x}; \mathbf{p})$ and $\frac{\partial \mathbf{W}(\mathbf{x}; \mathbf{p})}{\partial \mathbf{p}}$ is the Jacobian of the warp. Solving for $\Delta \mathbf{p}$ reveals,

$$\Delta \mathbf{p} = \mathbf{H}^{-1} \sum_{\mathbf{x}} \left[\nabla I \frac{\partial \mathbf{W}(\mathbf{x}; \mathbf{p})}{\partial \mathbf{p}} \right]^T [T(\mathbf{x}) - I(\mathbf{W}(\mathbf{x}; \mathbf{p}))] \quad (9.7)$$

where H is the Gauss-Newton approximation to the Hessian,

$$\mathbf{H} = \sum_{\mathbf{x}} \left[\nabla I \frac{\partial \mathbf{W}(\mathbf{x}; \mathbf{p})}{\partial \mathbf{p}} \right]^T \left[\nabla I \frac{\partial \mathbf{W}(\mathbf{x}; \mathbf{p})}{\partial \mathbf{p}} \right]. \quad (9.8)$$

Since I consists of distances to the surface to be registered, the gradient (∇I) corresponds to inward pointed normals of the surface evaluated at $\mathbf{W}(\mathbf{x}; \mathbf{p})$. If the surface is moved along the inward pointed normal (away from the sample \mathbf{x}) the distance I increases.

The warp $\mathbf{W}(\mathbf{x}; \mathbf{p})$ can be any type, e.g. rigid, affine or nonrigid transformation with corresponding parameters \mathbf{p} [12, 166]. In our case the warp is $\mathbf{W}(\mathbf{x}; \mathbf{p}) = \mathcal{C}(\mathbf{x}, \mathbf{s})$. $\mathcal{C}(\mathbf{x}, \mathbf{s})$ is the set of points in the warped surface \mathbf{s} , eq. 9.1, that are closest point to each sample in \mathbf{x} . These are obtained using a kd-tree. The parameters \mathbf{p} are the first t shape model parameters weighted by the square root of their corresponding eigenvalues, normalizing \mathbf{p} to standard deviations ($\mathbf{p} = (b_1/\sqrt{\lambda_1}, \dots, b_t/\sqrt{\lambda_t})^T$) off the mean in model parameter space.

∇I is computed as the negative mean of the normals of the faces connected to each point in $\mathbf{W}(\mathbf{x}; \mathbf{p})$.

$$\nabla I_i = -\frac{1}{f_i} \sum_{k=1}^{f_i} \mathbf{v}_k, \quad (9.9)$$

where f_i is the number of faces connected to the i^{th} vertex/point and \mathbf{v}_k is the outwards normal of the k^{th} connected face. Using the angle weighted normals would likely give a better estimate of the mean curvature at the vertices, but it would be computationally more expensive. The Jacobian of the warp for the i^{th} sample in \mathbf{x} is composed from the respective counterparts in the eigenvectors of the model.

$$\frac{\partial \mathbf{W}(\mathbf{x}_i; \mathbf{p})}{\partial \mathbf{p}} = \begin{pmatrix} \phi_{x_i,1}\sqrt{\lambda_1} & \dots & \phi_{x_i,t}\sqrt{\lambda_t} \\ \phi_{y_i,1}\sqrt{\lambda_1} & \dots & \phi_{y_i,t}\sqrt{\lambda_t} \\ \phi_{z_i,1}\sqrt{\lambda_1} & \dots & \phi_{z_i,t}\sqrt{\lambda_t} \end{pmatrix} \quad (9.10)$$

In the above formulation the sample vector \mathbf{x} can be constructed arbitrarily, (within a sensible range from the surface) and the optimization algorithm will seek to minimize the rms error between the distance maps. It is therefore possible to estimate the model parameters without having full point correspondence.

To estimate \mathbf{p} requires an initial estimate, which in this case is $\mathbf{p} = \mathbf{0}$ which corresponds to the mean shape of the shape model. By applying equations 9.7, 9.9, 9.10, 9.8 & 9.5 we obtain a new estimate of $\Delta \mathbf{p}$ that minimize a first order estimate of a quadratic surface to the parameter space. If this is far from the global optimum, the estimate will be inaccurate. To rectify this a line search is applied at each iteration if the full step did not reduce the cost function. This is initialized with a small step size, which doubles until one step before the cost function starts to increase, which ensures a reasonable tradeoff between computations and optimum step size.

To improve speed several papers, e.g. [12, 166], propose to formulate the Lukas-Kanade algorithm in the inverse compositional way making it possible to pre-compute several steps, especially the Hessian in eq. 9.8. This is beneficial if the sample vector \mathbf{x} is very large, which it is not in the present application. Furthermore applying the inverse compositional algorithm would require the use of surface information from the template image, which may not be feasible to acquire.

9.2.3 Validation

The validation is performed in a leave-one-out scheme (LOO), where the model parameters for each surface i are estimated using a SSM constructed using all but the i^{th} surface. The true set of parameters are found by projecting the aligned surface into the parameter space of the model using eq. 9.2. The actual parameter estimates and the rms errors (point-to-point) are then compared. Only absolute distances less than 5 mm are included when computing the rms

error in order to reduce the effect of outliers which can occur due to missing and non-corresponding regions.

9.3 Data

The method is applied to a data set consisting of 33 cases of 3D surfaces from a section of the porcine pelvic bone. Implicit surfaces are extracted from CT scans using radial basis functions [162] from which the surfaces are reconstructed as triangular meshes. The surfaces of the bone of interest are disconnected from the skeleton by planes and therefore have two open ends. Furthermore they would have genus 1 topology, i.e. topological similar to a torus, if the ends were closed.

Correspondence is obtained using the iterative closest point (ICP) algorithm [15] using a similarity transform (translation, rotation and scaling) extended with a point-to-surface step determined by a search along the direction of the estimated vertex normal to the other surface. A reference shape is constructed by initially performing registration of a specific shape to the other shapes, then computing a new reference shape as the mean, performing registration of this to all shapes until convergence of the mean shape. The reference shape consists of 3815 vertices and 7397 faces.

Choosing the number of modes (t) to include in the model is a tradeoff between including the general intrinsic variation of the data and excluding noise. Applying parallel analysis (PA) as suggested by Horn [83], results in 7-9 modes of variation to be included for the different LOO models. PA only includes modes that contain more variation than can be explained by noise, i.e. modes with intrinsic variation less than the noise level are excluded.

Since we investigate the parameter estimation ability of the algorithm for this specific data set, the sample vector \mathbf{x} is composed of the full point set of the surface to register the model to. $T(\mathbf{x})$ is $\mathbf{0}$.

9.4 Results

Figure 9.1 shows the first 3 modes of variation (rows) in one of the LOO models, perturbed -3 std. (left column) and +3 std. (right column). The middle column is the mean shape, with the first 3 and 7 modes containing 45% and 65% of the variation in the data, respectively.

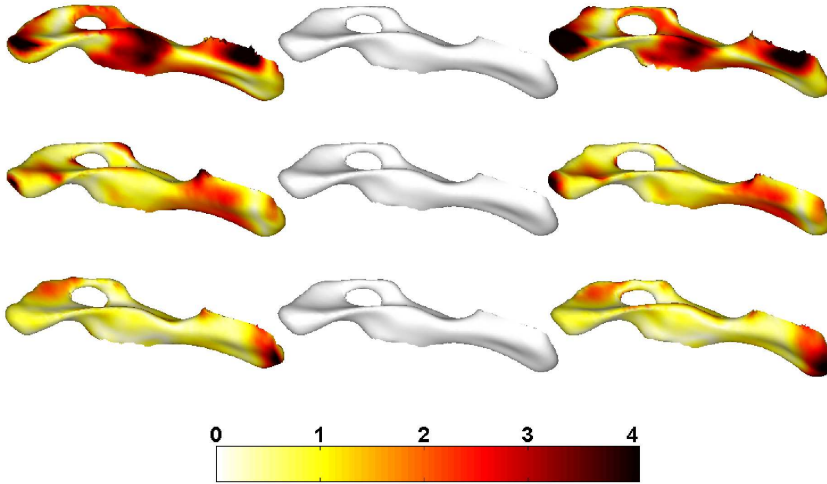


Figure 9.1: Three principal modes of variation (rows) cover 25%, 12% and 8% respectively of the total variation in the data. Left and right columns denote -3 and $+3$ std. from the mean shape (middle column). The color coding indicates the absolute distance in mm to the mean shape.

When estimating shape model parameters errors accumulate through modes and it might not be possible to estimate more than the first few of modes. If the estimate of the first mode is incorrect, the other modes try to compensate in terms of reducing the rms error of the point-to-point distance. With that in mind 3 schemes are reported, one where all the model parameters are estimated in a combined optimization (comb.) and 2 sequential schemes where only the last mode is estimated, fixing the previous modes to the estimated value (seq-est), and to the true value (seq-true). The latter scheme is included for comparison even though the true parameters would not be accessible in an application. Still it gives an indication of the error levels that should be expected.

In the 3 schemes the true pose is used as initialization and parameter estimates and rms errors compared when including from 1 to 7 modes. The true pose is defined as the pose obtained from the ICP registration, applying the similarity transform. The effect of not having the true pose will be investigated in future work. Figure 9.2 and table 9.1 show the mean and std. of the difference between the estimated and true values of the parameter estimates in the LOO validation. For the majority of cases the mean is within ± 0.1 std. from the true value, which seems reasonable. The std. of the difference is more interesting, since it gives an idea of how far off most of the estimates are. When estimating 1 or 2 modes the three schemes approximately have the same std. of the difference, less than 0.35. When estimating 3-6 modes the two sequential schemes have a std. within

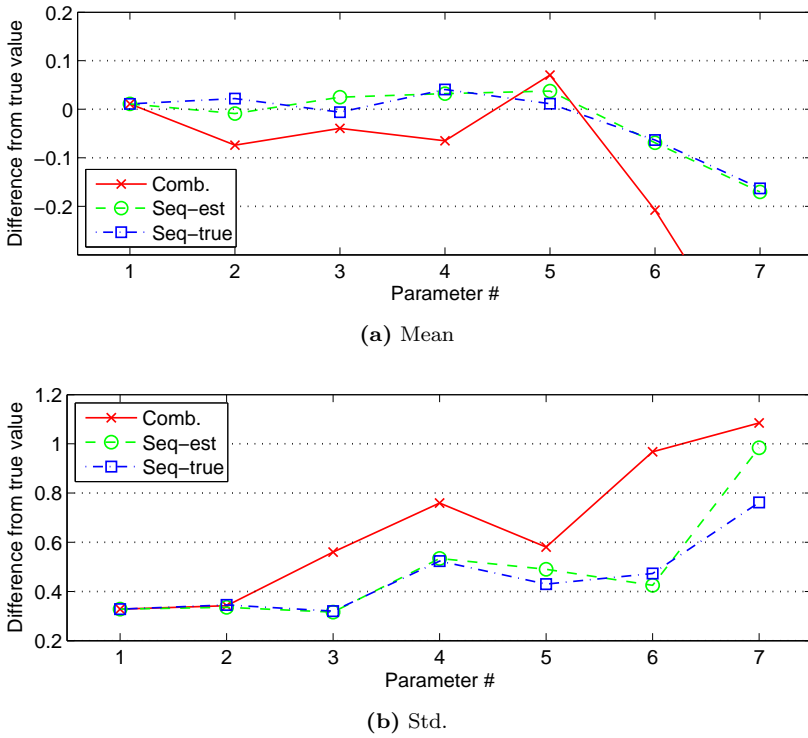


Figure 9.2: Difference between estimated and true parameter values for the three optimization schemes.

0.53, while the std. of the combined scheme only is within 0.76 when estimating 3-5 modes. This shows that the parameter estimates for the combined scheme try to balance each other out, resulting in less reliable estimates.

Figure 9.3 shows the mean rms errors for the three parameter estimation schemes and for the true set of parameters. For the initial set of parameters, the mean rms error is 1.85 mm. It shows that the more parameters that are estimated in the combined scheme, the more likely the optimization is to converge to a local minima, where the rms error is significantly higher than for the true set of parameters. For the seq-est scheme the difference is within 0.01 mm for 1-5 modes. This indicates that the seq-est scheme is preferable to the combined scheme, revealing similar rms values as for the true parameter values when using 1-5 modes. The std. of modes higher than the third mode are substantially higher than for the first three modes, so including more than 3 modes should depend on the acceptable level for the std. of the difference. For the present application it is suggested to include 3 modes.

Modes	Comb.	Seq-est	Seq-true
1	0.01 (0.33)	0.01 (0.33)	0.01 (0.33)
2	-0.07 (0.34)	-0.01 (0.34)	0.02 (0.35)
3	-0.04 (0.56)	0.02 (0.32)	-0.01 (0.32)
4	-0.07 (0.76)	0.03 (0.53)	0.04 (0.52)
5	0.07 (0.58)	0.04 (0.49)	0.01 (0.43)
6	-0.21 (0.97)	-0.07 (0.42)	-0.06 (0.47)
7	-0.55 (1.08)	-0.17 (0.98)	-0.16 (0.76)

Table 9.1: Difference between estimated and true parameter values for the three schemes when estimating 1 through 7 modes. Mean and (std.) are reported.

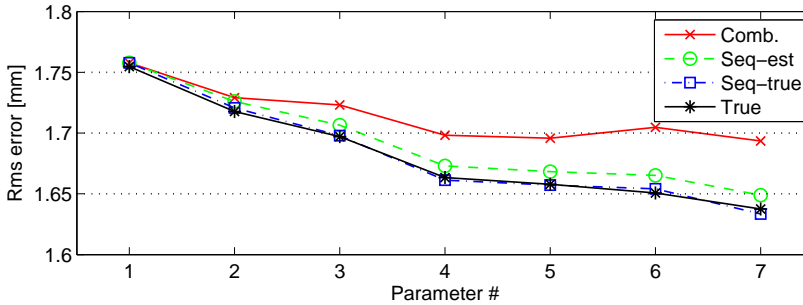


Figure 9.3: Mean rms error of leave-one-out validation for different number of modes included, the std. is 0.12 mm. The mean value of the initial rms error is 1.85 mm.

Figure 9.4 shows the mean and std. of the rms error for each surface point plotted on the mean surface, when 3 modes of variation are used. The error is nicely distributed over the central parts of the shape, with the main errors located at either end and along the edge of the top right part of the hole. The mean rms error is 1.50 mm and the mean std. is 0.59 mm.

9.5 Conclusion

An iterative Gauss-Newton algorithm is applied to estimate statistical shape model parameters for unseen data. The optimization is driven by sampling in distance maps, which can be done arbitrarily. This enables the estimation of model parameters without the need of full point correspondence, which would be needed if the aligned shape were to be projected into the parameter space.

For applications where it is of interest to fit a dense model to sparse data in order to estimate model parameters e.g. for classification or regression purposes this

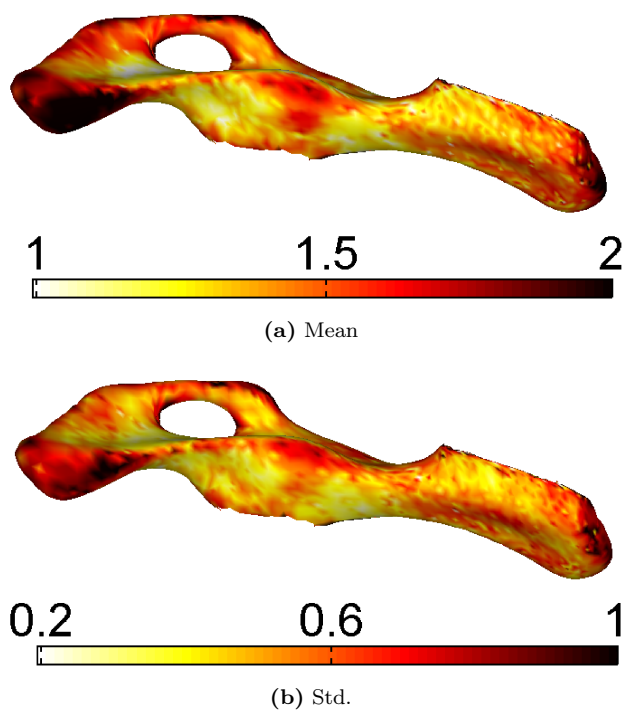


Figure 9.4: Mean (a) and std. (b) of rms error, in mm, for each point plotted on the mean shape and reconstructed using 3 modes. The mean rms error on the surface is 1.50 mm. and the mean of the std. is 0.59 mm.

method can be applied. This is important in applications where time, dosage, cost etc. are issues.

Leave-one-out validation of parameter estimates for a data set of 3D surfaces of a specific porcine bone shows that the three primary modes of the statistical shape model can be estimated with a mean difference between $[-0.01, 0.02]$ std. and with a std. of the difference within 0.34. This is done using a sequential estimation scheme where each parameter is estimated sequentially with previous parameters fixed. If 6 modes are estimated the upper limit of the std. of the difference increases to 0.53 and the mean difference is between $[-0.07, 0.04]$ std. The difference between the true and the estimated rms error is below 0.01 mm. The rms error decreases when increasing the number of modes, but the parameter estimates are only reliable enough for the first 3 modes in the present application.

The sample vector that drives the optimization can be arbitrarily defined, which is a topic for future work, along with the introduction of weights on the cost function. Other topics to investigate include applying more localized models, i.e. ICA-models, varimax rotation or sparse PCA.

The statistical shape model will be used in a slaughterhouse robotic tool and the parameters are of interest as they can be used to obtain a relation with specific quality measures of the carcasses.

Acknowledgements

The CT data was provided by the Danish Meat Research Institute as a part of the project "The Virtual Butcher" funded by the Danish Pig Levy Fund and the Directorate for Food, Fisheries and Agri Business.

Accelerated 3D Image Registration

Martin Vester-Christensen, Søren G. Erbou, Sune Darkner and Rasmus Larsen

Abstract

Image registration is an important task in most medical imaging applications. Numerous algorithms have been proposed and some are widely used. However, due to the vast amount of data collected by e.g. a computed tomography (CT) scanner, most registration algorithms are very slow and memory consuming. This is a huge problem especially in atlas building, where potentially hundreds of registrations are performed. This paper describes an approach for accelerated image registration. A grid-based warp function proposed by Cootes and Twining, parameterized by the displacement of the grid-nodes, is used. Using a coarse-to-fine approach, the composition of small diffeomorphic warps, results in a final diffeomorphic warp. Normally the registration is done using a standard gradient-based optimizer, but to obtain a fast algorithm the optimization is formulated in the inverse compositional framework proposed by Baker and Matthews. By switching the roles of the target and the input volume, the Jacobian and the Hessian can be pre-calculated resulting in a very efficient optimization algorithm. By exploiting the local nature of the grid-based warp, the storage requirements of the Jacobian and the Hessian can be minimized. Furthermore, it is shown that additional constraints on the registration, such as the location of markers, are easily embedded in the optimization. The method is applied on volumes built from CT-scans of pig-carcasses, and results show a two-fold increase in speed using the inverse compositional approach versus the traditional gradient-based method.

10.1 Introduction

Registration of images is an important and actively researched area of medical imaging. It is the task of transforming the geometry of two or more images such that their corresponding regions are aligned. The need may arise from comparison of images from different imaging modalities, from images obtained at different times, from different patients, or from comparison with a patient atlas. Registration is needed in a wide variety of medical applications, e.g. for diagnostic purposes, for pre-surgery planning or for treatment estimation. The medical imaging hardware of today produce images of high resolution, and as a consequence a huge amount of data need processing in order to solve the registration problem. The requirements on the processing hardware are very high in terms of storage capability, CPU speed, and maybe most importantly in memory capacity.

A range of different registration algorithms have been produced in the recent years. The algorithm described in this paper, belongs to the class of parameterized methods. Hence the registration can be described by a set of parameters. Existing methods includes Rueckert *et al.* [134] using B-splines on a grid to define the warp-field, Cootes *et al.* [40] use bounded diffeomorphisms, warping pixels inside a unit sphere based on the displacement of the sphere center. An example of the non-parametric approach is found in Christensen *et al.* [29] which solve partial differential equations for fluid motions to align images.

This paper presents the acceleration of an image registration algorithm by Cootes *et al.* [41]. An inverse compositional optimization scheme proposed by Baker and Matthews [12] is used. It is a Gauss-Newton approach, but in which the Jacobian and the estimated Hessian can be pre-computed. However, to be tractable memory wise, this requires exploitation of the properties of the registration algorithm. An additional benefit of the Gauss-Newton approach is the ease of which addition of soft constraints on the registration can be added. Comparison is made with optimization using the Lucas-Kanade scheme [104].

The paper consists of the following. First the registration algorithm is described. In 10.2.1 the image registration algorithm is described, followed by outlining of the Lucas-Kanade algorithm, in 10.2.2, and the inverse compositional optimization algorithm, in 10.2.3. Addition of soft constraints is described in 10.2.4. Section 10.3 describes the results obtained by comparing the two optimization schemes.

10.2 Methods

The image registration algorithm utilized in this paper is proposed by Cootes *et al.* [41] which builds on the algorithms presented by Rueckert *et al.* [136]. The image registration is performed by composing a series of grid-based diffeomorphic warps which ensures the resulting warp being diffeomorphic.

10.2.1 Grid-Based Diffeomorphisms

A grid-based warp is represented by a grid of nodes¹, cf. figure 10.1. The transformation \mathbf{W} of a pixel $\mathbf{x} = (x, y, z)$ is found by interpolating the displacement \mathbf{d} of its surrounding grid nodes. In 3D the interpolating scheme is as below,

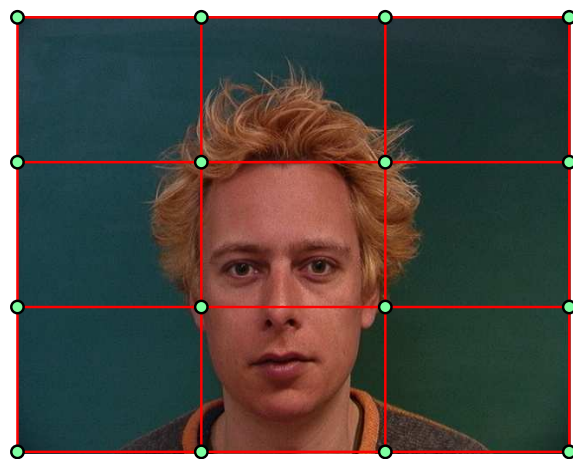
$$\begin{aligned}
 \mathbf{W}(\mathbf{x}; \alpha) &= k(x-i)k(y-j)k(z-l)\mathbf{d}_{i,j,l} \\
 &+ k(i+1-x)k(y-j)k(z-l)\mathbf{d}_{i+1,j,l} \\
 &+ k(x-i)k(j+1-y)k(z-l)\mathbf{d}_{i,j+1,l} \\
 &+ k(i+1-x)k(j+1-y)k(z-l)\mathbf{d}_{i+1,j+1,l} \\
 &+ k(x-i)k(y-j)k(l+1-z)\mathbf{d}_{i,j,l+1} \\
 &+ k(i+1-x)k(y-j)k(l+1-z)\mathbf{d}_{i+1,j,l+1} \\
 &+ k(x-i)k(j+1-y)k(l+1-z)\mathbf{d}_{i,j+1,l+1} \\
 &+ k(i+1-x)k(j+1-y)k(l+1-z)\mathbf{d}_{i+1,j+1,l+1},
 \end{aligned} \tag{10.1}$$

where $k(\cdot)$ denotes a suitable kernel function which is non-zero only for $i \leq x < i+1$, $j \leq y < j+1$ and $l \leq z < l+1$. The warp is parameterized with the components of the displacement vectors \mathbf{d} . Thus, with a $3 \times 3 \times 3$ grid in 3D, the warp consist of 81 parameters. The kernel is chosen as $k(r) = \frac{1}{2}(1 + \cos(\pi r))$ which gives a smooth and invertible mapping [41] given that $-\frac{1}{\pi} < r < \frac{1}{\pi}$. Using the interpolating scheme the warp is regularized by the coarseness of the grid. Thus, a pixel cannot move outside the bounding box provided by the surrounding grid nodes. However, to represent a complex transformation several simple warps can be composed,

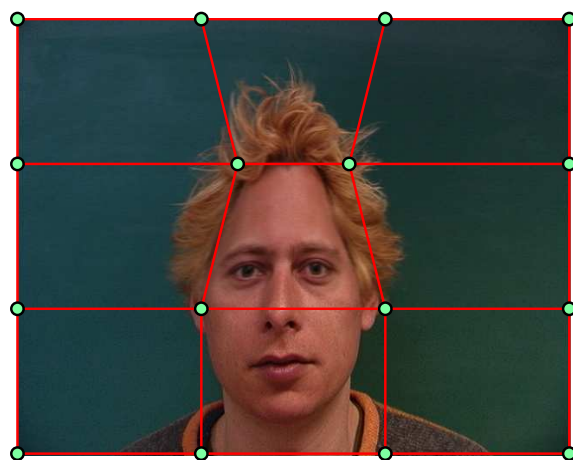
$$\mathbf{W}(\mathbf{x}; \mathbf{p}) = \mathbf{W}(\mathbf{x}; \delta_1) \circ \mathbf{W}(\mathbf{x}; \delta_2) \dots \mathbf{W}(\mathbf{x}; \delta_{n-1}) \circ \mathbf{W}(\mathbf{x}; \delta_n), \tag{10.2}$$

where $\mathbf{W}(\mathbf{x}; \delta_1) \circ \mathbf{W}(\mathbf{x}; \delta_2) = \mathbf{W}(\mathbf{W}(\mathbf{x}; \delta_2); \delta_1)$ denotes the composition of two warps. The warps are applied in a fine to coarse manner.

¹The following is an elaboration on the paper by Cootes *et al.* [41], but is included here for completeness.



(a) Before.



(b) After.

Figure 10.1: The displacement of a pixel is governed by the displacement of its surrounding grid nodes [149].

10.2.2 Image Registration using the Lucas-Kanade Algorithm

The goal of the image registration algorithm is to align a target and a input image such that the difference is minimized. This is quantified by the minimization of the sum of squared residuals,

$$\mathbf{F}(\mathbf{p}) = \sum_{\mathbf{x}} [T(\mathbf{x}) - I(\mathbf{W}(\mathbf{x}; \mathbf{p}))]^2, \quad (10.3)$$

where I is the input image and T is the target image. This can be minimized using a Gauss-Newton optimization scheme[104],

$$F(\mathbf{p}) = \frac{1}{2} \sum_{\mathbf{x}} [T(\mathbf{x}) - I(\mathbf{W}(\mathbf{x}; \mathbf{p} + \Delta\mathbf{p}))]^2, \quad (10.4)$$

which by Taylor expansion and solving for $\Delta\mathbf{p}$ gives,

$$\Delta\mathbf{p} = \mathbf{H}^{-1} \sum_{\mathbf{x}} \left[\nabla I(\mathbf{W}(\mathbf{x}; \mathbf{p})) \frac{\partial \mathbf{W}(\mathbf{x}; \mathbf{p})}{\partial \mathbf{p}} \right]^\top E(\mathbf{x}), \quad (10.5)$$

where \mathbf{H} is the Gauss-Newton approximation to the Hessian,

$$\mathbf{H} = \sum_{\mathbf{x}} \left[\nabla I(\mathbf{W}(\mathbf{x}; \mathbf{p})) \frac{\partial \mathbf{W}(\mathbf{x}; \mathbf{p})}{\partial \mathbf{p}} \right]^\top \left[\nabla I(\mathbf{W}(\mathbf{x}; \mathbf{p})) \frac{\partial \mathbf{W}(\mathbf{x}; \mathbf{p})}{\partial \mathbf{p}} \right], \quad (10.6)$$

and the error is,

$$E(\mathbf{x}) = T(\mathbf{x}) - I(\mathbf{W}(\mathbf{x}; \mathbf{p})). \quad (10.7)$$

The warp parameters \mathbf{p} are updated using,

$$\mathbf{p} \leftarrow \mathbf{p} + \Delta\mathbf{p}. \quad (10.8)$$

The Jacobian is found to be,

$$\mathbf{J} = \sum_{\mathbf{x}} \left[\nabla I(\mathbf{W}(\mathbf{x}; \mathbf{p})) \frac{\partial \mathbf{W}(\mathbf{x}; \mathbf{p})}{\partial \mathbf{p}} \right], \quad (10.9)$$

where $\nabla I(\mathbf{W}(\mathbf{x}; \mathbf{p}))$ is the image gradient of the input image sampled at the points $\mathbf{W}(\mathbf{x}; \mathbf{p})$, and $\frac{\partial \mathbf{W}(\mathbf{x}; \mathbf{p})}{\partial \mathbf{p}}$ is the derivative of the warp function with respect to the parameters.

This optimization scheme requires computation of the Jacobian \mathbf{J} and the inverse Hessian \mathbf{H}^{-1} at each iteration. For large volumes and large grids, this is very computationally demanding. However, the Hessian is symmetric and very sparse thus enabling the utilization of fast schemes for solving large sparse linear equations [69].

10.2.3 Inverse Compositional Image Registration

To overcome the drawbacks of the Gauss-Newton scheme of calculating the Jacobian and the Hessian in each iteration, Baker and Matthews [12] recently proposed the *Inverse Compositional Algorithm*, in which the Jacobian and the Hessian can be pre-computed. As the name implies the algorithm consists of two innovations. The compositional part refers to the updating of the parameters and the inverse part indicates that the image and the target switches roles. The cost function in 10.4 is changed to,

$$F_{ic}(\mathbf{p}) = \frac{1}{2} \sum_{\mathbf{x}} [T(\mathbf{W}(\mathbf{x}; \Delta \mathbf{p})) - I(\mathbf{W}(\mathbf{x}; \mathbf{p}))]^2. \quad (10.10)$$

Solving for $\Delta \mathbf{p}$ gives,

$$\Delta \mathbf{p} = -\mathbf{H}_{ic}^{-1} \sum_{\mathbf{x}} \left[\nabla T(\mathbf{x}) \frac{\partial \mathbf{W}(\mathbf{x}; \mathbf{0})}{\partial \mathbf{p}} \right]^\top E(\mathbf{x}). \quad (10.11)$$

The update to the warp is,

$$\mathbf{W}(\mathbf{x}; \mathbf{p}) = \mathbf{W}(\mathbf{x}; \mathbf{p}) \circ \mathbf{W}(\mathbf{x}; \Delta \mathbf{p})^{-1}, \quad (10.12)$$

In equation 10.10 it can be seen that the incremental warp $\mathbf{W}(\mathbf{x}; \Delta \mathbf{p})$ applies only to the target T , and thus the Taylor expansion is around $\mathbf{p} = \mathbf{0}$, yielding the Jacobian

$$\mathbf{J}_{ic} = \sum_{\mathbf{x}} \left[\nabla T(\mathbf{W}(\mathbf{x}; \mathbf{0})) \frac{\partial \mathbf{W}(\mathbf{x}; \mathbf{0})}{\partial \mathbf{p}} \right]. \quad (10.13)$$

and thus the Hessian \mathbf{H}_{ic} is,

$$\mathbf{H}_{ic} = \sum_{\mathbf{x}} \left[\nabla T(\mathbf{x}) \frac{\partial \mathbf{W}(\mathbf{x}; \mathbf{0})}{\partial \mathbf{p}} \right]^\top \left[\nabla T(\mathbf{x}) \frac{\partial \mathbf{W}(\mathbf{x}; \mathbf{0})}{\partial \mathbf{p}} \right]. \quad (10.14)$$

The Jacobian is independent of \mathbf{p} and $\nabla T(\mathbf{x})$ is the image gradient of the target, thus enabling pre-computation of the Jacobian and the Hessian.

Baker and Matthews [12] prove that the update $\Delta \mathbf{p}$ calculated using the inverse compositional algorithm is equivalent, to a first order approximation, to the update calculated using the Lucas-Kanade algorithm.

10.2.4 Adding Constraints

Baker *et al.* [13] describe how to incorporate prior information on the warp parameters. This could for instance be landmark or volume constraints formulated as an additional term in the expression to be minimized, i.e. as weighted

soft constraints to equation 10.3,

$$\frac{1}{2} \sum_{\mathbf{x}} [T(\mathbf{x}) - I(\mathbf{W}(\mathbf{x}; \mathbf{p}))]^2 + \alpha \sum_{i=1}^K C_i^2(\mathbf{p}). \quad (10.15)$$

K is the number of constraints, C_i is a vector of functions containing the prior on the parameters for the i^{th} constraint and α is a weight controlling the emphasis on the prior term. In the inverse compositional framework this corresponds to equation 10.10,

$$\frac{1}{2} \sum_{\mathbf{x}} [T(\mathbf{W}(\mathbf{x}; \Delta \mathbf{p}) - I(\mathbf{W}(\mathbf{x}; \mathbf{p}))]^2 + \alpha \sum_{i=1}^K C_i^2(\mathbf{p} + \frac{\partial \mathbf{p}'}{\partial \Delta \mathbf{p}} \Delta \mathbf{p}). \quad (10.16)$$

Approximating this with a first order Taylor expansion gives the following update equations for the gradient $\Delta \mathbf{p}$ and the Hessian,

$$\Delta \mathbf{p} = -\mathbf{H}_{ic, C_i}^{-1} \left[\sum_{\mathbf{x}} \left[\nabla T(\mathbf{x}) \frac{\partial \mathbf{W}(\mathbf{x}; \mathbf{0})}{\partial \mathbf{p}} \right]^T E(\mathbf{x}) + \alpha_{Gr} \sum_{i=1}^K \left[\frac{\partial C_i}{\partial \mathbf{p}} \frac{\partial \mathbf{p}'}{\partial \Delta \mathbf{p}} \right]^T C_i(\mathbf{p}) \right] \quad (10.17)$$

$$\mathbf{H}_{ic, C_i} = \mathbf{H}_{ic} + \alpha_{He} \sum_{i=1}^K \left[\frac{\partial C_i}{\partial \mathbf{p}} \frac{\partial \mathbf{p}'}{\partial \Delta \mathbf{p}} \right]^T \left[\frac{\partial C_i}{\partial \mathbf{p}} \frac{\partial \mathbf{p}'}{\partial \Delta \mathbf{p}} \right]. \quad (10.18)$$

The computational cost of adding priors is that the Hessian is not constant anymore. The cost is $O(nN + n^2K + n^3)$ compared to $O(nN + n^2)$ without priors. As long as the number of constraints and the number of parameters are smaller than the number of pixels/voxels ($K \ll N$ and $n \ll N$), this cost is negligible. In order to make the prior terms robust to the number of constraints, the α weights are chosen relative to the L2-norm of the term without priors,

$$\alpha_{Gr} = \alpha_{Rel} \frac{\left\| \sum_{\mathbf{x}} \left[\nabla T(\mathbf{x}) \frac{\partial \mathbf{W}(\mathbf{x}; \mathbf{0})}{\partial \mathbf{p}} \right]^T E(\mathbf{x}) \right\|_{L2}}{\left\| \sum_{i=1}^K \left[\frac{\partial C_i}{\partial \mathbf{p}} \frac{\partial \mathbf{p}'}{\partial \Delta \mathbf{p}} \right]^T C_i(\mathbf{p}) \right\|_{L2}} \quad (10.19)$$

$$\alpha_{He} = \alpha_{Rel} \frac{\left\| \mathbf{H}_{ic} \right\|_{L2}}{\left\| \sum_{i=1}^K \left[\frac{\partial C_i}{\partial \mathbf{p}} \frac{\partial \mathbf{p}'}{\partial \Delta \mathbf{p}} \right]^T \left[\frac{\partial C_i}{\partial \mathbf{p}} \frac{\partial \mathbf{p}'}{\partial \Delta \mathbf{p}} \right] \right\|_{L2}}, \quad (10.20)$$

where $\alpha_{Rel} \geq 0$ is the relative weighting between the two terms. $\alpha_{Rel} = 0$ corresponds to the inverse compositional without the prior term.

10.2.5 Fast Grid-Based Image Registration

The inverse compositional scheme described above requires the computation the Jacobian from equation 10.13 and subsequently the Hessian from equation 10.14. To take full advantage of the inverse compositional method, they must be pre-calculated and stored. However, the storage requirement of the Jacobian can be very large. In a naive implementation using a simple $3 \times 3 \times 3$ grid, space is needed for $81 \cdot N$ floating point numbers with N being the number of pixels in the image and potentially very large. So great care must be taken in the implementation in order to exploit the speed gain provided by the inverse compositional framework.

10.2.5.1 Calculating the Jacobian and the Hessian

The Jacobian consist of the gradient $\nabla T(\mathbf{x}) = \begin{bmatrix} \frac{\partial T}{\partial x} & \frac{\partial T}{\partial y} & \frac{\partial T}{\partial z} \end{bmatrix}$ of the target image and the derivative of the warp $\frac{\partial \mathbf{W}}{\partial \mathbf{p}}$. $\nabla T(\mathbf{x})$ can be found using a simple finite difference method or more elaborate methods using B -splines or similar interpolating methods. The warp derivatives are very simple to calculate. As mentioned, the parameters of the warp are simply the $3 \cdot mnp$ ordinates of the displacements of the nodes,

$$\mathbf{p} = [d_{1,1,1}^x \ d_{1,1,1}^y \ d_{1,1,1}^z \ d_{2,1,1}^x \ d_{2,1,1}^y \ d_{2,1,1}^z \ \dots \ d_{m,n,p}^x \ d_{m,n,p}^y \ d_{m,n,p}^z], \quad (10.21)$$

for a $m \times n \times p$ grid. This and equation 10.1 yields

$$\frac{\partial \mathbf{W}}{\partial d_{i,j,l}^x} = \frac{\partial \mathbf{W}}{\partial d_{i,j,l}^y} = \frac{\partial \mathbf{W}}{\partial d_{i,j,l}^z}, \quad (10.22)$$

meaning that the derivatives corresponding to the x, y, z components of one displacement vector are equal. Each pixel \mathbf{x} contributes to eight partial derivatives only, corresponding to the eight surrounding grid nodes, cf. figure 10.2 for a 2D example. Thus, for N pixels, an $N \times 8$ floating point value representation of $\frac{\partial \mathbf{W}}{\partial \mathbf{p}}$ is possible using a simple lookup method. However, since the kernel function $k()$ only operates on the distance from a contributing pixel \mathbf{x} to a node, an even sparser representation of only $N_{reg} \times 8$ is possible. N_{reg} is the number of pixels surrounded by 8 neighboring grid nodes. For increasing grid sizes the space requirement goes down.

Another property of $\frac{\partial \mathbf{W}}{\partial \mathbf{p}}$ is seen from,

$$k(i+1-x) = 1 - k(x-i), \quad (10.23)$$

which holds for y and z as well. For a neighborhood of grid nodes, the derivative

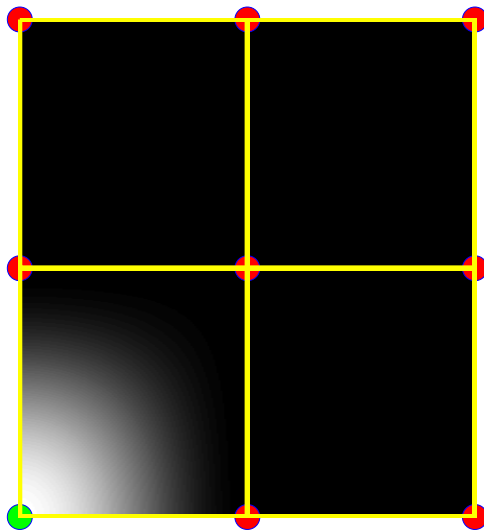


Figure 10.2: The derivative of the warp with respect to the node in the lower left corner. It is non-zero only in the region bounded by the neighboring nodes.

at $\mathbf{x} = (x, y, z)$ w.r.t. the parameters of the warp has the form,

$$\begin{aligned}
 \frac{\partial \mathbf{W}}{\partial p_{i,j,l}} &= k(x-i)k(y-j)k(z-l) \\
 \frac{\partial \mathbf{W}}{\partial p_{i+1,j,l}} &= (1-k(x-i))k(y-j)k(z-l) \\
 &\vdots \\
 \frac{\partial \mathbf{W}}{\partial p_{i+1,j+1,l+1}} &= (1-k(x-i))(1-k(y-j))(1-k(z-l)) \quad (10.24)
 \end{aligned}$$

(10.25)

Thus, to evaluate the derivative contribution for a single pixel \mathbf{x} , only three kernel function evaluations, $k(x-i)$, $k(y-j)$ and $k(z-l)$ are needed. The derivatives can then be found using simple multiplications and subtractions.

Finally the Jacobian is calculated as in equation 10.13, which means multiplying the warp derivatives with the image gradients. However, the Jacobian with the sparse representation mentioned above has a size of $N \times 24$ floating point values which requires a large amount of memory. Subsequently a compromise has to be made, and in this work the image gradients and the warp derivatives are stored separately, yielding space requirement for $N \times 3$ plus $N_{reg} \times 8$ numbers. This means the multiplication of the gradients and the derivatives must be performed each time the Jacobian is needed, yet precalculation of the Hessian is still possible.

The Hessian is calculated as in equation 10.14. The sparseness of the Jacobian is transferred into the Hessian. Figure 10.3 depicts the sparseness of the Hessian for three grid sizes. Solving equation 10.11 requires the inversion of the Hessian matrix. This usually destroys the sparseness and is very computationally demanding. Furthermore, the Hessian can be very ill-conditioned, but making use of iterative methods[69] for solving sparse linear equations, the inversion of the Hessian can be avoided.

10.2.5.2 The Image Registration Algorithm

To estimate the transformation of the input image I into the target image T minimization of equation 10.10 with respect to \mathbf{p} is required. This is done by first applying a coarse grid, e.g. $3 \times 3 \times 3$, and iteratively solving equation 10.11 until convergence. Subsequently a finer grid, e.g. $5 \times 5 \times 5$, is applied, and so forth. This enables the estimation of small local transformations while still being diffeomorphic [41]. A multilevel approach, using down-sampled versions of the images, is adopted to avoid local minima. Consequently, for each grid size,

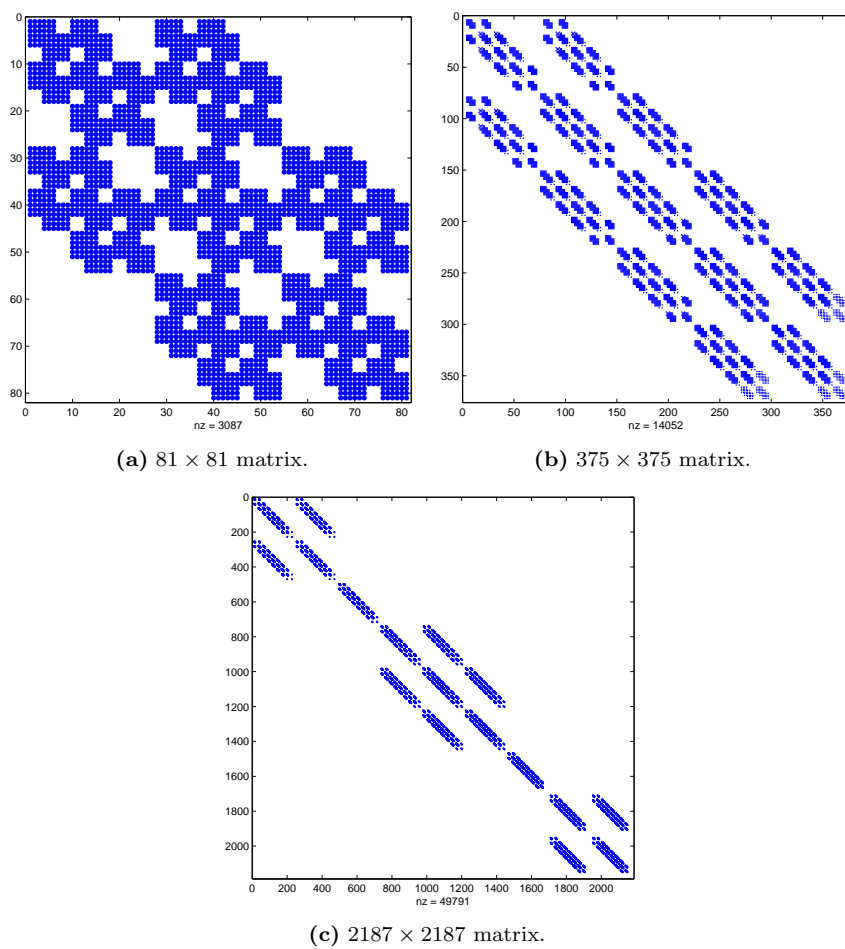


Figure 10.3: Plot of non-zero elements in Hessian matrices, for grid sizes of $3 \times 3 \times 3$, $5 \times 5 \times 5$ and $9 \times 9 \times 9$.

optimization is done in a coarse-to-fine manner as well, starting the optimization on a finer downsampling level with the parameters estimated on a coarser level. See figure 10.4. At each iteration equation 10.12 must be used to update the parameters. In this work the parameters of $\mathbf{W}(\mathbf{x}; \Delta\mathbf{p})$ is estimated with the first order approximation [13] $-\Delta\mathbf{p}$. Thus the parameter update from equation 10.12 has the form,

$$\mathbf{p} \leftarrow \mathbf{p} - \Delta\mathbf{p}. \quad (10.26)$$

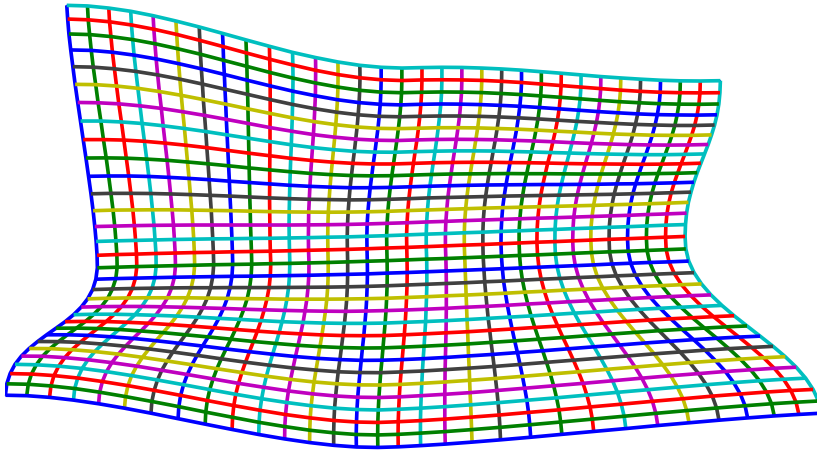
When the optimization for one grid size converges, a finer grid is applied, i.e. a $3 \times 3 \times 3$ is replaced with a $5 \times 5 \times 5$. Composition of warps of difference grid sizes is done in a simple manner. Figure 10.5 depicts the scheme. The grid nodes of the higher level warp are transformed with the lower level warp. Thus, the parameters from the lower level are transported into the higher level warp.

10.3 Results

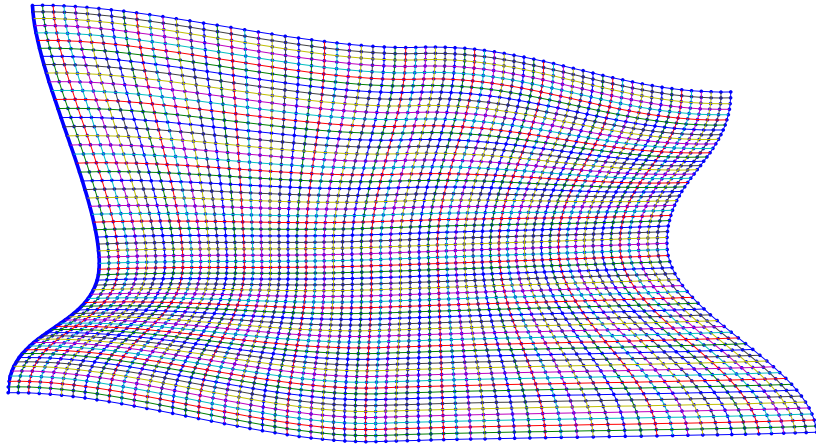
10.3.1 3D Non-Rigid Registration

5 CT-volumes of the hind part of porcine carcasses are cross-registered to compare the inverse compositional algorithm with the Lucas-Kanade algorithm. The volumes are approximately $512 \times 512 \times 170$ voxels of size $[0.67, 0.67, 2]$ mm. After rigid registration the two algorithms for non-rigid registration are applied and the speed and accuracy are compared. Due to time considerations the 20 registrations are done with images down-sampled to $\frac{1}{16}$, $\frac{1}{8}$ and $\frac{1}{4}$ of the original image size for grids of size $[3, 5, 7, 9]$ per dimension. Figure 10.6 shows three slice planes of a volume and their corresponding error images after a typical registration. The main errors are along the border of the volume due to the large difference in value between background and volume.

Rows 1 and 2 in table 10.1 show the mean value and standard deviation of the number of iterations used before convergence, the final registration error and the time consumption for the two algorithms. Row 3 shows the mean improvement when using the IC algorithm and row 4 shows a paired T-test of significant differences in the mean values. There are highly significant improvements (denoted by 1) in both speed and number of iterations. The mean final registration error of the two methods are not significantly different. In this simple test it therefore shows that the inverse compositional algorithm is as accurate as the Lucas-Kanade algorithm, as expected, but is twice as fast for registration of CT-volumes. The results are obtained using a Dell Latitude 810D, with a 2.0Ghz CPU and 2 GB of RAM. The implementation of the Lucas-Kanade algorithm utilizes the same sparseness properties as the implementation of the inverse compositional algorithm. Thus, the algorithms perform similar memory



(a) Coarser level.



(b) Finer level.

Figure 10.4: Plot of the warfield estimated on a coarse image level and the corresponding field in a finer level.

	Iterations	Final Error	Speed [sec.]
Lucas-Kanade (mean \pm std.)	160 \pm 29	$(7.6 \pm 4.1) \cdot 10^{11}$	436 \pm 128
Inverse Compositional (mean \pm std.)	140 \pm 15	$(7.5 \pm 4.0) \cdot 10^{11}$	222 \pm 45
Mean improvement with IC (%)	13	2	49
Paired T-test for difference in mean, 1=mean values are sign. diff.	1 ($p < 0.006$)	0	1 ($p < 10^{-3}$)

Table 10.1: Comparison between the Lucas-Kanade algorithm and the inverse compositional algorithm based on 20 registrations.

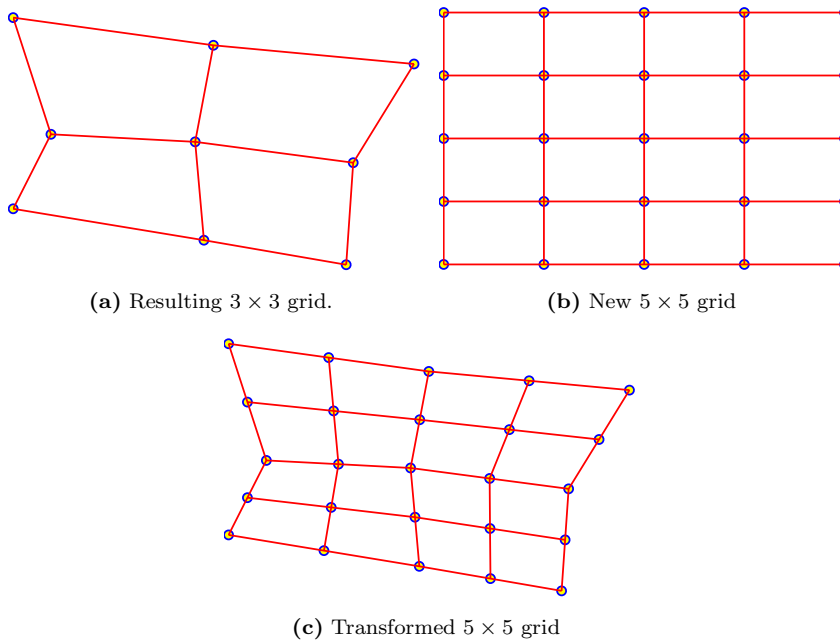


Figure 10.5: Composition of grids of different sizes.

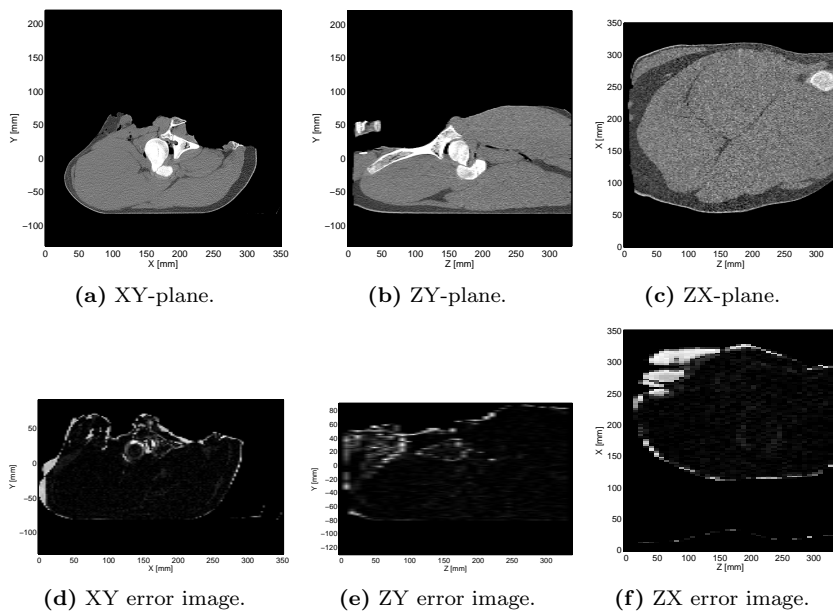


Figure 10.6: (a)-(c): CT-volume of a porcine carcass. (d)-(f): Error images.

wise. The speed increase of the inverse compositional algorithm is due to the pre-computation of the Hessian and the target image gradient. In the paper[41] by Cootes *et al.* the optimization is done by a simple gradient descent scheme. The gradient is computed by displacement of each of the grid nodes in turn. Early experiments have shown this approach to be very slow, so no comparison is made. However, no space is required for pre-computation, and as such it performs well memory wise.

10.3.2 Adding Constraints

If some prior knowledge is at hand before registration or if there is a need for guiding the registration, adding constraints in the optimization scheme should be considered. As an example 58 landmark constraints are applied in a 2D affine warp of image I in figure 10.7(a) to image T in figure 10.7(b). The warp $\mathbf{W}(\mathbf{x}, \mathbf{p})$ of a pixel \mathbf{x} is defined by 6 parameters in vector \mathbf{p}

$$\mathbf{W}(\mathbf{x}, \mathbf{p}) = \begin{pmatrix} 1 + p_1 & p_3 & p_5 \\ p_2 & 1 + p_4 & p_6 \end{pmatrix} \begin{pmatrix} x \\ y \\ 1 \end{pmatrix}. \quad (10.27)$$

The first order term in linearizing the additive update is

$$\frac{\partial \mathbf{p}'}{\partial \Delta \mathbf{p}} = - \begin{pmatrix} 1 + p_1 & p_3 & 0 & 0 & 0 & 0 \\ p_2 & 1 + p_4 & 0 & 0 & 0 & 0 \\ 0 & 0 & 1 + p_1 & p_3 & 0 & 0 \\ 0 & 0 & p_2 & 1 + p_4 & 0 & 0 \\ 0 & 0 & 0 & 0 & 1 + p_1 & p_3 \\ 0 & 0 & 0 & 0 & p_2 & 1 + p_4 \end{pmatrix}. \quad (10.28)$$

The error function of the prior part is defined as

$$C_i = (Lm_{T,i} - \mathbf{W}(Lm_{I,i}; \mathbf{p})), \quad (10.29)$$

where $Lm_{T,i}$ is the i^{th} landmark in the target image T and $Lm_{I,i}$ is the i^{th} landmark in the input image I . The Jacobian of C_i then is

$$\frac{\partial C_i}{\partial \mathbf{p}} = - \begin{pmatrix} Lm_{I,i,x} & 0 & Lm_{I,i,y} & 0 & 1 & 0 \\ 0 & Lm_{I,i,x} & 0 & Lm_{I,i,y} & 0 & 1 \end{pmatrix}, \quad (10.30)$$

where $Lm_{I,i,x}$ and $Lm_{I,i,y}$ are the x- and y-coordinates, respectively, of the i^{th} landmark in I .

Figure 10.8 shows the L2-norm of the intensity and prior error as α_{Rel} is increased. $\alpha_{Rel}=0$ corresponds to no constraints and $\alpha_{Rel}=1$ corresponds to the

intensity and the constraints being weighted equally. The constraints improve the registration as long as the intensity error is decreasing, i.e. for α -values approximately between 0.8 and 1.6. The prior error will of course decrease with increasing α -value. How much weight to put on the constraints depends on the application but for this example weighting intensity and prior more or less equal gives the best result. Figures 10.7(c)-10.7(e) show the difference between the input image I and the target image T warped into the coordinate frame of I , for $\alpha_{Rel}=0, 1$ and 2 . The improvement in registration without constraints compared to the registration with the intensity and constraints weighted equally is obvious, especially in the area around the jaw.

Applying similar constraints as described in section 10.2.4 to the nonrigid case or in 3D is straightforward, all you need to do is to define C_i and compute the Jacobian and $\partial \mathbf{p}' / \partial \Delta \mathbf{p}$.

10.4 Conclusion

This paper has presented an algorithm for registration of 3D images. Registration is done using grid-based warps in a coarse-to-fine manner, enabling the registration of even fine structures in the images while still being diffeomorphic. Using the inverse compositional framework for optimization, the algorithm performs very fast. Exploitation of the sparseness of the grid-based warps and the properties of the interpolating kernel, enables the pre-computation of the Hessian and the target image gradient. The algorithm has a two-fold increase in speed compared to the Lucas-Kanade based algorithm.

Acknowledgements

The 2D images are part of the DTU Face Database [149] and the CT data was provided by the Danish Meat Research Institute as a part of the project "The Virtual Butcher" funded by the Danish Pig Levy Fund and the Directorate for Food, Fisheries and Agri Business. The authors would also like to thank the IMM ITMAN graduate school at the Technical University of Denmark for support.

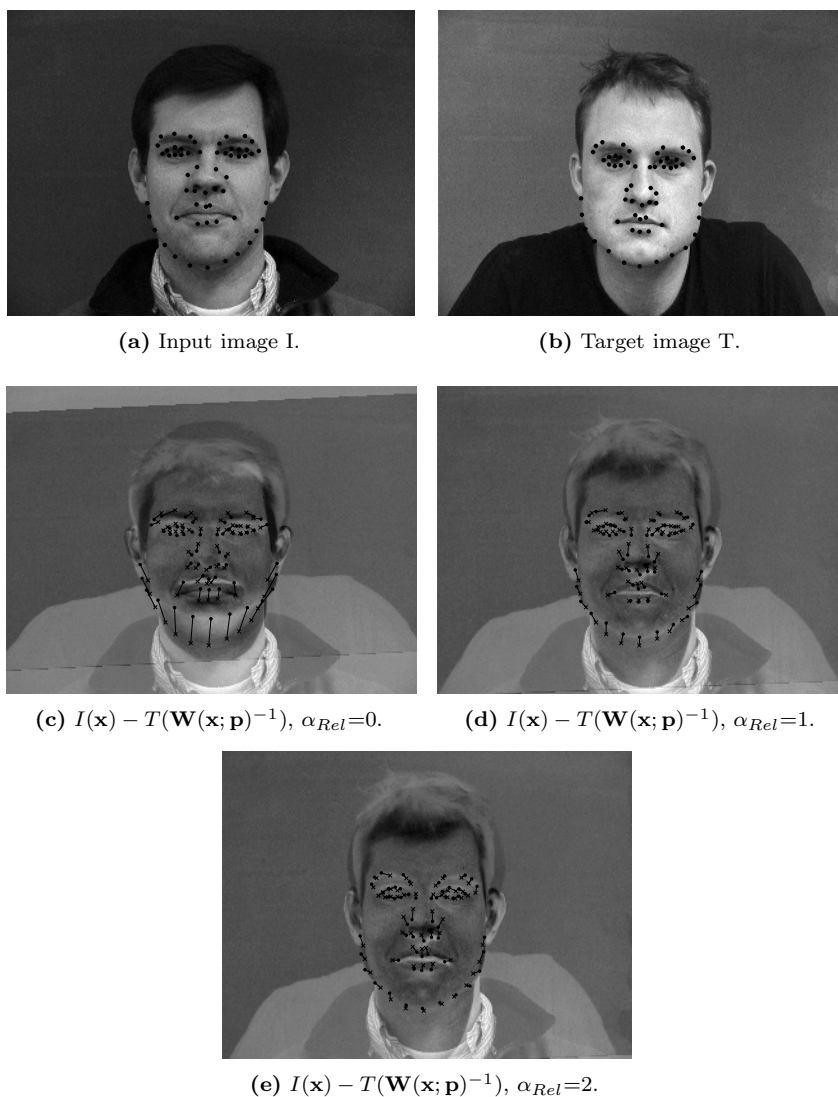


Figure 10.7: 2D affine registration of 2 images with increasing weight on landmark constraints.

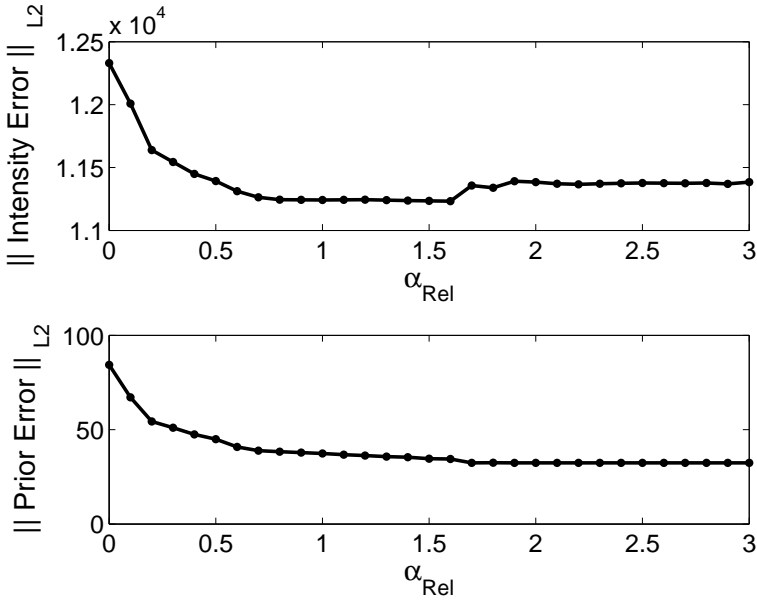


Figure 10.8: Intensity and prior errors vs. α_{Rel} .

Software

Søren G. H. Erbou

11.1 SSM Explorer

SSM Explorer is a simple application for visualization and exploration of statistical shape models and stl-files. It is written in **C#** using **VTK** and shape models can be exported from **Matlab**. Different types of models can be visualized, e.g. PCA based and Varimax rotated models. Sliders make it possible to adjust each mode of variation. Figure 11.1 shows a screen-dump of SSM Explorer.

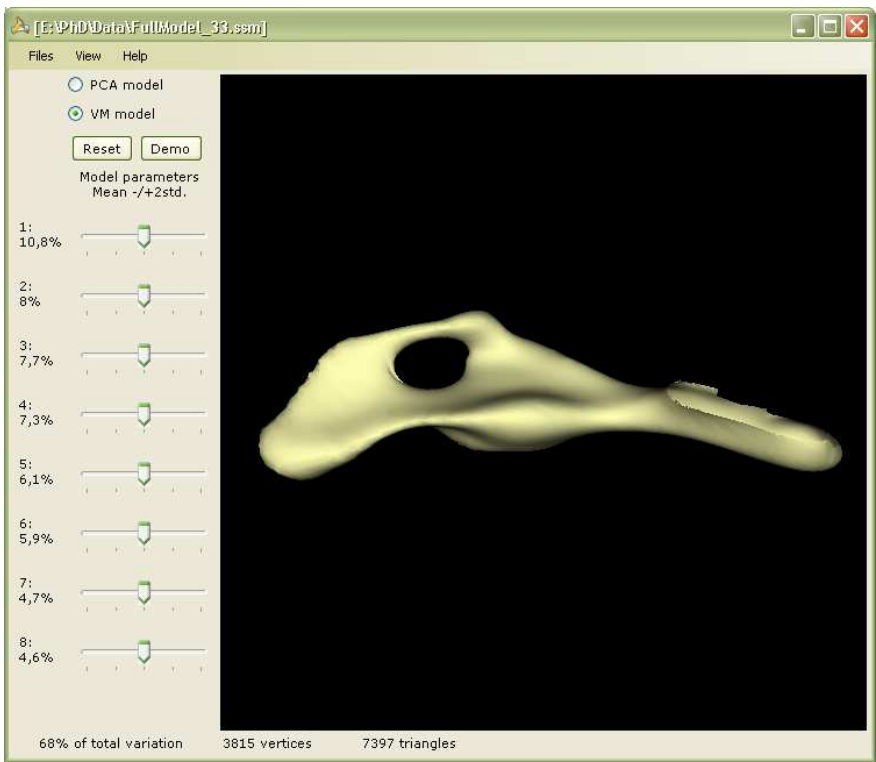


Figure 11.1: SSM Explorer. Software for visualization of statistical shape models and stl-files.

List of Figures

2.1	Modern abattoir. Part A - sedation, killing and cleaning. Part B - removal of organs, inspection and grading. Part C - Chilling and major cuts. Courtesy of DMA.	12
2.2	Various automated processes in a modern abattoir (Courtesy of DMA).	13
2.3	Bone structure in the ham of a pig carcass.	14
2.4	Measuring fat thickness using ultrasound. The shadows in (b) are due to two ribs which reflect most of the signal. (Courtesy of DMA).	15
2.5	Pork loin (Courtesy of DMA).	16
2.6	X-ray Computed Tomography (Courtesy of W. A. Kalender [94]).	19
2.7	CT topogram.	21
4.1	Left side of a carcass prepared and ready for scanning (Courtesy of DMRI).	34
4.2	(a) CT estimated weight versus measured weight. (b) LMP estimated by manual dissection versus CT estimated LMP.	35

4.3	(a) & (b) Mean shape seen from two different views. (c) PCA based PDM. Left and right columns are perturbed $-3/+3$ std. from the mean shape. Rows are modes 1-8. The colors show the distance to the mean surface, from blue through red (0-3mm). . .	36
4.4	5 shape models are compared. (a) PCA, (b) Varimax, (c) Threshold PCA, (d) Threshold Varimax, (e) Sparse PCA. Left and right columns for each model are perturbed $-3/+3$ std., respectively, from the mean shape. Rows are modes 1-8. The color coding shows the distance to the mean surface, from blue through red ($> 0 \rightarrow 3\text{mm}$). Zero distance is denoted gray. A sparsity level of 30% non-zero loadings is chosen for the three sparse models. . . .	38
4.5	Difference between estimated and true parameter values for the three optimization schemes.	40
4.6	2D affine registration of 2 images with and without landmark constraints.	42
6.1	Histogram of a CT-volume of a pig carcass. The ordinate is scaled to show the distribution of fat (left) and meat voxels (right). . .	51
6.2	Left side of a carcass prepared and ready for scanning.	53
6.3	Partial volume effects shown in a CT-slice from the shoulder part of half a pig carcass. Yellow denotes voxels with a probability above 0.5 and below 1.0 of belonging to the meat class.	54
6.4	The resulting LMP estimated by CT, 299 carcasses (left), and by manual dissection, 29 carcasses (right), sorted by LMP.	55
6.5	LMP estimated by manual dissection versus CT-estimated LMP using the MAP model.	57
6.6	Estimated weight using the MAP model versus measured weight.	58
6.7	Estimated parameters and their corresponding 95% confidence intervals for the two models, with and without a constant term c	59
7.1	(a) shows a CT slice with the bone contour segmented (red). (b) shows an image of the bone structure in the ham of a pig carcass and (c) shows the segmented contour points for the hind part of a carcass with the estimated surface of the pelvic bone structure.	71

7.2	Triangulated surfaces of a small part of two bones. Black lines denote correspondence between vertices in the dark gray bone, and the surface of the light gray bone along the estimated mean curvature normal.	73
7.3	Mean shape seen from two different views.	73
7.4	Plots of distances between vertices of the mean shape and the surface of each of the other shapes. Shape no. 8 is used as initial reference. Boxes denote lower quartile, median and upper quartile. The horizontal green line denotes the overall mean of the distances for each shape, which is $1.13 \pm 0.18\text{mm}$ (mean \pm std). The black line denotes the overall median (0.92mm).	74
7.5	Model selection. Parallel Analysis (upper 95% CI) suggests to keep 8 modes of the original PCA, describing 67.0% of the total variation in the data.	75
7.6	Scatter plots of the surfaces projected onto combinations of PCA modes. The blue triangles denote the original reference shape (no. 6) and the red squares show a shape (no. 22) is an extreme in mode 5, but not in the other modes. The green diamonds denote shape no. 10 which has the largest absolute value of mode 1. The black circles are iso-contours of 1, 2 and 3 std. of each parameter.	76
7.7	PCA based PDM. Left and right columns are perturbed $-3/+3$ std. from the mean shape. Rows are modes 1-8, cf. table 7.1. The color coding shows the distance to the mean surface, from blue through red (0-3mm).	78
7.8	Surfaces 1-15	80
7.9	Surfaces 16-33	81
8.1	For a specific LOO model, the total adjusted variance explained is plotted (left) as a function of the percentage of non-zero loadings, with eight modes included in all five models. In the right figure the adjusted variance explained by each mode is plotted for a sparsity level of 30% non-zero loadings for the three sparse models.	92
8.2	Reconstruction error. The top row shows the mean rms error as a function of the percentage of non-zero loadings (note the scaling of the axes). The bottom row shows std. of the rms error. The left column shows the results with only one mode included and the right column shows results with eight modes included.	94

8.3 PCA model. Left and right column is perturbed $-3/+3$ std., respectively, from the mean shape. Rows are modes 1-8, cf. figure 8.1. The color coding shows the distance to the mean surface, from blue through red ($> 0 \rightarrow 3\text{mm}$). Zero distance is denoted gray. 96

8.4 Varimax model. Left and right column is perturbed $-3/+3$ std., respectively, from the mean shape. Rows are modes 1-8, cf. figure 8.1. The color coding shows the distance to the mean surface, from blue through red ($> 0 \rightarrow 3\text{mm}$). Zero distance is denoted gray. 97

8.5 Threshold PCA model. Left and right columns for each model are perturbed $-3/+3$ std., respectively, from the mean shape. Rows are modes 1-8, cf. figure 8.1. The color coding shows the distance to the mean surface, from blue through red ($> 0 \rightarrow 3\text{mm}$). Zero distance is denoted gray. 98

8.6 Threshold Varimax model. Left and right columns for each model are perturbed $-3/+3$ std., respectively, from the mean shape. Rows are modes 1-8, cf. figure 8.1. The color coding shows the distance to the mean surface, from blue through red ($> 0 \rightarrow 3\text{mm}$). Zero distance is denoted gray. A sparsity level of 30% non-zero loadings is chosen. 99

8.7 SPCA model. Left and right columns for each model are perturbed $-3/+3$ std., respectively, from the mean shape. Rows are modes 1-8, cf. figure 8.1. The color coding shows the distance to the mean surface, from blue through red ($> 0 \rightarrow 3\text{mm}$). Zero distance is denoted gray. A sparsity level of 30% non-zero loadings is chosen. 100

8.8 Spatial error distribution [mm]. (a) rms error distribution using PCA model. (b) difference in rms error distribution between, from the top down, VM / Th. PCA / Th. VM / SPCA and PCA respectively. Negative differences (bluish) denote smaller rms errors, and positive differences (reddish) denote larger rms errors, than the PCA model. 102

9.1 Three principal modes of variation (rows) cover 25%, 12% and 8% respectively of the total variation in the data. Left and right columns denote -3 and $+3$ std. from the mean shape (middle column). The color coding indicates the absolute distance in mm to the mean shape. 111

9.2	Difference between estimated and true parameter values for the three optimization schemes.	112
9.3	Mean rms error of leave-one-out validation for different number of modes included, the std. is 0.12 mm. The mean value of the initial rms error is 1.85 mm.	113
9.4	Mean (a) and std. (b) of rms error, in mm, for each point plotted on the mean shape and reconstructed using 3 modes. The mean rms error on the surface is 1.50 mm. and the mean of the std. is 0.59 mm.	114
10.1	The displacement of a pixel is governed by the displacement of its surrounding grid nodes [149].	120
10.2	The derivative of the warp with respect to the node in the lower left corner. It is non-zero only in the region bounded by the neighboring nodes.	125
10.3	Plot of non-zero elements in Hessian matrices, for grid sizes of $3 \times 3 \times 3$, $5 \times 5 \times 5$ and $9 \times 9 \times 9$	127
10.4	Plot of the warpfield estimated on a coarse image level and the corresponding field in a finer level.	129
10.5	Composition of grids of different sizes.	130
10.6	(a)-(c): CT-volume of a porcine carcass. (d)-(f): Error images.	130
10.7	2D affine registration of 2 images with increasing weight on landmark constraints.	133
10.8	Intensity and prior errors vs. α_{Rel}	134
11.1	SSM Explorer. Software for visualization of statistical shape models and stl-files.	136

List of Tables

6.1	Previous work. Papers [46], [31], [133] and [89] apply PLSR-methods on histograms for meat pixels, modeling the lean meat weight obtained from dissection. [105] apply a contextual Bayesian classifier and linear regression for predicting the full weight of half carcasses. R^2 is the explained variance, RMSEP/C are the rms errors of prediction/calibration, with the corresponding bias reported in some cases.	52
6.2	Mean and standard deviations of the residuals obtained by comparing CT-dissection with manual dissection.	56
6.3	Predictive performance of the two models, with and without a constant term c , using leave-one-out cross-validation.	56
6.4	The resulting parameters for the MAP and PVE models excluding and including a constant term c . 95% confidence intervals are shown in brackets.	60
7.1	Variance explained by each mode in the PCA model. 8 modes explain 67.0% of the total variation.	75
8.1	For a specific LOO model, the total adjusted variance explained is shown for each of the five models, along with the mean and std. of the rms error for all LOO models. Eight modes of variation are included and a sparsity of 30% non-zero loadings is chosen for the three sparse models.	92

8.2 Paired t test of the difference in adjusted variance explained being zero (H_0) at a 0.1% significance level. 1 denotes H_0 -reject, i.e. the adjusted variance explained is significantly different for each pair of models. A sparsity level of 30% non-zero loadings is chosen for the three sparse models. 93

8.3 Paired t test of the mean difference in spatial rms error being zero (H_0) at a 0.1% significance level. 1 denotes H_0 -reject, i.e. the difference in rms error is different from zero, with the model in the row having smaller spatial rms error than the model in the column. 101

9.1 Difference between estimated and true parameter values for the three schemes when estimating 1 through 7 modes. Mean and (std.) are reported. 113

10.1 Comparison between the Lucas-Kanade algorithm and the inverse compositional algorithm based on 20 registrations. 129

Bibliography

- [1] H. Akaike. Information theory and an extension of the maximum likelihood principle. In *2nd Int. Symposium on Information Theory*, pages 267–281, 1973.
- [2] D. Alcantara, O. Carmichael, E. Delson, W. Harcourt-Smith, K. Sterner, S. Frost, R. Dutton, P. Thompson, H. Aizenstein, O. Lopez, J. Becker, and N. Amenta. Localized components analysis. In *Information Processing in Medical Imaging (IPMI)*, pages 519–531, 2007.
- [3] P. Allen and O. Vangen. X-ray tomography of pigs: some preliminary results. In *In Vivo Measurement of Body Composition in Meat Animals*, pages 52–66, 1984.
- [4] N. Amenta, S. Choi, and R. K. Kolluri. The power crust, unions of balls, and the medial axis transform. *Computational Geometry*, 19(2):127–153, 2001.
- [5] P. R. Andresen. *Surface-bounded growth modeling applied to human mandibles*. PhD thesis, Informatics and Mathematical Modelling, Technical University of Denmark, 1999.
- [6] P. R. Andresen and M. Nielsen. Non-rigid Registration by Geometry-Constrained Diffusion. *Medical Image Analysis*, 5(2):81–88, 2001.
- [7] P. R. Andresen and M. Nielsen. Non-rigid Registration by Geometry-Constrained Diffusion. In *Medical Image Computing and Computer-Assisted Intervention (MICCAI)*, volume 1679, pages 533–543, 1999.
- [8] P. R. Andresen, F. L. Bookstein, K. Conradsen, B. K. Ersbøll, J. Marsh, and S. Kreiborg. Surface-bounded growth modeling applied to human mandibles. *IEEE Transactions on Medical Imaging*, 19(11):1053–1063, 2000.

- [9] J. Ashburner, C. Hutton, R. Frackowiak, I. Johnsrude, C. Price, and K. Friston. Identifying Global Anatomical Differences: Deformation-Based Morphometry. *Human Brain Mapping*, 6:348–357, 1998.
- [10] M. A. Audette, F. P. Ferrie, and T. M. Peters. An Algorithmic Overview of Surface Registration Techniques for Medical Imaging. *Medical Image Analysis*, 4(3):201–217, 2000.
- [11] R. Bajcsy and S. Kovačič. Multiresolution elastic matching. *Computer Vision, Graphics, and Image Processing*, 46(1):1–21, 1989.
- [12] S. Baker and I. Matthews. Lucas-Kanade 20 Years On: A Unifying Framework. *Int. Journal of Computer Vision*, 56(3):221–255, 2004.
- [13] S. Baker, R. Gross, and I. Matthews. Lucas-Kanade 20 Years On: A Unifying Framework: Part 4. Technical report, Robotics Institute, Carnegie Mellon University, 2004.
- [14] U. Baulain. Magnetic resonance imaging for the in vivo determination of body composition in animal science. *Computers and Electronics in Agriculture*, 17(2):189–203, 1997.
- [15] P. J. Besl and N. D. McKay. A Method for Registration of 3-D Shapes. *IEEE Transactions on Pattern Analysis and Machine Intelligence*, 14(2):239–256, 1992.
- [16] H. Blum. A transformation for extracting new descriptors of shape. *Models for the Perception of Speech and Visual Form*, pages 36–380, 1967.
- [17] F. L. Bookstein. Principal warps: Thin-Plate Splines and the Decomposition of Deformations. *IEEE Transactions on Pattern Analysis and Machine Intelligence*, 11(6):567–585, 1989.
- [18] F. L. Bookstein. Shape and the Information in Medical Images: A Decade of the Morphometric Synthesis. *Computer Vision and Image Understanding*, 66(2):97–118, 1997.
- [19] F. L. Bookstein. Landmark methods for forms without landmarks: morphometrics of group differences in outline shape. *Medical Image Analysis*, 1(3):225–243, 1997.
- [20] C. Brechbühler, G. Gerig, and O. Kuebler. Parametrization of Closed Surfaces for 3-D Shape Description. *Computer Vision and Image Understanding*, 61:154–154, 1995.
- [21] M. Bro-Nielsen. *Medical Image Registration and Surgery Simulation*. PhD thesis, Informatics and Mathematical Modelling, Technical University of Denmark, 1996.
- [22] M. Bro-Nielsen and C. Gramkow. Fast fluid registration of medical images. In *Visualization in Biomedical Computing (VBC)*, pages 267–276, 1996.
- [23] C. Broit. *Optimal registration of deformed images*. PhD thesis, University of Pennsylvania, 1981.

- [24] H. Busk, E. V. Olsen, and J. Brøndum. Determination of lean meat in pig carcasses with the Autofom classification system. *Meat Science*, 52(3): 307–314, 1999.
- [25] J. Cadima and I. T. Jolliffe. Loading and correlations in the interpretation of principle components. *Journal of Applied Statistics*, 22(2):203–214, 1995.
- [26] J. C. Carr, R. K. Beatson, J. B. Cherrie, T. J. Mitchell, W. R. Fright, B. C. McCallum, and T. R. Evans. Reconstruction and representation of 3D objects with radial basis functions. In *Computer Graphics Proceedings (SIGGRAPH)*, pages 67–76, 2001.
- [27] Y. Chen and G. Medioni. Object modeling by registration of multiple range images. *IEEE Conf. on Robotics and Automation*, 3:2724–2729, 1991.
- [28] Z. Cho, J. P. Jones, and M. Singh. *Foundations of Medical Imaging*. John Wiley & Sons, Inc., 1993.
- [29] G. E. Christensen. *Deformable Shape Models for Anatomy*. PhD thesis, Washington University, 1994.
- [30] L. B. Christensen, M. Vester-Christensen, C. Borggaard, and E. V. Olsen. Robustness of weight and meat content in pigs determined by CT. In *54th Int. Congress of Meat Science and Technology (ICoMST)*, 2008.
- [31] G. Collewet, P. Bogner, P. Allen, H. Busk, A. Dobrowolski, E. Olsen, and A. Davenel. Determination of the lean meat percentage of pig carcasses using magnetic resonance imaging. *Meat Science*, 70:563–572, 2005.
- [32] Commission of the European Communities (EC). EC regulation no. 3127/94 amending regulation (EC) no. 2967/85 laying down detailed rules for the application of the community scale for grading pig carcasses. ECOJ Nr L330, 43, 1994.
- [33] P. Comon. Independent component analysis, A new concept? *Signal Processing*, 36(3):287–314, 1994.
- [34] T. F. Cootes and C. J. Taylor. Statistical Models of Appearance for Computer Vision. Technical report, University of Manchester, 2004. URL www.isbe.man.ac.uk/~bim/Models/app_models.pdf.
- [35] T. F. Cootes and C. J. Taylor. Active Shape Models - Smart Snakes. In *British Machine Vision Conference (BMVC)*, pages 266–275, 1992.
- [36] T. F. Cootes, C. J. Taylor, D. H. Cooper, and J. Graham. Training Models of Shape from Sets of Examples. In *British Machine Vision Conference (BMVC)*, pages 9–18, 1992.
- [37] T. F. Cootes, C. J. Taylor, D. H. Cooper, and J. Graham. Active Shape Models - their Training and Application. *Computer Vision and Image Understanding*, 61(1):38–59, 1995.

- [38] T. F. Cootes, G. J. Edwards, and C. J. Taylor. Active Appearance Models. *IEEE Trans. on Pattern Recognition and Machine Intelligence*, 23(6):681–685, 2001.
- [39] T. F. Cootes, C. J. Twining, K. O. Babalola, and C. J. Taylor. Diffeomorphic statistical shape models. *Image and Vision Computing*, 26(3): 326–332, 2008.
- [40] T.F. Cootes, S. Marsland, C.J. Twining, K. Smith, and C.J. Taylor. Groupwise Diffeomorphic Non-rigid Registration for Automatic Model Building. In *European Conference on Computer Vision (ECCE)*, pages Vol IV: 316–327, 2004.
- [41] T.F. Cootes, C.J. Twining, and C.J. Taylor. Diffeomorphic Statistical Shape Models. In *British Machine Vision Conference (BMVC)*, pages 447–456, 2004.
- [42] S. Darkner, M. Vester-Christensen, R. R. Paulsen, and R. Larsen. Non-rigid surface registration of 2D manifolds in 3D euclidian space. In *SPIE Int. Symposium on Medical Imaging*, volume 6914, (69142R), 2008.
- [43] R. H. Davies, C. J. Twining, T. F. Cootes, J. C. Waterton, and C. J. Taylor. 3D statistical shape models using direct optimisation of description length. In *European Conference on Computer Vision (ECCE)*, pages 3–20, 2002.
- [44] R. H. Davies, C. J. Twining, T. F. Cootes, J. C. Waterton, and C. J. Taylor. A minimum description length approach to statistical shape modeling. *IEEE Transactions on Medical Imaging*, 21(5):525–537, 2002.
- [45] M. Desbrun, M. M., P. Schröder, and A. H. Barr. Implicit fairing of irregular meshes using diffusion and curvature flow. In *Computer Graphics Proceedings (SIGGRAPH)*, pages 317–324, 1999.
- [46] A. Dobrowolski, W. Branscheid, R. Romvári, P. Horn, and P. Allen. X-ray computed tomography as possible reference for the pig carcass evaluation. *Fleischwirtschaft*, 84(3):109–112, 2004.
- [47] I. L. Dryden and K. V. Mardia. *Statistical Shape Analysis*. John Wiley & Sons, 1998.
- [48] S. G. Erbou. 3D Statistical Shape Model of Bones. In *Image Analysis and In-Vivo Pharmacology (IAVP)*, 2007.
- [49] S. G. Erbou, H. B. D. Sørensen, and B. Stage. Detection of Cast Shadows in Surveillance Applications. In *Den 14. Danske Konference i Mønstergenkendelse og Billedanalyse (DSAGM)*, pages 10–19, 2005.
- [50] S. G. Erbou, R. Larsen, and B. K. Ersbøll. Registration and Shape Modelling of Porcine Bone Structures via CT. In *21st Nordic Conference on Mathematical Statistics (NordStat)*, 2006.

- [51] S. G. Erbou, M. Vester-Christensen, R. Larsen, E. V. Olsen, and B. K. Ersbøll. Quantifying Biological Variation. In *European Congress of Chemical Engineering - 6 (ECCE6), Special Symposium - Innovations in Food Technology*, 2007.
- [52] S. G. H. Erbou and B. K. Ersbøll. From CT to Shape Model. Technical report, DTU Informatics, Technical University of Denmark, 2008.
- [53] S. G. H. Erbou, S. Darkner, J. Fripp, S. Ourselin, and B. K. Ersbøll. Estimation of Shape Model Parameters for 3D Surfaces. In *IEEE 5th Int. Symposium on Biomedical Imaging (ISBI)*, pages 624–627, 2008.
- [54] S. G. H. Erbou, M. Vester-Christensen, L. B. Christensen, R. Larsen, and B. K. Ersbøll. Comparison of Sparse Point Distribution Models. *Machine Vision and Applications*, 2009. doi: 0.1007/s00138-009-0203-1.
- [55] EUPIGCLASS. Fifth framework programme of the European Community for research, technological development and demonstration activities, 2003. URL www.eupigclass.net.
- [56] P. T. Fletcher, S. Joshi, C. Lu, and S. M. Pizer. Gaussian Distributions on Lie Groups and Their Application to Statistical Shape Analysis. In *Information Processing in Medical Imaging (IPMI)*, pages 450–462, 2003.
- [57] P. T. Fletcher, C. Lu, and S. Joshi. Statistics of Shape via Principal Geodesic Analysis on Lie Groups. In *Computer Vision and Pattern Recognition (CVPR)*, volume 1, pages 95–101, 2003.
- [58] P. T. Fletcher, C. Lu, S. M. Pizer, and S. Joshi. Principal Geodesic Analysis for the Study of Nonlinear Statistics of Shape. *IEEE Transactions on Medical Imaging*, 23(8):995–1005, 2004.
- [59] M. Fleute and S. Lavallée. Building a Complete Surface Model from Sparse Data Using Statistical Shape Models: Application to Computer Assisted Knee Surgery System. In *Medical Image Computing and Computer-Assisted Intervention (MICCAI)*, pages 879–887, 1998.
- [60] M. Fleute and S. Lavallée. Nonrigid 3-D/2-D Registration of Images Using Statistical Models. In *Medical Image Computing and Computer-Assisted Intervention (MICCAI)*, pages 138–147, 1999.
- [61] J. Fripp, S. Crozier, S. K. Warfield, and S. Ourselin. Automatic segmentation of the bone and extraction of the bone-cartilage interface from magnetic resonance images of the knee. *Physics in Medicine and Biology*, 52(6):1617–1631, 2007.
- [62] G. Gerig, M. Styner, D. Jones, D. Weinberger, and J. Lieberman. Shape analysis of brain ventricles using SPHARM. *Mathematical Methods in Biomedical Image Analysis (MMBIA)*, pages 171–178, 2001.
- [63] C. A. Glasbey and K. V. Mardia. A review of image-warping methods. *Journal of Applied Statistics*, 25(2):155–171, 1998.

- [64] C. A. Glasbey and C. D. Robinson. Estimators of tissue proportions from X-ray CT images. *Biometrics*, 58:928–936, 2002.
- [65] P. Golland, W. E. L. Crimson, and R. Kikinis. Statistical Shape Analysis Using Fixed Topology Skeletons: Corpus Callosum Study. In *Information Processing in Medical Imaging (IPMI)*, pages 382–387, 1999.
- [66] P. Golland, W. E. L. Grimson, M. E. Shenton, and R. Kikinis. Small sample size learning for shape analysis of anatomical structures. In *Medical Image Computing and Computer-Assisted Intervention (MICCAI)*, volume 1935, pages 72–82, 2000.
- [67] P. Golland, W. E. L. Grimson, M. E. Shenton, and R. Kikinis. Deformation Analysis for Shape Based Classification. In *Information Processing in Medical Imaging (IPMI)*, pages 517–530, 2001.
- [68] P. Golland, W. E. L. Grimson, M. E. Shenton, and R. Kikinis. Detection and analysis of statistical differences in anatomical shape. *Medical Image Analysis*, 9(1):69–86, 2005.
- [69] G. H. Golub and C. F. Van Loan. *Matrix Computations*. Johns Hopkins Press, 2nd edition, 1989.
- [70] R. C. Gonzalez and R. E. Woods. *Digital Image Processing*. Prentice Hall, 2nd edition, 2002.
- [71] C. Goodall. Procrustes Methods in the Statistical Analysis of Shape. *Journal of the Royal Statistical Society. Series B. Methodological*, 53(2): 285–339, 1991.
- [72] J. C. Gower. Generalized Procrustes analysis. *Psychometrika*, 40:33–50, 1975.
- [73] A. Guimond, J. Meunier, and J. Thirion. Average brain models: A convergence study. *Computer Vision and Image Understanding*, 77(2):192–210, 2000.
- [74] M. F. Hansen. Quality Estimation and Segmentation of Pig Backs. Master’s thesis, Informatics and Mathematical Modelling, Technical University of Denmark, 2005.
- [75] M. F. Hansen, R. Larsen, B. Ersbøll, and L. B. Christensen. Coupled Shape Model Segmentation in Pig Carcasses. In *IEEE International Conference on Pattern Recognition ICPR*, 2006.
- [76] M. F. Hansen, S. Erbou, M. Vester-Christensen, R. Larsen, B. Ersbøll, and L. B. Christensen. Surface-to-Surface Registration Using Level Sets. In *Scandinavian Conference on Image Analysis (SCIA)*, pages 780–788, 2007.
- [77] J. C. Hayton, D. G. Allen, and V. Scarpello. Factor retention decisions in exploratory factor analysis: A tutorial on parallel analysis. *Organizational Research Methods*, 7(2):191–205, 2004.

- [78] T. Heimann, I. Wolf, T. Williams, and H. P. Meinzer. 3D active shape models using gradient descent optimization of description length. In *Information Processing in Medical Imaging (IPMI)*, pages 566–577, 2005.
- [79] T. Heimann, I. Wolf, and H. P. Meinzer. Optimal Landmark Distributions for Statistical Shape Model. In *SPIE Int. Symposium on Medical Imaging*, volume 6144, page 61441J, 2006.
- [80] P. W. Holland and R. E. Welsch. Robust regression using iteratively reweighted least-squares. *Communications in Statistics - Theory and Methods*, 6(9):813 – 827, 1977.
- [81] P. Horkaew and G. Z. Yang. Optimal Deformable Surface Models for 3D Medical Image Analysis. In *Information Processing in Medical Imaging (IPMI)*, pages 13–24, 2003.
- [82] P. Horkaew and G. Z. Yang. Construction of 3D Dynamic Statistical Deformable Models for Complex Topological Shapes. In *Medical Image Computing and Computer-Assisted Intervention (MICCAI)*, pages 217–224, 2004.
- [83] J. L. Horn. A rationale and test for the number of factors in factor analysis. *Psychometrika*, 30:179–185, 1965.
- [84] H. Huang, L. Shen, R. Zhang, F. Makedon, A. Saykin, and J. Pearlman. A Novel Surface Registration Algorithm With Biomedical Modeling Applications. *IEEE Transactions on Information Technology in Biomedicine*, 11(4):474–482, 2007.
- [85] A. Hyrvärinen. Survey on independent component analysis. *Neural Computing Surveys*, 2:94–128, 1999.
- [86] Danish Meat Research Institute. Udvikling af ”den virtuelle slagter” (in Danish). Technical report, Danish Meat Research Institute, 2005.
- [87] J. E. Jackson. *A User’s Guide to Principal Components*. John Wiley & Sons, Inc., 1991.
- [88] J. A. Jensen. *Estimation of Blood Velocities Using Ultrasound: A Signal Processing Approach*. Cambridge University Press, New York, 1996.
- [89] J. Johansen, B. Egelanddal, M. Røe, K. Kvaal, and A. H. Aastveit. Calibration models for lamb carcass composition analysis using computerized tomography (CT) imaging. *Chemometrics and Intelligent Laboratory Systems*, 87(2):303–311, 2007.
- [90] S. J. Jones, A. Guru, V. Singh, , and T. F. Jones. Porcine Myology, 2006. URL <http://porcine.unl.edu>.
- [91] S. Joshi, S. Pizer, P. T. Fletcher, P. Yushkevich, A. Thall, and J. S. Marron. Multiscale Deformable Model Segmentation and Statistical Shape Analysis Using Medial Descriptions. *IEEE Transactions on Medical Imaging*, 21(5):538–550, 2002.

- [92] A. Junkuszew and F. Ringdorfer. Computer tomography and ultrasound measurement as methods for the prediction of the body composition of lambs. *Small Ruminant Research*, 56(1-3):121–125, 2005.
- [93] H. F. Kaiser. The varimax criterion for analytic rotation in factor analysis. *Psychometrika*, 23:187–200, 1958.
- [94] W. A. Kalender. *Computed Tomography*. Publicis MCD Verlag, Munich, 2000.
- [95] R. A. Katz and S. M. Pizer. Untangling the Blum Medial Axis Transform. *International Journal of Computer Vision*, 55(2):139–153, 2003.
- [96] N. C. Kjærsgaard. *Optimization of the Raw Material Use at Danish Slaughterhouses*. PhD thesis, DTU informatics, Technical University of Denmark, 2008.
- [97] J. Kongsro, M. Røe, A. H. Aastveit, K. Kvaal, and B. Egelanddsdal. Virtual dissection of lamb carcasses using computer tomography (CT) and its correlation to manual dissection. *Journal of Food Engineering*, 88(1):86–93, 2008.
- [98] J. Kongsro, M. Røe, K. Kvaal, A. H. Aastveit, and B. Egelanddsdal. Prediction of fat, muscle and value in Norwegian lamb carcasses using EUROP classification, carcass shape and length measurements, visible light reflectance and computer tomography (CT). *Meat Science*, 2008. doi: 10.1016/j.meatsci.2008.07.004.
- [99] R. Larsen. 3-D Contextual Bayesian Classifiers. *IEEE Transactions on Image Processing*, 10(3):518–524, 2000.
- [100] R. Larsen and K. B. Hilger. Probabilistic generative modelling. In *13th Scandinavian Conference on Image Analysis (SCIA)*, volume 2749, pages 861–868, 2003.
- [101] S. Lee, G. Wolberg, and S. Y. Shin. Scattered data interpolation with multilevel B-splines. *IEEE Transactions on Visualization and Computer Graphics*, 3(3):228–244, 1997.
- [102] M. E. Leventon, W. E. L. Grimson, and O. Faugeras. Statistical Shape Influence in Geodesic Active Contours. In *Computer Vision and Pattern Recognition (CVPR)*, volume 1, pages 316–323, 2000.
- [103] W. E. Lorensen and H. E. Cline. Marching cubes: A high resolution 3D surface construction algorithm. In *Computer Graphics Proceedings (SIGGRAPH)*, volume 21, pages 163–169, July 1987.
- [104] B. Lucas and T. Kanade. An iterative image registration technique with an application to stereo vision. In *7th Int. Joint Conference on Artificial Intelligence*, pages 674–679, 1981.
- [105] A. Lyckegaard, R. Larsen, L. B. Christensen, M. Vester-Christensen, and E. V. Olsen. Contextual analysis of CT scanned pig carcasses. In *52nd*

- Int. Congress of Meat Science and Technology (ICoMST)*, pages 207–208, 2006.
- [106] M. Lüthi, T. Albrecht, and T. Vetter. Curvature Guided Surface Registration using Level Sets. In *21st Congress on Computer Assisted Radiology and Surgery (CARS)*, 2007.
- [107] M. Lüthi, T. Albrecht, and T. Vetter. A Curvature Sensitive Demon's Algorithm for Surface registration. Technical report, Department of Computer Science, University of Basel, 2007.
- [108] J. B. A. Maintz and M. A. Viergever. A survey of medical image registration. *Medical Image Analysis*, 2(1):1–36, 1998.
- [109] J. Modersitzki. *Numerical Methods for Image Registration*. Numerical Mathematics and Scientific Computation. Oxford University Press, 2004.
- [110] M. Monziols, G. Collewet, F. Mariette, M. Kouba, and A. Davenel. Muscle and fat quantification in MRI gradient echo images using a partial volume detection method. Application to the characterization of pig belly tissue. *Magnetic Resonance Imaging*, 23(6):745–755, 2005.
- [111] M. Monziols, G. Collewet, M. Bonneau, F. Mariette, A. Davenel, and M. Kouba. Quantification of muscle, subcutaneous fat and intermuscular fat in pig carcasses and cuts by magnetic resonance imaging. *Meat Science*, 72(1):146–154, 2006.
- [112] B. S. Morse, T. S. Yoo, P. Rheingans, D. T. Chen, and K. R. Subramanian. Interpolating implicit surfaces from scattered surface data using compactly supported radial basis functions. In *Shape Modelling Int. (SMI)*, pages 89–98, 2001.
- [113] E. A. Navajas, C. A. Glasbey, K. A. McLean, A. V. Fisher, A. J. L. Charteris, N. R. Lambe, L. Bünger, and G. Simm. In vivo measurements of muscle volume by automatic image analysis of spiral computed tomography scans. *Animal Science*, 82(4):545–553, 2007.
- [114] M. Nielsen, P. Johansen, A. Jackson, and B. Lautrup. Brownian warps: A least committed prior for non-rigid registration. In *Medical Image Computing and Computer-Assisted Intervention (MICCAI)*, pages 557–564, 2002.
- [115] M. Nielsen, P. Johansen, A. Jackson, B. Lautrup, and S. Hauberg. Brownian Warps for Non-Rigid Registration. *Journal of Mathematical Imaging and Vision*, pages 221–231, 2008.
- [116] P. M. Nissen, H. Busk, M. Oksama, M. Seynaeve, M. Gispert, P. Walstra, I. Hansson, and E. Olsen. The estimated accuracy of the EU reference dissection method for pig carcass classification. *Meat Science*, 73(1):22–28, 2006.

- [117] H. Ólafsdóttir. *Analysis of Craniofacial Images using Computational Atlases and Deformation Fields*. PhD thesis, Informatics and Mathematical Modelling, Technical University of Denmark, 2007.
- [118] H. Ólafsdóttir, M. S. Hansen, K. Sjöstrand, T. A. Darvann, N. V. Hermann, E. Oubel, B. K. Ersbøll, R. Larsen, A. F. Frangi, P. Larsen, C. A. Perlyn, G. M. Morriss-Kay, and S. Kreiborg. Sparse Statistical Deformation Model for the Analysis of Craniofacial Malformations in the Crouzon Mouse. In *Scandinavian Conference on Image Analysis (SCIA)*, volume 4522, pages 112–121, 2007.
- [119] E. V. Olsen, M. Candek-Potokar, M. Oksama, S. Kien, D. Lisiak, and H. Busk. On-line measurements in pig carcass classification: Repeatability and variation caused by the operator and the copy of instrument. *Meat Science*, 75(1):29–38, 2007.
- [120] S. Osher and J. A. Sethian. Fronts Propagating with Curvature-Dependent Speed: Algorithms Based on Hamilton-Jacobi Formulations. *Journal of Computational Physics*, 79:12–49, 1988.
- [121] R. R. Paulsen and K. B. Hilger. Shape modelling using markov random field restoration of point correspondences. In *Information Processing in Medical Imaging (IPMI)*, 2003.
- [122] R. R. Paulsen, R. Larsen, S. Laugesen, C. Nielsen, and B. K. Ersbøll. Building and Testing a Statistical Shape Model of the Human Ear Canal. In *Medical Image Computing and Computer-Assisted Intervention (MICCAI)*, volume 2489, pages 373–380, 2002.
- [123] S. M. Pizer, D. S. Fritsch, P. A. Yushkevich, V. E. Johnson, and E. L. Chaney. Segmentation, Registration, and Measurement of Shape Variation via Image Object Shape. *IEEE Transactions on Medical Imaging*, 18(10): 851–865, 1999.
- [124] S. M. Pizer, P. T. Fletcher, S. Joshi, A. Thall, J. Z. Chen, Y. Fridman, D. S. Fritsch, A. G. Gash, J. M. Glotzer, M. R. Jiroutek, et al. Deformable M-Reps for 3D Medical Image Segmentation. *International Journal of Computer Vision*, 55(2):85–106, 2003.
- [125] S. M. Pizer, P. T. Fletcher, S. Joshi, A. G. Gash, J. Stough, A. Thall, G. Tracton, and E. L. Chaney. A method and software for segmentation of anatomic object ensembles by deformable m-reps. *Medical Physics*, 32: 1335–1345, 2005.
- [126] K. T. Rajamani, J. Hug, L. P. Nolte, and M. Styner. Bone Morphing with statistical shape models for enhanced visualization. In *SPIE Int. Symposium on Medical Imaging*, volume 5367, pages 122–130, 2004.
- [127] K. T. Rajamani, S. C. Joshi, and M. A. Styner. Bone model morphing for enhanced surgical visualization. In *IEEE Int. Symposium on Biomedical Imaging (ISBI)*, pages 1255–1258, 2004.

- [128] K. T. Rajamani, L. P. Nolte, and M. Styner. A Novel Approach to Anatomical Structure Morphing for Intraoperative Visualization. In *Medical Image Computing and Computer-Assisted Intervention (MICCAI)*, pages 478–485, 2004.
- [129] K. T. Rajamani, M. A. Styner, H. Talib, G. Zheng, L. P. Nolte, and M. A. G. Ballester. Statistical deformable bone models for robust 3D surface extrapolation from sparse data. *Medical Image Analysis*, 11:99–109, 2007.
- [130] J. O. Ramsay and B. W. Silverman. *Functional Data Analysis*. Springer-Verlag New York, Inc., 1997.
- [131] Y. Rath, S. Dambreville, and A. Tannenbaum. Statistical shape analysis using kernel pca. In *SPIE Int. Symposium on Medical Imaging*, volume 6064, page 60641B, 2006.
- [132] N. Roberts, L. M. Cruz-Orive, N. M. Reid, D. A. Brodie, M. Bourne, and R. H. Edwards. Unbiased estimation of human body composition by the cavalieri method using magnetic resonance imaging. *Journal of Microscopy*, 171:239–253, 1993.
- [133] R. Romvári, A. Dobrowolski, I. Repa, P. Allen, E. Olsen, A. Szabó, and P. Horn. Development of a computed tomography calibration method for the determination of lean meat content in pig carcasses. *Acta Veterinaria Hungarica*, 54(1):1–10, 2006.
- [134] D. Rueckert, L.I. Sonoda, C. Hayes, D.L.G. Hill, M.O. Leach, and D.J. Hawkes. Nonrigid registration using free-form deformations: Application to breast MR images. *Medical Image Analysis*, 18(8):712–721, 1999.
- [135] D. Rueckert, A. F. Frangi, and J. A. Schnabel. Image analysis and modeling - automatic construction of 3-D statistical deformation models of the brain using nonrigid registration. *IEEE Transactions on Medical Imaging*, 22(8):1014–1025, 2003.
- [136] D. Rueckert, A.F. Frangi, and J.A. Schnabel. Automatic construction of 3-D statistical deformation models of the brain using nonrigid registration. *Medical Image Analysis*, 22(8):1014–1025, 2003.
- [137] S. Rusinkiewicz and M. Levoy. Efficient Variants of the ICP Algorithm. In *Third Intl. Conf. on 3D Digital Imaging and Modeling*, pages 145–152, 2001.
- [138] G. Schwarz. Estimating the dimension of a model. *Annals of Statistics*, 6(2):461–464, 1978.
- [139] J.A. Sethian. *Level Set Methods and Fast Marching Methods: Evolving Interfaces in Computational Geometry, Fluid Mechanics, Computer Vision, and Materials Science*. Cambridge University Press, 1999.

- [140] L. Shen, H. Huang, F. Makdeon, and A. J. Saykin. Efficient Registration of 3D SPHARM Surfaces. In *Computer and Robot Vision (CRV)*, pages 81–88, 2007.
- [141] K. Sjöstrand. *Regularized Statistical Analysis of Anatomy*. PhD thesis, Informatics and Mathematical Modelling, Technical University of Denmark, 2007.
- [142] K. Sjöstrand, M. B. Stegmann, and R. Larsen. Sparse principal component analysis in medical shape modeling. In *SPIE Int. Symposium on Medical Imaging*, volume 6144, (6144-179), 2006.
- [143] H. Skjervold, K. Grønseth, O. Vangen, and A. Evensen. In vivo estimation of body composition by computerized tomography. *Zeitschrift für Tierzüchtung und Züchtungsbiologie*, 98:77–79, 1981.
- [144] Danske Slagterier. Statistik 2007 - Svin (in Danish). Technical report, Danish Meat Association, 2008. URL www.danishmeat.dk.
- [145] Danske Slagterier. Årsberetning 2006-07 (in Danish). Technical report, Danish Meat Association, 2007. URL www.danishmeat.dk.
- [146] L. H. Staib and J. S. Duncan. Model-Based Deformable Surface Finding for Medical Images. *IEEE Transactions on Medical Imaging*, 15(5):720–731, 1996.
- [147] K. Stanford, S. D. M. Jones, and M. A. Price. Methods of predicting lamb carcass composition: A review. *Small Ruminant Research*, 29(3):241–254, 1998.
- [148] M. B. Stegmann. *Generative Interpretation of Medical Images*. PhD thesis, Informatics and Mathematical Modelling, Technical University of Denmark, 2004.
- [149] M. B. Stegmann, B. K. Ersbøll, and R. Larsen. FAME - A Flexible Appearance Modelling Environment. *IEEE Transactions on Medical Imaging*, 22(10):1319–1331, 2003.
- [150] M. B. Stegmann, K. Sjöstrand, and R. Larsen. Sparse modeling of landmark and texture variability using the orthomax criterion. In *SPIE Int. Symposium on Medical Imaging*, volume 6144, (61441G), 2006.
- [151] C. Studholme, D. L. G. Hill, and D. J. Hawkes. An overlap invariant entropy measure of 3D medical image alignment. *Pattern Recognition*, 32(1):71–86, 1999.
- [152] C. Studholme, V. Cardenas, R. Blumenfeld, N. Schuff, H. J. Rosen, B. Miller, and M. Weiner. Deformation tensor morphometry of semantic dementia with quantitative validation. *Neuroimage*, 21(4):1387–1398, 2004.
- [153] M. Styner, I. Oguz, S. Xu, C. Brechbühler, D. Pantazis, J. Levitt, M. Shenton, and G. Gerig. Framework for the Statistical Shape Analysis of Brain

- Structures using SPHARM-PDM. In *Open Science Workshop at Medical Image Computing and Computer-Assisted Intervention (MICCAI)*, 2006.
- [154] M. A. Styner, K. T. Rajamani, L. P. Nolte, G. Zsemlye, G. Szekely, C. J. Taylor, and R. H. Davies. Evaluation of 3D correspondence methods for model building. In *Information Processing in Medical Imaging (IPMI)*, pages 63–75, 2003.
- [155] Cs. Szabo, L. Babinszky, M. W. A. Verstegen, O. Vangen, A. J. M. Jansman, and E. Kanis. The application of digital imaging techniques in the in vivo estimation of the body composition of pigs: a review. *Livestock Production Science*, 60(1):1–11, 1999.
- [156] G. Taubin. A signal processing approach to fair surface design. In *Computer Graphics Proceedings (SIGGRAPH)*, pages 351–358, 1995.
- [157] J.P. Thirion. Image matching as a diffusion process: an analogy with Maxwell’s demons. *Medical Image Analysis*, 2(3):243–260, 1998.
- [158] H. H. Thodberg. Minimum Description Length Shape and Appearance Models. In *Information Processing in Medical Imaging (IPMI)*, pages 51–62, 2003.
- [159] H. H. Thodberg and H. Ólafsdóttir. Adding Curvature to Minimum Description Length Shape Models. In *British Machine Vision Conference (BMVC)*, 2003.
- [160] A. Tsai, A. Yezzi Jr, W. Wells, C. Tempany, D. Tucker, A. Fan, W. E. Grimson, and A. Willsky. A Shape-Based Approach to the Segmentation of Medical Imagery Using Level Sets. *IEEE Transactions on Medical Imaging*, 22(2):137–154, 2003.
- [161] G. Turk and J. F. O’Brien. Modelling with implicit surfaces that interpolate. *ACM Transactions on Graphics*, 21(4):855–873, 2002.
- [162] G. Turk and J. F. O’Brien. Shape transformation using variational implicit functions. In *Computer Graphics Proceedings (SIGGRAPH)*, volume 33, pages 335–342, 1999.
- [163] H. C. van Assen, M. G. Danilouchkine, A. F. Frangi, S. Ordás, J. J. M. Westenberg, J. H. C. Reiber, and B. P. F. Lelieveldt. SPASM: A 3D-ASM for segmentation of sparse and arbitrarily oriented cardiac MRI data. *Medical Image Analysis*, 10:286–303, 2006.
- [164] M. Vester-Christensen. *Image Registration and Optimization in the Virtual Slaughterhouse*. PhD thesis, DTU Informatics, Technical University of Denmark, 2008.
- [165] M. Vester-Christensen and R. Larsen. Virtual Jointing of Pig Carcasses using Image Registration and Atlases. Technical report, DTU Informatics, Technical University of Denmark, 2008.

- [166] M. Vester-Christensen, S.G. Erbou, S. Darkner, and R. Larsen. Accelerated 3D Image Registration. In *SPIE Int. Symposium on Medical Imaging*, volume 6512, (651201), 2007.
- [167] M. Vester-Christensen, S. G. H. Erbou, M. F. Hansen, E. V. Olsen, L. B. Christensen, M. Hviid, B. K. Ersbøll, and R. Larsen. Virtual Dissection of Pig Carcasses. *Meat Science*, 81:699–704, 2009. doi: 10.1016/j.meatsci.2008.11.015.
- [168] C. Vestergaard, S. G. Erbou, T. Thauland, J. Adler-Nissen, and P. Berg. Salt distribution in dry-cured ham measured by computed tomography and image analysis. *Meat Science*, 69:9–15, 2005.
- [169] P. Walstra and G. S. M. Merkus. Procedure for assesment of the lean meat percentage as a consequence of the new EU reference dissection method in pig carcass classification. ID-DLO 96.014, 1996.
- [170] Z. Xie and G. E. Farin. Image Registration Using Hierarchical B-Splines. *IEEE Transactions on Visualization and Computer Graphics*, 10(1):85–94, 2004.
- [171] J. Zhang, Y. Ge, S. H. Ong, C. K. Chui, S. H. Teoh, and C. H. Yan. Rapid surface registration of 3D volumes using a neural network approach. *Image and Vision Computing*, 26(2):201–210, 2008.
- [172] B. Zitova and J. Flusser. Image registration methods: a survey. *Image and Vision Computing*, 21:977–1000, 2003.
- [173] H. Zou, T. Hastie, and R. Tibshirani. Sparse principal component analysis. *Journal of Computational and Graphical Statistics*, 15(2):265–286, 2006.